UC Merced
UC Merced Electronic Theses and Dissertations

Title
Quantum Transport of Ultracold Fermions in Optical Potentials

Permalink
https://escholarship.org/uc/item/6dk6r04w

Author
Metcalf, Mekena Lynn

Publication Date
2018

Peer reviewed|Thesis/dissertation

UNIVERSITY OF CALIFORNIA, MERCED

Quantum Transport of Ultracold Fermions in Optical Potentials

A dissertation submitted in partial satisfaction of the
requirements for the degree
Doctor of Philosophy

in

Physics

by

Mekena Lynn Metcalf

Committee in charge:

        Professor Kevin Mitchell, Chair
        Professor Jay Sharping
        Professor Hrant Hratchian
        Professor Chih-Chun Chien

2018

The dissertation of Mekena Lynn Metcalf is approved, and it is acceptable in quality and form for publication on microfilm and electronically:

_____

(Professor Jay Sharping)

_____

(Professor Hrant Hratchian)

_____

(Professor Chih-Chun Chien)

_____

(Professor Kevin Mitchell, Chair)

University of California, Merced

2018

DEDICATION

To my husband, my mom and my dad

EPIGRAPH

In every area of physics, the more you look, the more questions there are. Nothing is fully understandable. I thought if I am going to put all my energy into something, let me put it into something that will benefit mankind

—Dr. Elsa Garmire

LIST OF FIGURES

vii

ACKNOWLEDGEMENTS

VITA

2012	B. S. in Physics, Saint Mary's College of California, Moraga
2018	Ph. D. in Physics, University of California, Merced

PUBLICATIONS

M. Metcalf, G.W. Chern, M. Di Ventra, C.C. Chien (2016), "*Matter-wave propagation in optical lattices: geometrical and flat-band effects*", *J*ournal of Physics B **49**: 075301.

M. Metcalf, C.Y. Lai, C.C. Chien (2016), "*Hysteresis of non-interacting and spin-orbit coupled atomic Fermi gases with dissipation*", *P*hysical Review A **93**: 053617.

M. Metcalf, C.Y. Lai, K. Wright, C.C. Chien (2017), "*Protocols for dynamically probing topological edge states and dimerization with fermionic atoms in optical potentials*", *E*uropean Physics Letters **118**: 56004.

M. Metcalf, C.Y. Lai, M.D. Ventra, C.C. Chien (2018), "*Interaction induced multi-valueness of current fluctuations in closed and open quantum systems*"

ABSTRACT OF THE DISSERTATION

Quantum Transport of Ultracold Fermions in Optical Potentials

by

Mekena Lynn Metcalf

Doctor of Philosophy in Physics

University of California Merced, 2018

Professor Kevin Mitchell, Chair

A new millennia ushered in novel experimental capabilities to investigate engineered quantum systems. Gases consisting of charge neutral atoms are cooled to the ground state and by exploiting the dipole interaction can be trapped by laser light. In ultracold atomic systems the tunneling and interactions are controllable, and the system is absent of disorder. Disorder and interactions in solid-state systems inhibits a complete understanding of transport phenomena. Theoretical investigations into non-equilibrium and equilibrium dynamics of fermions in discretized potentials and in continuum are presented. The affect of controllable, external system parameters is evaluated and exploited to reveal new properties of fermion dynamics. My thesis will begin with an overview of the physics associated with many-body fermion and the models used to obtain results, followed by my thesis research on how matter-waves can be manipulated by lattice geometry and tunneling strengths. Next, I present how dissipation affects current in a continuous ring, demonstrating rate-dependent hysteresis as the particles are driven by an artificial gauge field. After presenting the continuous ring, I will then focus on persistent current and corresponding quantum current fluctuations in a discretized ring. Lissajous curves are found in the system whose area strongly depends on the presence and absence of interactions. Lastly, I will discuss dynamical detection methods for one-dimensional topological insulators us-

ing ultracold fermions. All of the results are supported with discussion on how they can be realized using current experimental technology.

TABLE OF CONTENTS

Chapter 1

Introduction

Revolutions in experimental techniques launched a new, innovative and exciting field of ultra-cold atoms in optical trapping potentials [20]. Prior to the turn of the century, atomic physics research involved optimizing known techniques for many body systems rather than seeking to discover new physics and further the field. Experimental access to dynamics of electrons in solid-state systems was an impossible task due to Fermi velocities near relativistic speeds and collisions happening on the attosecond timescale. Events on these timescales make it challenging to explore quantum behavior of many body systems. Atoms are trapped via an optical-dipole interaction. An array of potentials can be formed to construct periodic potentials, known as optical lattices, using counter propagating lasers. Particles can tunnel through the optical potential barrier to adjacent sites. The tunneling timescales in optical lattices are more tractable with tunneling times on the millisecond time scale, and furthermore possess controllable collision rates [90]. It is also an impossibility to tune interactions in conducting systems since interactions caused by collisions are inherent, along with long-range Coulomb interaction between electrons. Atoms used experimentally are charge neutral and the Feshbach resonance is used to tune the scattering length of atoms from the non-interacting to the strongly interacting limits [135, 125]. Furthermore the trapping potentials are perfect periodic

structures and effects from disorder can be mitigated. The control permitted with cold atoms in optical trapping potentials make them ideal for simulating many-body physics.

Advances in laser cooling and trapping elucidated amazing methods to manipulate, control and detect quantum systems, allowing experimentalists to explore areas such as entanglement, correlation and coherence. Atoms can be cooled to the nanoKelvin regime at a fraction of the Fermi temperature. These cooling techniques permitted bosons to be cooled below the critical temperature for condensation. The experimental observation of the Bose Einstein Condensation (BEC) with laser and evaporation cooling techniques marking the beginning of a new era to discover rich physics for many-body systems [41]. The ability to access the the ground state wave-function in a controlled environment makes cold atoms ideal for engineering model Hamiltonians. Richard Feynman believed quantum computing would be quantum simulators that could simulate quantum many body systems unachievable by current computers. Cold atoms are used to simulate these many-body systems, and have led to amazing new discoveries of condensed matter physics unachievable with material systems. Thus, in the early stages of cold-atoms, the ability to realize universal quantum computer with cold, neutral atoms motivate research efforts[35, 144].Using an optical lattice the Hubbard tight-binding Hamiltonian can be engineered for different lattice geometries [90], and additions like complex next-nearest neighbor tunneling for topological states [77], Hubbard ladders [10, 26], spin-orbit coupling [94, 49], long-range interactions[90, 109, 85], vector potentials [95] opens up thrilling possibilities for theoretical exploration into phenomena of many-body systems not necessarily realizable in traditional solid-state systems.

A complete theoretical understanding of fermionic dynamics is still lacking. However, simulating quantum dynamics in isolated, controlled environments permits theoretical focus on intrinsic transport properties since interactions with the environment must be engineered. Transport can be inhibited by external factors, and disorder within the system leads to localization. Engineering of optical lattices is advantageous for the discovery of new transport behavior and the manipulation of particle transport. A distinct

difference between transport in solid-state systems and cold atom systems is the driving force. The Lorentzian force from a magnetic field drives a current in a conducting system, but since the atoms are charge neutral the addition of an external magnetic field has no effect on delocalization. It is necessary then to mimic the magnetic field using different driving mechanisms. One method to drive the system is to create an energy imbalance across the boundary, and it has been shown a chemical potential imbalance between two halves of a lattice can drive a steady-state current [33]. Optically induced Abelian synthetic magnetic fields formed by coupling of the atoms to Raman laser beams have become a standard method to evaluate particles dynamics induced by a magnetic field[94, 49, 55]. In this thesis work both methods of inducing particle transport are employed for isolated quantum systems as well as systems coupled to the environment.

1.1   Thesis Outline

The second chapter of this thesis is devoted to the theory behind many-body physics used in my PhD work, and subsequent chapters are devoted to the research conducted throughout the graduate program. The entirety of the research focused on fermion particles with unique behavior due to their inability to occupy the same energy state. The antisymmetry of the wave-function and the resulting statistics are discussed. Theory behind condensed matter systems is elucidated with crystals being constructed from translationally invariant unit cells. The energy bands of the crystal structures can be determined using the Bloch formalism, and calculations for the crystal structures in this thesis can be found in the the Appendix. Lastly discussed in the introductory theoretical chapter is the formulation for the Hubbard tight-binding model which is the Hamiltonian used in all theoretical calculations conducted for lattices systems in this work.

In the third chapter work done on the manipulation of matter-wave propagation by tuning lattice geometry and tunneling strengths is presented. Quantum transport of fermionic atoms in optical lattices with various geometries is studied. Looking at the

probability density of particles over time on the square, triangle and body centered lattice we find an increase in particle velocity as diagonal links are added to the system. As the longitudinal dimension is increased the velocities converge to the maximum group velocity of the system predicted by band theory. Calculations elucidated a phenomenological result in the body centered lattice where a flat band exists under special cases. A controllable range of velocities when transitioning from the triangle lattice to the zig-zag lattice is found. All theoretical results are experimentally realizable in optical lattice systems with ultra-cold fermionic gases.

Rate-dependent hysteresis of current resulting from external dissipation on persistent current in a continuous ring is discussed in the fourth chapter. In most systems exhibiting hysteresis interactions are present, but hysteresis exists for a non-interacting Fermi gas in an optical ring potential when driven by a time-dependent artificial gauge field and subject to dissipation. Fermions in a ring potential threaded with flux can exhibit a persistent current when the system is in thermal equilibrium, but cold-atoms in optical potentials lack scattering mechanisms due to perfect periodicity and dissipation for reaching thermal equilibrium can be introduced by an external, thermal bath. The standard relaxation approximation is used to model the dynamics of cold-atoms driven periodically by an artificial gauge field. A competition of the driven time and the relaxation time leads to hysteresis of mass current, and work done on the system, as a function of the relaxation time, exhibits similar behavior as Kramers transition rate in chemical reaction and one-dimensional thermal transport. Therefore, noninteracting systems with suitable dissipation are sufficient to support hysteresis behavior which can be observed with current experimental techniques.

In the fifth chapter dynamical methods are presented to detect topological signatures of a non-interacting and interacting one-dimensional topological insulator. Topological edge states are difficult to detect in ultracold atoms because the background harmonic, confining potential prevents direct detection of topological edge states arising at the boundary because the additional potential fuses the edge states into the bulk. Protocols

are proposed to probe localized edge states and dimerization of ultracold fermions that are within current experimental capability. By confining atoms in a ring lattice and change the boundary condition from periodic to open using an off-resonant laser sheet to cut open the ring, topological edge states can be generated. A lattice in a topological configuration can trap a single particle released at the edge as the system evolves in time. Alternatively, depleting an initially filled system away from the boundary reveals the occupied edge states. Signatures of dimerization in the presence of contact interactions can be found in selected correlations as the system boundary suddenly changes from periodic to open and exhibit memory effect of the initial state, which can distinguish topological structures or different insulating phases.

A global property of persistent current and quantum current fluctuations in mesoscopic systems, interaction induced Lissajous curves, is presented in the sixth chapter. Measurement of quantum systems has remained one of the spooky features of quantum mechanics due to the probability nature of particles. There exist fluctuations in the measurement of quantum systems calculated as the standard deviation of an operator's expectation value. The fluctuation of current in a mesoscopic ring lattice has unique features when interactions are considered. In a non-interacting system there exists a fourth-order degeneracy point periodic in flux. At this point the current is null and the fluctuations demonstrate a jump to compensate for the jump in current. The addition of interactions lifts the degeneracy the current and fluctuations become continuous. In the interacting cases the current and current fluctuations form Lissajous curves which indicated the underlying periodic nature of the measurements. In the non-interacting picture the curve has zero area and jumps to a finite value with any interaction, indicating a topological change. Addition of next-nearest-neighbor tunneling is considered and the Lissajous curves are robust against small tunneling strengths. The Lissajous curves were see in both a periodic, closed quantum system and an open quantum system connected to external reservoirs demonstrating this global property of quantum transport.

Publications in the PhD Work:

- Chapter 3

  M. Metcalf, G.W. Chern, M. Di Ventra, C.C. Chien (2016), "*Matter-wave propagation in optical lattices: geometrical and flat-band effects*", Journal of Physics B **49**: 075301.

- Chapter 4

  M. Metcalf, C.Y. Lai, C.C. Chien (2016), "*Hysteresis of non-interacting and spin-orbit coupled atomic Fermi gases with dissipation*", Physical Review A **93**: 053617.

- Chapter 5

  M. Metcalf, C.Y. Lai, K. Wright, C.C. Chien (2017), "*Protocols for dynamically probing topological edge states and dimerization with fermionic atoms in optical potentials*", European Physics Letters **118**: 56004.

- Chapter 6

  M. Metcalf, C.Y. Lai, M.D. Ventra, C.C. Chien (2018), "*Interaction induced multi-valueness of current fluctuations in closed and open quantum systems*"

Chapter 2

Many-Body Physics of Fermions

2.1 Fermion Antisymmetry

Nature contains two types of particles with different spin quantum numbers: bosons with spin 1 and fermions with spin 1/2. Fermions are the particles building up the atom such as electrons, protons and neutrons. Single particle fermions have two spin states, "spin up" $|\uparrow\rangle$ and "spin down" $|\downarrow\rangle$, and the spin states are orthonormal

$$\langle\uparrow|\uparrow\rangle = 1 \qquad\qquad \langle\downarrow|\downarrow\rangle = 1 \qquad\qquad (2.1)$$

$$\langle\uparrow|\downarrow\rangle = 0 \qquad\qquad \langle\downarrow|\uparrow\rangle = 0. \qquad\qquad (2.2)$$

The two spin species are distinguishable from each other, but particles of the same spin are indistinguishable (or identical). Indistinguishable fermions possess an antisymmetric wave function

$$\Psi(\mathbf{x}_1, ..., \mathbf{x}_i, \mathbf{x}_j, ..., \mathbf{x}_N) = -\Psi(\mathbf{x}_1, ..., \mathbf{x}_j, \mathbf{x}_i, ..., \mathbf{x}_N), \qquad (2.3)$$

and under interchange of spatial coordinates of any two identical fermions the wave function gains a negative sign. Antisymmetry of the wave function under particle

exchange proves the Pauli exclusion principle, since with equal coordinates $\mathbf{x}_i = \mathbf{x_j}$ the wave function $\Psi(\mathbf{x}_1, ..., \mathbf{x}_i, \mathbf{x}_j, ..., \mathbf{x}_N) = 0$. Thus, no fermionic particle can occupy the same quantum state. For example, a molecular or atomic orbital can only contain two distinguishable fermions, one spin up and one spin down.

In most physical systems, there are more particles than a single fermion, requiring construction of a many body wave function. The most general construction of the many body wave function for particles is expanding it as a product of single particle wave functions

$$\Psi(\mathbf{x}_1, ..., \mathbf{x}_i, \mathbf{x}_j, ..., \mathbf{x}_N) = \phi(\mathbf{x}_1)...\phi(\mathbf{x}_i)\phi(\mathbf{x}_j)...\phi(\mathbf{x}_N). \tag{2.4}$$

This generalized formula, known has Hartree products, distinguishes between identical particles and a linear combination of the Hartree products is needed to obtain the complete wave function. The linear combination for the antisymmetric wave function can be constructed as a Slater determinant

$$\Psi(\mathbf{x}_1, ..., \mathbf{x}_i, \mathbf{x}_j, ..., \mathbf{x}_N) = \frac{1}{\sqrt{N!}} \begin{vmatrix} \phi_{\nu_1}(\mathbf{x}_1) & . & . & . & \phi_{\nu 1}(\mathbf{x}_n) \\ & & . & & \\ & & & . & \\ & & & . & \\ \phi_{\nu_N}(\mathbf{x}_1) & . & . & . & \phi_{\nu_N}(\mathbf{x}_n) \end{vmatrix} \tag{2.5}$$

of the single particle eigenstates where ν_i is the single particle state. This notation of the many body wave function is known as first quantization.

2.2 Fermi-Dirac Statistics

Consider non-interacting fermions of a chosen spin component in a gas as indistinguishable particles in thermodynamic equilibrium. These particles can only occupy a single state or energy level, so the N particles will fill up the energy to some ϵ_N. The grand canonical ensemble is used with a fixed chemical potential μ which controls

the rate of change of the energy with particle number. The energy can be determined by summing over the states

$$E = \sum_i^N (\epsilon_i n_i - \mu_i n_i) \tag{2.6}$$

with n_i being the occupancy of the energy. The grand-canonical partition function summed over all possible states ν

$$Z = \sum_\nu e^{-\beta E_\nu} \tag{2.7}$$

provides a statistical outcome of all system possibilities. The coefficient $\beta = 1/k_b T$ where k_b is the Boltzmann's constant and T is the temperature. In quantum mechanics the state ν is specified by the occupancies $(n_1, ...n_i, n_j, ...n_N)$ of the energy states. The partition function for fermions with an occupancy of 0 or 1 due to the Pauli exclusion principle is

$$Z = \sum_{n_1,...n_i,n_j,...n_N=0}^{1} e^{-\beta \sum_i (\epsilon_i n_i - \mu n_i)} \tag{2.8}$$

$$= \prod_i \sum_{n_i=0}^{1} e^{-\beta \sum_i (\epsilon_i - \mu) n_i} \tag{2.9}$$

$$= \prod_i (1 + e^{-\beta(\epsilon-\mu)}) \tag{2.10}$$

The particle distribution is determined by

$$\langle n \rangle = \frac{\partial \ln(Z)}{\partial(-\beta\epsilon)} \tag{2.11}$$

$$= \frac{\partial \ln(1 + e^{-\beta(\epsilon-\mu)})}{\partial(-\beta\epsilon)} \tag{2.12}$$

$$= \frac{1}{e^{\beta(\epsilon-\mu)} + 1} \tag{2.13}$$

and $F(\epsilon) = 1/(e^{\beta(\epsilon-\mu)} + 1)$ is better known as the Ferm-Dirac distribution function.

The energy of a free fermion is related to the wave vector $\mathbf{k} = k_x \hat{x} + k_y \hat{y} + k_z \hat{z}$ by $\epsilon(\mathbf{k} = \hbar^2 \mathbf{k}^2 / 2m$ where m is the mass of the fermion. Density of states can be determine

using the relationship $\langle N \rangle = \sum_i \langle n_i \rangle$. Considering a cubic volume where $V = L^3$ we find that

$$\langle N \rangle = \frac{2L^3}{(2\pi)^3} \int d\mathbf{k} F(\epsilon(k)). \tag{2.14}$$

Density of state becomes much more tractable in the limit as $T \to 0$ since the Fermi-Dirac function becomes

$$F(\epsilon) = 1 \qquad\qquad\qquad \epsilon < \mu_0 \tag{2.15}$$

$$= 0 \qquad\qquad\qquad \epsilon > \mu_0 \tag{2.16}$$

The chemical potential in the limit of zero temperature is referred to as the Fermi energy E_f since particle occupancy is zero above this value. The Fermi momentum k_F gives the Fermi surface in which the density of states is zero in momementum space when $k > k_F$.

2.3 Fock Space and Second Quantization

Determining distinguishability of particles is necessary to compose a many-body basis. Particles of the same spin species are indistinguishable from one another, where particles of different spin species are distinguishable. A Hilbert space must be constructed for single particle systems for each set of indistinguishable particles. From these single-particle Hilbert spaces a many-particle Hilbert space is constructed for the distinguishable sets. This many-particle Hilbert space is better known as Fock space. Fermions have two distinguishable types, spin up and spin down, that make up the Fock space. The total Hilbert space for a many-particle fermion system is the tensor product of the single particle Hilbert spaces for the two spin types

$$\mathcal{H}_{tot} = \mathcal{H}_\uparrow \otimes \mathcal{H}_\downarrow. \tag{2.17}$$

Before describing how to construct the single particle Hilbert spaces composed of Fock states, it is worth introducing second quantization notation.

A complete set of single particle states, describing the number of particles occupying each state, are constructed from abstract state vectors $|n_1 n_2 .. n_i n_j ... n_N\rangle$ representing N total states, and for fermions the occupancy $n_\nu = 0$ or 1. The vector product of these states for both spins is known as the Fock state

$$|F\rangle = |n_{1\uparrow} n_{2\uparrow} .. n_{i\uparrow} n_{j\uparrow} ... n_{N\uparrow}\rangle |n_{1\downarrow} n_{2\downarrow} .. n_{i\downarrow} n_{j\downarrow} ... n_{N\downarrow}\rangle. \tag{2.18}$$

The many particle wave function is expanded in these Fock states

$$|\Psi\rangle = \sum_i c_i |F_i\rangle \tag{2.19}$$

where c_i is the expansion coefficient for the Fock basis.

Operators act on a Fock state to either create or remove a particle from an individual state n_ν. These operators are known as the creation operator $c_\nu^\dagger$ and annihilation operator c^ν. The creation operator creates a particle on a state

$$c_\nu^\dagger |0\rangle = |1\rangle, \tag{2.20}$$

and to satisfy the Pauli exclusion principle $c_\nu^\dagger c_\nu^\dagger |0\rangle = 0$. The annihilation operator removes a particle from a state

$$c_\nu |1\rangle = |0\rangle \qquad\qquad c_\nu |0\rangle = 0. \tag{2.21}$$

Statistics of these operators must account for the antisymmetry of the many-body fermion wave function, so they anticommute $\{A, B\} = AB + BA$. The anticommutation relations for the creation and annihilation operators are as follows:

$$\{c_{\nu'}, c_\nu^\dagger\} = \delta_{\nu'\nu} \tag{2.22a}$$

$$\{c_{\nu'}^\dagger, c_\nu^\dagger\} = \{c_{\nu'}, c_\nu\} = 0. \tag{2.22b}$$

By using anticommutation relations the negative sign obtained through the exchange of two fermions on different states is accounted for. The number of particles on an individual state n_ν is found by the number operator $\hat{n}_\nu = c_\nu^\dagger c_\nu$ which has eigenvalues of either 0 or 1.

Using the second quantization operators a Fock state can be constructed on the vacuum

$$|F\rangle = \prod_i^{N_p} c_i^\dagger |0\rangle, \tag{2.23}$$

where N_p is the number of particles in the system. For example, the Fock state $|010011\rangle$, site indexing is right to left, with six states and three particles is constructed from the vacuum as $c_5^\dagger c_2^\dagger c_1^\dagger |0\rangle$. It is a combinatorics problem to determine the total number of Fock states with six states and three particles. All the Fock states make up the Hilbert space which scales

$$\mathcal{H} = \frac{N!}{N_p!(N - N_p)!} \tag{2.24}$$

for a single particle system. The size of the Fock space is found from multiplying the Hilbert space for both fermion spin species.

2.4 Tight-Binding Model

Crystal structured materials possess translational symmetry with the atoms arranging in a periodic structure. The periodicity can be quantified by Bravais lattice vector $\mathbf{R} = n_1\vec{a}_1 + n_2\vec{a}_2 + n_3\vec{a}_3$ where $n_{1,2,3}$ is some integer and $\vec{a}_{1,2,3}$ are the unit vectors for a three dimensional solid. A good approximation is to consider the entire Hamiltonian for the crystal structure can be approximated by individual Hamiltonians for an atom at each lattice site. The wave function of the electron is considered to be very small when the distance r is greater than the order of a lattice constant. Electrons occupying a lattice site are considered to be bound by the wave function.

2.4.1 Non-Interacting Fermions

The potential created by the atoms is a one-electron potential $V(\mathbf{r})$ periodic under the lattice vectors $V(\mathbf{r}) = V(\mathbf{r} + \mathbf{R})$. A free-particle in a periodic potential is described by

the Hamiltonian

$$H = -\frac{\hbar^2}{2m}\nabla^2 + V(\mathbf{r}). \tag{2.25}$$

Since the potential and Hamiltonian are periodic in both real space and reciprocal space the wave function can be written as a plane wave multiplied by a periodic function

$$\psi_{nk}(\mathbf{r}) = e^{i\mathbf{k}\cdot\mathbf{r}}u_{nk}(\mathbf{r}) \tag{2.26}$$

where $u_{nk}(\mathbf{r}+\mathbf{R}) = u_k(\mathbf{r})$, $\mathbf{k}$ is the crystal momentum and n is the quantum number. This theorem, better known as Bloch's theorem, implies

$$\psi_{nk}(\mathbf{r}+\mathbf{R}) = e^{i\mathbf{k}\cdot\mathbf{r}}\psi_{nk}(\mathbf{r}) \tag{2.27}$$

which is the Bloch wave function in continuous models. Remembering fermions can't occupy the same state, a total of N particles will fill up N $\mathbf{k}$ values in the first Brillouin zone. The largest occupied $\mathbf{k}$ state is the Fermi surface, and the energy corresponding to this crystal momentum is the Fermi energy.

In the tight-binding approximation we consider the wave function restricted to lattice sites, yet this wave function must satisfy Bloch's theorem for periodic potentials. The wave function that satisfies Bloch's theorem is determined by summing over the lattice vectors

$$\psi_{nk}(\mathbf{r}) = \sum_{\mathbf{R}} e^{i\mathbf{k}\cdot\mathbf{R}}\psi_n(\mathbf{r}-\mathbf{R}). \tag{2.28}$$

Working in second-quantization this can be integrated into the operators such that

$$c_i = \sum_{\mathbf{k}} e^{i\mathbf{k}\cdot\mathbf{R}_i}c_{\mathbf{k}} \tag{2.29}$$

$$c_i^\dagger = \sum_{\mathbf{k}} e^{-i\mathbf{k}\cdot\mathbf{R}_i}c_{\mathbf{k}}^\dagger \tag{2.30}$$

Using second quantization, the tight-binding model and introducing a simplification of atomic orbitals, the non-interacting Hamiltonian can be expressed

$$H = \sum_{\langle ij \rangle}(t_{ij}c_i^\dagger c_j + h.c.) + \sum_i V_i c_i^\dagger c_i \tag{2.31}$$

where t_{ij} is the coefficient for the kinetic term of the Hamiltonian describing atomic orbital overlap and a particle tunneling from one site to it's neighbor and V_i is the onsite potential. Working with this Hamiltonian and formula can be derived using the operators derived with Bloch's theorem to determine the Bloch energies for non-interacting fermions. The Hamiltonian in momentum space is written as

$$H(\mathbf{k}) = \sum_{\mathbf{k}} \epsilon(\mathbf{k}) c_{\mathbf{k}}^{\dagger} c_{\mathbf{k}} \tag{2.32}$$

and $\epsilon(\mathbf{k})$ is the Bloch energy. Transforming the Hamiltonian in real space to momentum space using the relationship for the second-quantization operators above we can obtain the Bloch energies for any Bravais lattice. Using the non-interacting tight-binding model we find where the tunneling between sites in reciprocal space is $t_{kk'}$ the Bloch energy can be obtained

$$H = \sum_{\langle ij \rangle} (t_{ij} c_i^{\dagger} c_j + h.c.) + \sum_i V_i c_i^{\dagger} c_i \tag{2.33}$$

$$= \sum_{\langle ij \rangle} \sum_{\mathbf{kk'}} (t_{ij} e^{-i(\mathbf{k} \cdot \mathbf{R}_i)} e^{i(\mathbf{k'} \cdot \mathbf{R}_j)} c_{\mathbf{k}}^{\dagger} c_{\mathbf{k}} + h.c.) + V \sum_{\mathbf{k}} c_{\mathbf{k}}^{\dagger} c_{\mathbf{k}} \tag{2.34}$$

$$= \sum_{\langle ij \rangle} \sum_{\mathbf{kk'}} (t_{ij} e^{i(\mathbf{k'} \cdot \mathbf{R}_j - \mathbf{k} \cdot \mathbf{R}_i)} c_{\mathbf{k}}^{\dagger} c_{\mathbf{k}}) + h.c.) + V \sum_{\mathbf{k}} c_{\mathbf{k}}^{\dagger} c_{\mathbf{k}} \tag{2.35}$$

$$\tag{2.36}$$

$$\epsilon(\mathbf{k}) = \sum_{\langle ij \rangle} \sum_{kk'} (t_{ij} e^{i(\mathbf{k'} \cdot \mathbf{R}_j - \mathbf{k} \cdot \mathbf{R}_i)} + h.c.) + V \tag{2.37}$$

$$= \sum_{\langle ij \rangle} \sum_{kk'} (t_{ij} e^{i\mathbf{k'} \cdot (\mathbf{R}_j - \mathbf{R}_i)} e^{i(\mathbf{k'} - \mathbf{k}) \cdot \mathbf{R}_j} + h.c.) + V \tag{2.38}$$

$$= \sum_{kk'} (t_{ij} e^{i\mathbf{k'} \cdot (\mathbf{R}_j - \mathbf{R}_i)} \delta(\mathbf{k'} - \mathbf{k}) + h.c.) + V \tag{2.39}$$

$$= \sum_{\langle ij \rangle} \sum_k (t_{ij} e^{i\mathbf{k} \cdot (\mathbf{R}_j - \mathbf{R}_i)} + h.c.) + V \tag{2.40}$$

It can be seen from this equation that the addition of an onsite potential only shifts the energy by a constant value V. For a one-dimensional lattice with a lattice vector

$\mathbf{R} = a\hat{\mathbf{x}}$ and hopping between nearest neighbors $\bar{t}$, the Bloch energy can be determined with nearest-neighbor hopping $i = j + 1$ by

$$\epsilon(\mathbf{k}) = \bar{t}(e^{i(kja-kja-ka)} + \bar{t}e^{-i(kja-kja-ka)}) + V \tag{2.41}$$

$$= \bar{t}(e^{-ika} + e^{ika}) + V \tag{2.42}$$

$$= 2\bar{t}\cos(ka) + V \tag{2.43}$$

The total energy is found by taking the summation in momentum space until the Fermi surface

$$E = \sum_{k}^{k_f} \epsilon(\mathbf{k}), \tag{2.44}$$

providing an analytical description of the energy of a free particle in a crystalline lattice. However, this method breaks down with the addition of fermion-fermion interactions.

2.4.2 Hubbard Onsite Interaction

Charged particles are subjected to the Coulomb interactions. Accounting for interactions in many-body physics and physical chemistry is a difficult challenge analytically and computationally. In the tight-binding model the interactions are local and limited to onsite Pauli repulsive interactions with strength U; therefore, an energy cost is associated with doubly occupied sites. This interaction known as the Hubbard interaction can be expressed in second quantization as a quartic operator

$$H_U = U \sum_{i} c_{i\uparrow}^{\dagger} c_{i\uparrow} c_{i\downarrow}^{\dagger} c_{i\downarrow}. \tag{2.45}$$

The Hubbard model, with diagonal elements U and off-diagonal tunneling terms $\bar{t}$, is a gross over simplification of interactions in real materials, but it has successfully predicted observable phenomena [92]. The utility of the Hubbard model renders it ubiquitous in the study of phenomenological behavior of material systems. This being said, cold atoms were designed to realize the Hubbard model and the Hamiltonian coefficients are tunable. The

ability for cold atoms to realize these toy models demonstrates the value. Exotic features resulting from interactions can be easily quantified and accessed.

Though the Hubbard model is simplified compared to a full Hamiltonian which quantifies atomic and molecular orbitals, it is still difficult to solve. When interactions are added the basis can no longer be expanded in the onsite single particle basis. The many-particle wave-function is required and the Hilbert space is exponentially large. The single-particle Hamiltonian with two spin species scales as 2^N where is N is the number of lattice sites. To calculate an exact solution of the ground state energy and wave function the size of the system is limited. Using the Hartree-Fock method the interaction term can be reduced to a single particle potential that arises from an average interaction of all other particle. The Hartree Fock method is useful in the small U limit, $U \leq \bar{t}$, for a large system size. The density-density terms for the spin species in the interacting Hamiltonian term can be decoupled, and the interaction Hamiltonian becomes a sum of the spin up and spin down Hamiltonian with the addition of a constant term

$$H_U = U \sum_i n_{i\uparrow} \langle n_{i\downarrow} \rangle + U \sum_i \langle n_{i\uparrow} \rangle n_{i\downarrow} - U \sum_i \langle n_{i\uparrow} \rangle \langle n_{i\downarrow} \rangle. \qquad (2.46)$$

If the system has an equal population of particles $N_\uparrow = N_\downarrow$, the Hamiltonian is approximated in a reduced form

$$\langle H_U \rangle = U \sum_i \langle n_{i\uparrow} \rangle \langle n_{i\downarrow} \rangle. \qquad (2.47)$$

However many interesting effects occur with strong interactions, and the Hartree-Fock approximation will provide inaccurate quantifications of the energy. An exact diagonalization computational technique is used to obtain solutions for the Hubbard model with interactions in the following work.

Chapter 3

Matter Wave Propagation of Fermions in 2D Optical Lattices: Geometry and Flat Band Effects

The work on how lattice geometry affects ballistic particle transport has been published in a peer-reviewed journal see Ref [106] Copyright 2017 IOP Publishing. Below is a more detailed description of my work.

3.1   Motivation

Variational calculus led to the conclusion the shortest distance to move between two points is a straight line. Is the same true in quantum mechanics? Studying the dynamics of ultra-cold atomic gases in optical lattices provides a tool for quantum simulation, and understanding the effects of many body systems. Fermions moving in an optical lattice can produce a quasi-steady state current as fermions tunnel through the optical potential of the lattice [33]. Optimizing particle travel can enhance the usefulness of the observed current which will be of importance in the developing field of atomtronics [129, 115]. The

fermi velocity in a typical copper conductor is on the order of 10^6m/s where the v_F in a cold atom system is one the order of 10^{-3}m/s [22]. It is therefore imperative to find a way to increase particle velocity through a lattice.

By measuring the probability density over time for three different geometries we observe an increase in particle velocity through the lattice as more diagonal links are added. Our numerical calculations demonstrate that as the longitudinal dimension is increased particles move at the maximum group velocity predicted by energy band theory. It is apparent that the increase in group velocity comes from the mixing of the wave vectors when diagonal links are added.

Calculations of the square lattice with next-nearest-neigbor hopping (SNNN) revealed an interesting phenomenological result preventing particle transport through the lattice. A flat band appears in the 1D SNNN lattice resulting from overlapping energy bands [40]. This result is dependent on the equivalence of hopping coefficents along all links in the lattice and the longitudinal dimension of the lattice. With an increased interest in flat band systems in the cold atom community our results provide a mechanism to study the transition between a system with and without a flat band [76].

The spin frustrated zig-zag lattice also provides an opportunity to explore rich physics in optical lattice systems[57]. We explore the ability to tune the velocity of the matter wave by changing the ratio of hopping coefficients along the diagonal and horizontal links. Transition from the zig-zag lattice to the triangle lattice increases the range of wavefront velocity and allows for experimental control of particle movement.

3.2   Theoretical Description of the Tight-Binding Model and Time Evolution of the Correlation Matrix

Initially the system is prepared with non-interacting fermions in their ground state on the left half of the lattice, and the particles move to the right half of the lattice by tunneling
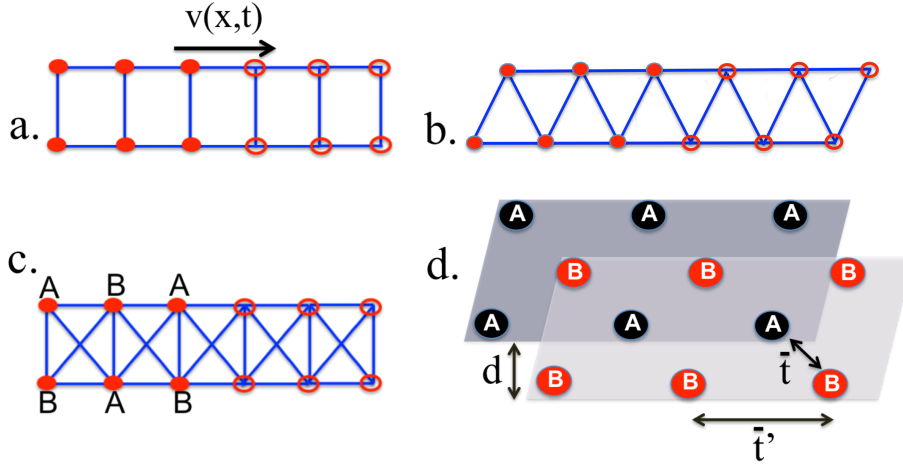
Figure 3.1: Lattice geometries for the (a) square, (b) triangle, and (c) SNNN lattice respectively. The left half of the lattice is filled with particles (solid red circles), and the right half is absent of particles (red rings). The particles propagate ballistically from the left half to the right half of the lattice as the system evolves in time, indicated by velocity vector. (d) Potential experimental realization of BCL using bi-layered optical lattices

through the optical potential $V(r)$ which is proportional to the intensity of the laser beam. We use the tight-binding hopping Hamiltonian without the interaction term.

$$H = -\sum_i \sum_\Delta \bar{t}_{ij} c_i^\dagger c_j$$

where $\bar{t}$ is the hopping coefficient and determines the unit of time $t_0 = \hbar/\bar{t}$ as the particle move from site $j = \bar{x}\bar{y}$ to the nearest neighbor $i = \bar{x}\bar{y} + \Delta$. Nearest neighbor to a specific site are denoted by Δ. The creation $c_i^\dagger$ and annihilation c_j operators make up the correlation matrix we use to analyze particle travel. Elements of the correlation matrix determine the probability density of hopping from site j to site i, and is used to determine the probability density $\langle \hat{n}_i \rangle = \langle c_i^\dagger c_i \rangle$ of being on the far right of the lattice [32]. The lattice constant, a, connecting unit cells serves as the unit of length and is set to one. We incorporate two dimensional inter-site travel for three lattices: the square lattice, the triangular lattice and the SNNN lattice Figure 3.1.

Time-evolving the correlation matrix operator using the Heisenberg equation of motion, with $\hbar = 1$ with the Hamiltonian, we can measure the probability density of a particle on the ith site over time. The equation of motion can be solved using the anti-commutation relations of fermions [48]. The generic form of the equation of motion

$$-i\frac{\partial\langle c_i^\dagger c_j\rangle}{\partial t} = \langle [c_i^\dagger c_j, H]\rangle, \tag{3.1}$$

can be evolved using the expression for the tight binding Hamiltonian,

$$-i\frac{\partial\langle c_i^\dagger c_j\rangle}{\partial t} = -\bar{t}\sum_\Delta(\langle c_i^\dagger c_{j+\Delta}\rangle - \langle c_{i-\Delta}^\dagger c_j\rangle) \tag{3.2}$$

The equation of motion was evaluated numerically using the Runge-Kutta method Appendix A.2.5 since it has improved accuracy to the simple Euler method [118]. The initial correlation matrix was set up with a particle located at each site on the left hand site of the lattice. It is then necessary to determine the nearest neighbors of site i in order to evolve the matrix with time.

In the thermodynamic limit of infinitely large lattices, the results should agree with band theory [9]. The correlation matrix is converted into momentum space

$$c_j = \sum_k c_k e^{ik\cdot x_j} \tag{3.3}$$

$$c_i^\dagger = \sum_k c_k^\dagger e^{-ik\cdot x_i} \tag{3.4}$$

$$x_j \to x_i + \Delta \tag{3.5}$$

where Δ is the nearest neighbor to site i, and is determined from the lattice vectors. The energy bands are determined by taking the Fourier transform of the tightbinding Hamiltonian for a given lattice configuration

$$H = \sum_k \epsilon_k c_k^\dagger c_k \tag{3.6}$$

to obtain the energy dispersion

$$\epsilon_k = -\bar{t} \sum_\Delta e^{ik \cdot \Delta} \tag{3.7}$$

Here c_k ($c_k^\dagger$) is the annihilation (creation) operator in momentum space. The dispersion ϵ_k can be exactly solved for noninteracting fermions. Importantly, the semiclassical group velocity in the transverse direction is given by [9]

$$\mathbf{v}_{k_x} = \frac{\partial}{\partial k_x} \epsilon_{k_x, k_y}. \tag{3.8}$$

This semiclassical prediction in the thermodynamic limit will be compared to the fully quantum mechanical results of matter-wave propagation.

To determine the effects of mean field interactions we consider two fermionic species with opposite spin. The system was modeled using the Hubbard interaction Hamiltonian.

$$H_{int} = H + U \sum_i \hat{n}_{i\uparrow} \hat{n}_{i\downarrow}$$

Where

$$\hat{n}_{i\uparrow} = c_{i\uparrow}^\dagger c_{i\uparrow}$$

is the number operator and U is the onsite repulsive coupling constant. The interaction Hamiltonian is evaluated in the same manner as before by solving the for the equation of motion in the Heisenberg picture. The Hartree-Fock approximation defined in Chapter 2 is needed to obtain a closed-form solution of the equation of motion. The two fermionic species are considered to be symmetric such that $\langle c_{i\uparrow}^\dagger c_{i\uparrow} \rangle = \langle c_{i\downarrow}^\dagger c_{i\downarrow} \rangle$ and the Hamiltonian takes the form of Equation 2.47. Using this approximation, the equation of motion becomes [30].

$$\begin{aligned} -i\frac{\partial \langle c_i^\dagger c_j \rangle}{\partial t} &= -\bar{t} \sum_\Delta (\langle c_i^\dagger c_{j+\Delta} \rangle - \langle c_{i-\Delta}^\dagger c_j \rangle) - \\ &\quad -U(\langle c_i^\dagger c_j \rangle \langle c_i^\dagger c_i \rangle - \langle c_i^\dagger c_j \rangle \langle c_j^\dagger c_j \rangle). \end{aligned} \tag{3.9}$$
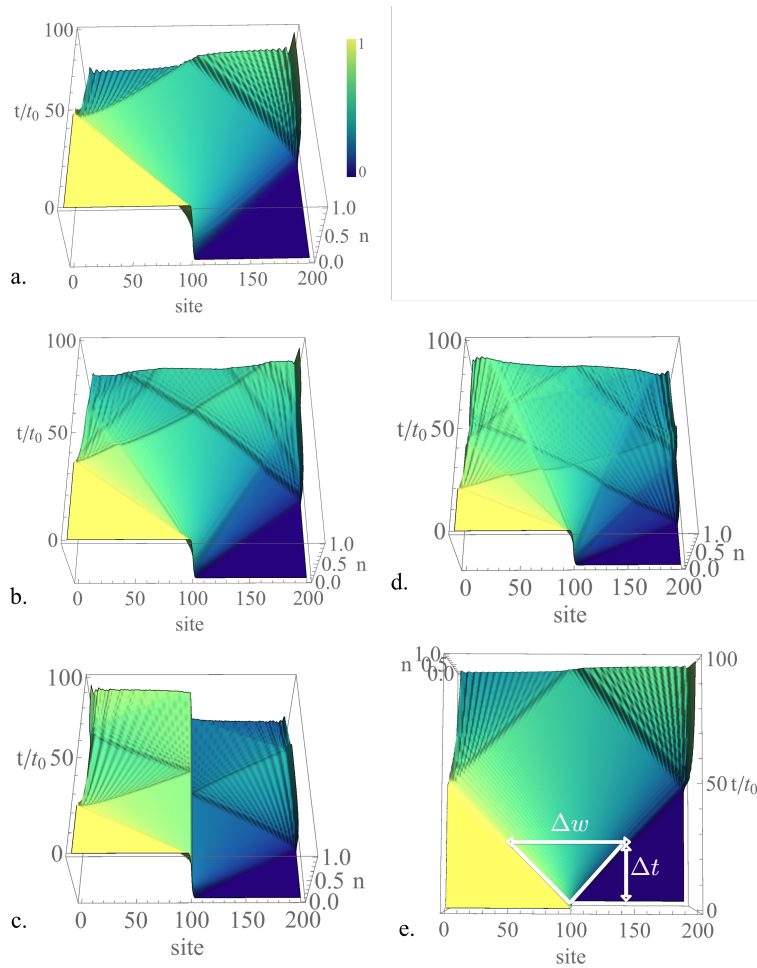
Figure 3.2: Evolution of the particle density. Here the brighter regions correspond to higher density. (a) Square lattice. (b) Triangular lattice. (c) Two-leg SNNN lattice. Here $L_x = 200$ and $L_y = 2$. In (c) there is a density discontinuity at $L_x/2$ caused by the flat band. (d) The SNNN lattice with $L_x = 200$ and $L_y = 3$ shows no density discontinuity.

3.3 Expansion Dynamics and Maximized Group Velocity

We first consider uniform lattices where all hopping coefficients are equal: $\bar{t}_{ij} = \bar{t}$. The time it takes for a particle to tunnel through an isolated double-well potential is $\pi t_0/2$ [36], and in a 1D multi-site lattice it asymptotically takes $t_0/2$ to tunnel through one link [32, 30] because of the modification of the dispersion. Since quantum matter wave is sensitive to how each site is connected to its neighbors, with suitably chosen lattice geometry the propagation speed can be altered.

Figure 3.2 shows the evolution of the y-direction averaged density,

$$\bar{n}(i_x) \equiv (\sum_{i_y=1}^{L_y} n_{i_x,i_y})/L_y,$$

for the square, triangular, and SNNN lattices with $(L_x, L_y) = (200, 2)$ Figure 3.2 ((a)-(c)) and for the SNNN lattice with $(L_x, L_y) = (200, 3)$Figure 3.2 (d). At $t = 0$ the left half is filled and the right half is empty. The spreading of the density clearly shows a light-cone structure [32, 123] with the outermost wavefront showing a constant maximal propagating speed. For different geometries the maximal speeds are different, and there are equivalent ways for measuring them. For instance, the expansion rate of the perturbed region of the cloud given by $\Delta w/\Delta t$ Figure 3.2 (e) will be twice of the propagating speed [123]. Since the propagating speed is constant as one can observe from Fig. 3.2, measuring the time t_x it takes for the outermost wavefront to reach a point i_x can also be used to evaluate the maximal speed $v_m = (i_x - i_{L/2})/t_x$. Measurement of the expansion velocity of non-interacting fermions will yield the same results since fermions expand ballistically with a constant, radial expansion velocity $v_r = \sqrt{2}(i_x - i_{L/2})/(t_x)$ [123]. In our simulations the initial transport is ballistic, and the latter method determines the maximal propagating speed.

It can be observed that the wavefront speed increases as more diagonal links are added to the lattice. The full quantum dynamics thus claims that altering the lattice geometry may boost matter-wave propagation, which can be very difficult to explain using classical
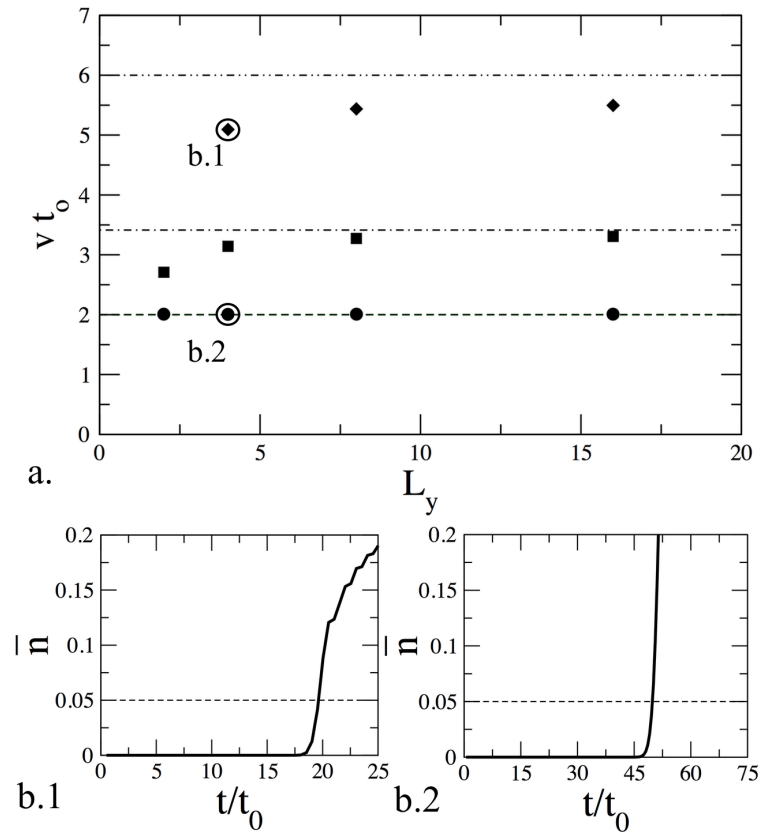
Figure 3.3: (a) Matter-wave propagation velocities for the square (circular symbols), triangular (square symbols), and SNNN (diamond symbols) lattices for $L_x = 200$ and selected L_y. The horizontal lines show the maximal velocities calculated from band theory. The evolutions of the y-direction averaged density $\bar{n}$ for two selected cases indicated as b.1 (for the SNNN lattice) and b.2 (for the square lattice) are shown in panels b.1 and b.2. The wavefront arrival time at L_x (denoted by t^*) is determined by the time when $\bar{n}$ rises above a selected threshold. In this work we choose the threshold to be 0.05 as shown by the dashed lines in panels b.1 and b.2.

physics. Even more puzzling is that for the case of the SNNN lattice with $L_x = 200$ and $L_y = 2$, about half of the particles stay on the left half, and this causes a density discontinuity at $L_x/2$, which is visible on Figure 3.2(c). In contrast, for the SNNN lattice with $L_x = 200$ and $L_y = 3$ no density discontinuity can be observed. This indicates that $L_y = 2$ is special for the SNNN lattice.

By analyzing $\bar{n}$ as a function of t as shown in Fig. 3.2, one can estimate the time it takes for the wavefront to first arrive at a point i_x. For convenience, we take $i_x = L_x$ and measure t^* as the time when $\bar{n}$ reaches a threshold and extract the velocity $v = (L_x/2)/t^*$ for the three types of lattices shown in Fig. 3.1 as a function of L_y with $L_x = 200$ and present the data in Figure 3.3 (a). The details of $\bar{n}$ as a function of t for selected cases are shown in Figure 3.3 (b1) and (b2). The threshold is set to be 0.05 and the results do not change qualitatively with the choice. We remark that by measuring the spreading rate of the density profile shown in Fig. 3.2 and use the same threshold to determine the boundary of the density spreading, the same maximal propagating speed would be determined. The agreement is guaranteed by the light-cone spreading of noninteracting fermions shown in Fig. 3.2.

The geometry-dependent propagation velocity can be accounted for by the standard band theory for fermions [9]. For an infinitely large 2D uniform square lattice following the illustration of Fig. 3.1 (a), the energy band is ($k = (k_x, k_y)$)

$$\epsilon_S(k) = -2\bar{t}[\cos(k_x) + \cos(k_y)]. \tag{3.10}$$

The semiclassical velocity in the x-direction is

$$v_x^S = 2\bar{t}\sin(k_x). \tag{3.11}$$

Thus the maximal velocity in the x-direction is $2\bar{t}$, which is consistent with the numerical simulations for the square lattice. A complete derivation of dispersions can be found in Appendix A.3. Since k_x and k_y are decoupled, the result is independent of k_y so the maximal velocity already reaches the band-theory prediction when $L_y = 2$, as shown in Fig. 3.3 (a).

For the triangular lattice, the energy band is

$$\epsilon_T(k) = -2\bar{t}\left[\cos(k_x) + 2\cos(\frac{k_x}{2})\cos(\frac{\sqrt{3}k_y}{2})\right]. \tag{3.12}$$

The corresponding velocity is

$$v_x^T = 2\bar{t}\left[\sin(k_x) + \sin(\frac{k_x}{2})\cos(\frac{\sqrt{3}k_y}{2})\right]. \tag{3.13}$$

Unlike the square lattice, however, an important feature for this case is that k_x and k_y are mixed in the expressions. The maximal velocity is $2\bar{t}(1 + \sqrt{2}/2)$, which is larger than that in the square lattice. This k_y dependence also suggests that the L_y dependence will be more significant. Indeed, Fig. 3.3 (a) shows a stronger L_y dependence of the wavefront propagation velocity for the triangular lattice.

For the SNNN lattice, we first consider the infinite 2D lattice and defer the discussion of the special case of $L_y = 2$ to later. Since there are two intercalated sublattices (A and B), the energy band will split into two bands while the size of the first Brillouin zone is only half when compared to the previous two cases. The energy dispersion is

$$\epsilon_{SNNN}(k) = -4\bar{t}\cos(k_x) \pm \bar{t}g(k). \tag{3.14}$$

Here $g(k) = \sqrt{1 + 4\cos(k_x)\cos(k_y) + 4\cos^2(k_x)}$. The group velocity is

$$v_x^{SNNN} = 4\bar{t}\sin(k_x)\cos(k_y) \mp$$
$$\bar{t}[2\sin(k_x)\cos(k_y) + 4\cos(k_x)\sin(k_x)]/g(k). \tag{3.15}$$

A plot of the two bands at $k_y = \pi/a$ is shown in Figure 3.5. The two bands touch at four points in the first Brillouin zone so the system remains conducting for any filling less than the band insulator. The maximal velocity for the SNNN lattice is $6\bar{t}$.

As shown in Fig. 3.3, the wavefront velocity of the SNNN lattice approaches the maximal velocity as L_y increases, but the convergence is slower when compared to the

previous two cases. Fig. 3.2(d) shows many trailing wakes behind the first wavefront in the SNNN lattice case and they are the byproducts of the more complex dispersion (3.14). As a consequence, the averaged density $\bar{n}$ of the SNNN lattice rises less abruptly when compared to the other cases as shown in Fig. 3.3 (b.1) and (b.2). By estimating the velocity from the time when $\bar{n}$ rises above the selected threshold 0.05, an underestimation is in place. This can be improved by choosing a lower threshold of $\bar{n}$, although it would require more precise experiments to locate the lower-density threshold. The same issue persists if one measures the spreading rate of the cloud [123] because a threshold specifying the spreading front (separating the cloud and the vacuum or undisturbed regions) is needed.

The initial condition corresponds to a band insulator on the left half lattice. It has been shown that reducing the initial filling only reduces the magnitude of the current and the dynamics remains similar [33, 29]. One may use an initial configuration with finite total momentum, which may be realizable by filling up fermions in selected momentum states or imposing a momentum transfer. Since the spectral weight of the states are determined by the initial condition, the propagation will be biased towards the selected initial momentum. The maximal propagating speed, however, is determined by the lattice geometry and will not be changed by different initial states. Here we focus on fermionic transport because it has been shown that noninteracting bosons in the ground state will form a macroscopically coherent condensate and the transport is highly oscillatory [33]. In addition, at low temperature bosons stay in the bottom of energy bands, so they are insensitive to flat-bands which are at higher energies. For the purpose of probing the maximal propagating speed and flat-band physics, fermions are a better choice.

The honeycomb lattice, when the zig-zag side is placed along the horizontal direction, can be viewed as a deformed square lattice with alternating missing vertical links. In this case, the wavefront propagation velocity from the band theory and simulations are both identical to that of the square lattice when geometrical factors are properly considered. It is known the low-energy dispersion in the honeycomb lattice around the Dirac points
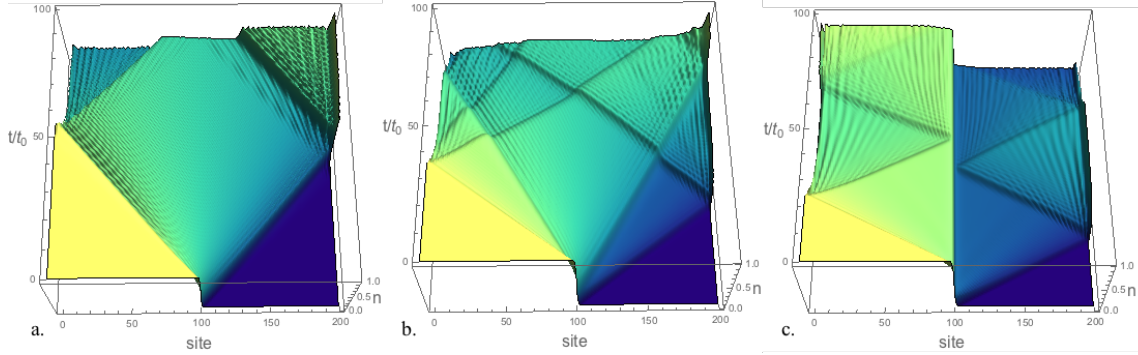
Figure 3.4: Evolution of the particle density with interaction $U/\bar{t} = 1$. Here the brighter regions correspond to higher density. (a) Square lattice. (b) Triangular lattice. (c) Two-leg SNNN lattice. Here $L_x = 200$ and $L_y = 2$.

resembles relativistic fermions [97]. For global transport studied here, the low-energy effects are not observable.

Band theory is no longer a good calculation of group velocity when interactions are added to the system. We provide numerical results in the small U limit, where the mean-field approximation applies, to determine interaction effects on the propagating wave front Figure 3.4. It is evident the presence of small interactions has minimal effect on the results with only a small increase in the time it takes to reach the boundary. The boost in wave propagation with the addition of diagonal links due to the mixing of transverse and longitudinal wave vectors is evident. Furthermore, the density discontinuity in the two-legged SNNN lattice remains present

3.4 Particle Localization and Flat band Effects

We now turn to the reason behind the density discontinuity of the two-leg SNNN lattice observed in Fig. 3.2. When $L_y = 2$, the Hamiltonian can also be diagonalized and the energy bands are

$$\epsilon(k_x) = -2\bar{t}\cos(k_x) \pm \bar{t}|1 + 2\cos(k_x)|. \tag{3.16}$$
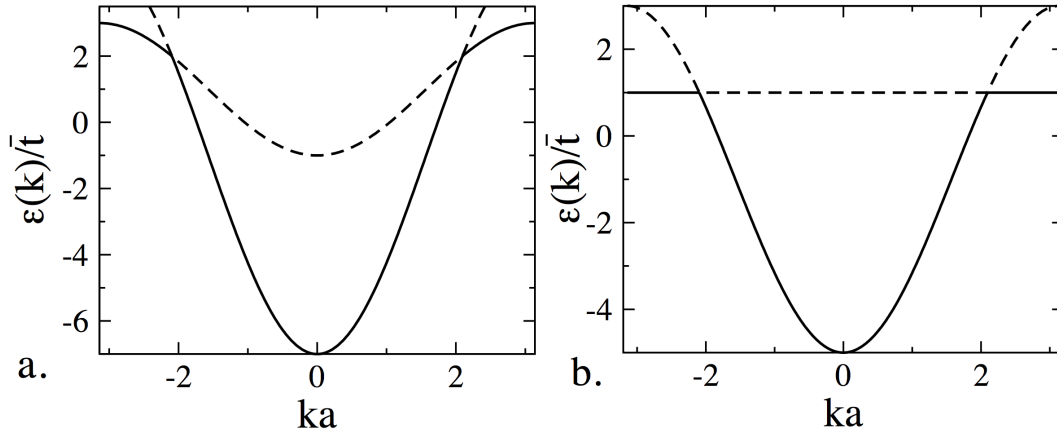
Figure 3.5: Energy bands of the (a) 2D SNNN lattice $k_y = \pi/a$ and (b) 1D SNNN lattice. The flat band appears from the overlapping of the bands and is intrinsic to the 1D lattice with equivalent tunneling coefficients on the diagonal, horizontal and vertical links.

The two bands are shown in Fig. 3.5(b). One important feature is that there is a flat band, i.e., a collection of dispersionless states. The particles on the flat band have localized spatial patterns so they do not participate in transport directly. For the two-leg SNNN lattice, the flat-band state corresponds to the wavefunction $\frac{1}{\sqrt{2}}\begin{pmatrix} 1 \\ -1 \end{pmatrix}$ localized on a vertical link. The tunneling from the two sites on a vertical link to any site to the left or to the right leads to a total destructive interference, which explains the localization. This also contrasts why $N_y = 2$ is special for the SNNN lattice because no such total destructive interference can be found in other values of N_y. In the presence of a chemical potential difference caused by the initial density difference, mobile atoms on the curved part of the dispersions are driven to the initial vacuum region.

The atoms on the flat-band, in contrast, remain in the initially filled region because their wave functions tend to localize. Since each momentum state can accommodate one fermion, on Fig. 3.5(b) the flat-band contains exactly L_x states. Thus, the flat-band states account for half of the total states (i.e., L_x out of the total $2L_x$ states). Therefore, the static property of the localized flat-band states is the reason for the density discontinuity.

By inspecting the particle density profiles at different time slots, we have verified that the density discontinuity does not decrease significantly as the wavefront propagates to the right. We also remark that, because fermions pile up from the lowest energy to the Fermi energy, the lower part of the dispersive band will be populated first. There are $(2/3)L_x$ states on the dispersive band below the energy of the flat-band as shown in Fig. 3.5(b). Thus, to observe the density discontinuity the initial filling on the left half lattice should exceed $1/3$ for the flat-band to be filled.

Such a flat-band induced dynamical density discontinuity may be generic in cold-atom systems. For instance, the kagome lattice has one flat band in its lowest three bands and quantum dynamics show that a density discontinuity of magnitude $1/3$ emerges as particles flow from an initially filled region into an initially empty region [29]. There is, however, a subtle difference between the flat band of the kagome lattice and that of the two-leg SNNN lattice. The kagome flat-band is on top of the other two dispersive bands while that in the two-leg SNNN intersects the other dispersive band. Nevertheless, their roles in transport are identical. While demonstrating such a dynamical density discontinuity is straightforward in cold-atoms systems, in conventional condensed matter depleting mobile electrons completely can be very challenging and observing this phenomenon can be a daunting task.

A few remarks on the two-leg SNNN lattice are worth mentioning. First, the existence of the flat band depends crucially on the condition of uniform tunneling coefficients. If the diagonal (A-A and B-B) links have a different tunneling coefficient $\bar{t}'$, the bands start to curve and there is no longer a flat band. We have tested the case for $\bar{t}' < \bar{t}$ and confirmed that the density discontinuity vanishes. However, when $\bar{t}'/\bar{t}$ is close to 1, the flat-band is bent only slightly and there is a transient time where an observable density difference (but not a discontinuity) gradually decays. The results look very similar to Fig. 3.2 (d). Secondly, in the presence of magnetic flux penetrating the ladder, the dispersion exhibits additional interesting features and the system is known as the Creutz ladder [40, 136] and transport in the square lattice with effective magnetic flux has been recently studied in
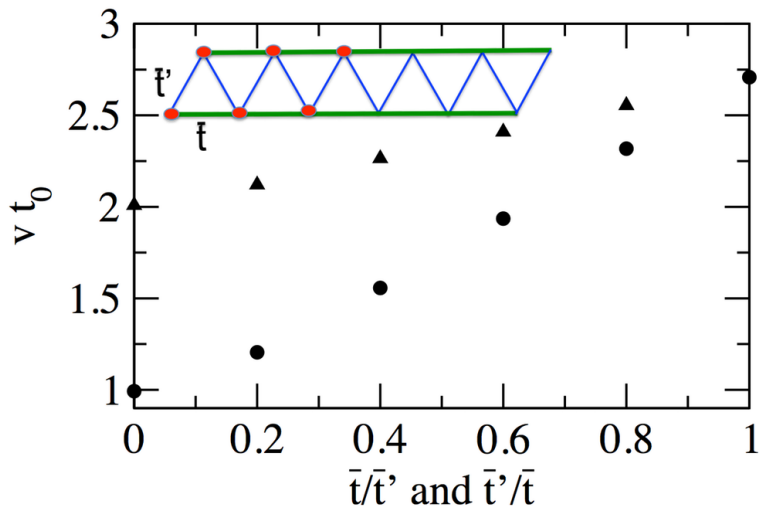
Figure 3.6: Adjustments to the tunneling coefficient ratio $\bar{t}/\bar{t}'$, where $\bar{t}' = 1$ and $\bar{t}$ is adjusted from 0 to 1(*circles*) increases the range of velocity when making the transition from the triangle lattice to the zig-zag lattice (*inset*). The range is decreased if $\bar{t} = 1$ and $\bar{t}'$ is adjusted from 0 to 1 (*triangles*).

cold-atom systems [10]. Here, we focus only on geometrical effects on transport.

3.5 Manipulating Matter-Wave Propagation by Controlling Nearest-Neighbor Tunneling

We end our discussion of geometrical effects on matter-wave propagation by presenting a possible application in the zig-zag lattice optical lattice [57, 150], which is basically a two-leg ladder of the triangular lattice as shown in the inset of Figure 3.6. The hopping coefficient along the horizontal direction is $\bar{t}$ and that along the diagonal is $\bar{t}'$, and the ratio between them are assumed to be continuously tunable. The initial condition is identical to the previous cases with the left half of the lattice being a band insulator and the right half being empty, as illustrated in Fig. 3.6.

When $\bar{t}' = 0$ and $\bar{t}$ gives the time scale t_0, the two legs decouple and it takes $L_x t_0/4$

for the matter wave to reach the far right boundary. In the opposite limit when $\bar{t} = 0$ and $\bar{t}'$ gives the same time scale t_0, it takes $L_x t_0/2$ because the particle has to traverse twice the distance to reach the far right boundary. The velocities are thus $2a/t_0$ and a/t_0 for the two limits. Figure 3.6 shows the velocity for selected values of $\bar{t}/\bar{t}'$ and $\bar{t}'/\bar{t}$. We chose the quantity in the denominator to give the same tunneling time scale t_0 to guarantee a fair comparison. Importantly, a maximal velocity appears when $\bar{t} = \bar{t}'$ when each site has the most available number of neighbors to tunnel into.

By tuning the ratio of the tunneling coefficients, a zig-zag optical lattice may serve as an atomic "gas pedal" for changing the speed of atoms passing through it. One possible scenario is to control the nearest-neighbor tunneling $\bar{t}$ while keep the next-nearest-neighbor tunneling $\bar{t}'$ fixed. When $\bar{t} = 0$, the velocity is slowed down to a/t_0. To accelerate the matter wave, one can tune to $\bar{t} = \bar{t}'$ and the velocity will be increased by 270%, according to Fig. 3.6. An experimental set up proposed for the zig zag lattice by superpositioning a triangular lattice and a strong optical superlattice [46, 14] could make such a gearing device feasible. Alternatively, the zig-zag lattice can be constructed by using both real and synthetic dimension [7] We emphasize that the zig-zag lattice tunes matter-wave propagating speed by the relative hopping strength of the two types of links (horizontal and diagonal) while the total current through the lattice is roughly maintained around a selected value because the total bandwidth does not change drastically. One may consider an alternative way of simply reducing the hopping coefficient of a uniform lattice to decrease the overall propagating speed, but this will reduce the total current due to the reduced bandwidth as well.

Similar applications may be relevant to quantum information transfer by controlling the group velocity of information carriers played by massive quantum particles. There have been experiments demonstrating information exchanges between photons and cold-atom matter-waves [52], where the propogation speed of the matter wave affects the overall transfer of the information. Our investigations into geometrical control of matter-wave propagation could provide additional manipulations of quantum systems.

3.6 Conclusion

It is apparent the geometry of the lattice affects the velocity of particles through the system. By adding diagonal links we increase the mixing of the wave vectors k_x and k_y which increases the maximum group velocity of the lattice. The SNNN lattice exhibited the fastest velocity of the wavefront due to it's maximum group velocity being a multiplicity of 3 higher than the square lattice. Control of the group velocity through an atomic system is of great relevance to quantum information transfer.

A flat band was observed in the 1D SNNN lattice when the hopping parameters are equivalent along the horizontal and diagonal links due to the overlap of energy bands. There is great interest in the study of flat bands and the SNNN lattice provides a way to discover physical properties resulting from a transition between a flat band system and a system without constant energy bands.

The tunability of the zig-zag lattice also provides an avenue for interesting physical phenomena. One can control the particle speed over a large range by merely tuning the hopping parameters. All predictions can be confirmed with aforementioned experimental setups.

I would like to acknowledge my co-authors Prof. Chih-Chun Chien, Prof. Gia-Wie Chern and Prof. Massimiliano Di Ventra for having this idea that sparked my interest in fermion transport.

Chapter 4

Dissipative Effects on Persistent Current in Continuum Model

Results on the hysteresis of dissipative current were published by the author in Ref [104] with permission to reproduce from Copyright (2016) American Physics Society.. Below a more detailed description is provided on the research results.

4.1   Motivation

Experimental advancements of cold atoms in optical potentials have renewed interest in the study of persistent current in mesoscopic rings. A 1D ring of particles can support a non-vanishing current in thermal equilibrium, known as persistent current, and is identical to magnetization [89, 3]. Recent work has focused on persistent current measurement of superfluid bosons, but studies of fermion persistent current in cold atoms remains theoretically and experimentally unexplored [120, 45, 37]. Past experiments studying persistent current in mesoscopic rings came across difficulties with interaction effects, but cold atoms provide a technique to measure the persistent current of non-interacting fermions in a ring[89, 28]. However, a lack of scattering mechanisms for

non-interacting fermions in optical potentials will be detrimental to the experimental measurement of a true, persistent current. Dissipation must be added to the system for it to settle into thermal equilibrium. Exchange of energy with a thermal bath relaxes the system and allows for a true, persistent current to be observed.

We shall demonstrate, not only is dissipation necessary for the observation of persistent current, but when the magnetic flux is periodically modulated hysteretic behavior can be observed. Hysteresis is a ubiquitous phenomena well studied in magnetic systems. Well known forms of hysteresis include ferromagnetic materials, superconductors, and superfluids, and it is known to be a significant mechanism in the advancement of modern electronics because it provides memory to a system and can cancel systematic effects[110, 71, 139]. Hysteresis arising from thermal relaxation occurs in two forms: rate-dependent hysteresis and rate-independent hysteresis[16]. The aforementioned systems are cases of rate-independent, where two or more metastable energy states are separated by an energy barrier and the free energy takes a non-linear form. Rate-independent hysteresis of persistent current in a rotating, superfluid Bose-Einstein Condensate (BEC) was observed and has been considered a milestone in the advancement of atomtronic circuitry [45]. Two local minima are dependent on the quantized angular momentum of the superfluid and the energy barrier is controlled by the potential of a weak link. After reaching a critical rotation the angular winding number changed between 0 and 1 leading to hysteresis loops of angular momentum.

Our study of persistent current in non-interacting fermions illustrates rate-dependent hysteresis of current, and cold atoms provide a means to explore this phenomena outside of magnetic systems. The competition between equilibrium and non-dissipative current leads to hysteresis of mass current when a periodically modulated artificial, magnetic flux and dissipation are added. Our results support a general approach to memory effects when the system responds to an external driving force and strengthen the case for the universality of hysteresis occurring in nature. Non-equilibrium memory effects of persistent current can be observed in cold atoms where exchange of energy with the environment can be

precisely tuned and dissipative techniques will be discussed.

Another interesting phenomenological result is the dependence of hysteresis loop area on relaxation time and which is connected to an overdamped harmonic oscillator. The area of a hysteresis loop determines how much energy is lost as heat from the system. Rate-independent hysteresis of ferromagnetic materials provides a common illustration of energy loss from a hysteretic process, and knowledge of the loss is highly important when ferromagnetic and ferroelectric materials are used in electronic systems [74]. The ability to form and magnetize domains depends on the material and determines how much energy is lost when the system undergoes a change in direction of the magnetic field. Hard magnets lose more energy during thermal relaxation processes thus requiring more energy to align with the magnetic field explaining why hard magnets make efficient memory systems. Energy loss from soft magnets is much less, which is why soft magnets are used in electronic systems. Behavior similar to hard and soft magnets is observable when calculating the areas for short and long dissipation times. It must be stated the illustration given is a different class of hysteresis, and the phenomena we observed is unique to rate-dependent systems. Rate-dependent behavior of energy loss is analogous to a particle overcoming viscous forces with relaxation time being inversely proportional to the friction coefficient. Examples of this behavior can be seen in Kramer's transition rate problem, and similar behavior has been predicted for thermal transport of atoms in a 1-D lattice coupled to a hot and cold bath on opposite boundaries.

Effects on hysteresis arising from interactions depends on whether the interaction affects the eigenstate. The formalism used to describe rate-dependent hysteresis only holds if the system does not redistribute with added flux and the eigenstate doesn't change as well. Two distinct cases of this type will also be discussed. Spin orbit coupling is of great interest since the use of artificial magnetic fields for cold, neutral atoms induce this interaction [94]. We demonstrate spin-orbit coupling doesn't lead to a superpostition of states, so the energies and currents are uniquely represented for each spin state. This is an important feature which allows us to use the rate-independent picture to describe the
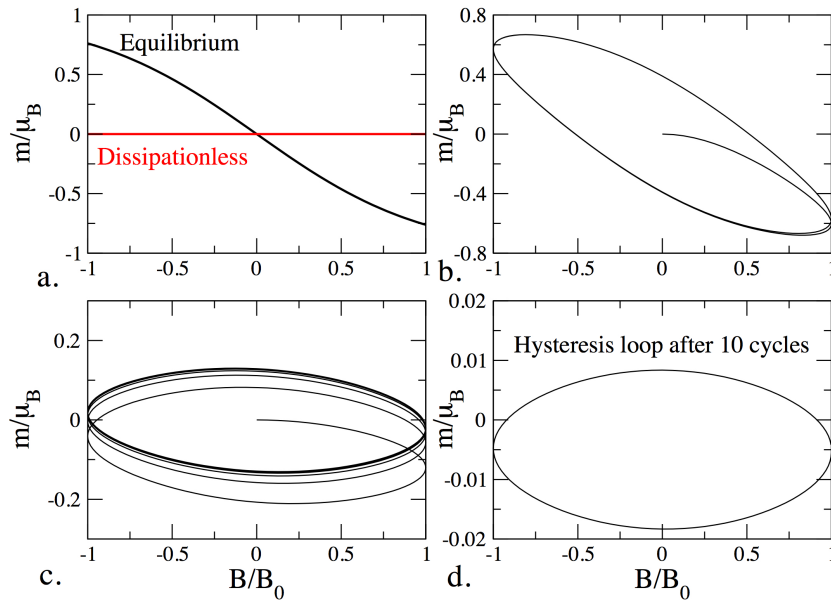
Figure 4.1: Hysteresis loops of total magnetization, m, over the normalized magnetic field, B/B_0. (a) The equilibrium (black) and non-dissipative (red) currents for the two-state spin system. Hysteresis of magnetization as flux is periodically modulated with a dissipation time (b) $\tau/t_p = 0.1$, (c) $\tau/t_p = 1$, (d) and $\tau/t_p = 10$.

system, and we show hysteresis arises in the presence of spin-orbit coupling.

4.2 Hysteresis by Thermal Relaxation

The principle behind memory effects, arising from thermal relaxation, can be demonstrated with a single spin subjected to a periodic magnetic field. Using this more simple, single body method the principle behind the many particle hysteresis mechanism can be elucidated. Extension to an n-state system follows the same formalism and can be calculated for an ultra-cold, fermionic persistent current by incorporating Fermi-Dirac statistics.

4.2.1   Two-State System

Two observable energy states are present as the spin aligns with the magnetic field in the $\hat{z}$ direction, $E = \mu B_z \sigma_z$, where σ_z is the Pauli matrix in the $\hat{z}$ direction, E is the energy, and μ is the magnetic moment. Probability of being either in the spin-up or spin-down state can be calculated by using the partition function with $\beta = 1/k_B T$ where k_B and T are Boltzmann's constant and temperature respectively.

$$P_\sigma = \frac{e^{-\beta \epsilon_\sigma}}{Z}$$

$$\begin{aligned} Z &= \sum_i e^{-\beta \epsilon_i} \\ &= 2\cosh(\beta \mu_B B) \end{aligned}$$

$$P_\uparrow = \frac{e^{-\beta \mu_B B}}{2\cosh(\beta \mu_B B)}$$

$$P_\downarrow = \frac{e^{\beta \mu_B B}}{2\cosh(\beta \mu_B B)}$$

The total equilibrium magnetization can be found by taking the difference of the probabilities.

$$\begin{aligned} m_{eq} &= \mu_B (P_\uparrow - P_\downarrow) \\ &= \mu_B \tanh(\beta \mu B(t)) \end{aligned} \tag{4.1}$$

Magnetization follows the black curve in Figure 4.1(a) in thermal equilibrium, but as the system is continually exposed to the periodic magnetic field $B = B_0 \sin(\omega t)$ energy is lost with relaxation. The period of the oscillating magnetic field $t_p = 1$ since we set the angular frequency $\omega = 2\pi$. The period of magnetic field oscillation sets the time unit for relaxation. The magnetization changes as energy is released to the environment as heat and can be determined over time with the relaxation approximation.

$$\frac{dm}{dt} = \frac{-(m(t) - m_{eq}(t))}{\tau} \tag{4.2}$$

where τ is the relaxation time. Relaxation time is the amount of time between scattering events and governs the rate of relaxation for the system. Relaxation of nuclear moments [18] and electron properties in metals [9] have been determined with the relaxation approximation and it proves to be robust when determining gross properties of the system.

Time-evolution of the magnetization is calculated from the solution of the first-order differential equation above (see next section for a full derivation).

$$m(t) = \frac{1}{\tau} \int_0^t e^{-(t-t')/\tau} \mu_B tanh(\beta\mu B(t'))dt' \qquad (4.3)$$

t_f is the amount of time energy is being dissipated. The relaxed distribution function and the corresponding time-dependent magnetization can be numerically calculated for both spin states Figure 4.1.

Evaluating the magnetization of the two state system in the presence of an oscillating magnetic field leads to clear memory effects if the relaxation time is on the order of the oscillating period. Three relaxation times are examined $\tau/t_p = 0.1, 1, 10$, and magnetization is plotted against the sinusoidal magnetic field over 10 periods Figure 4.1(b-d). Near close-loop hysteresis curves appear if the number of cycles is on the same order as the relaxation time, since the leading term in the time-evolution of probability is diminished when the final time $t_f \sim \tau$.

Memory effects arise from the periodicity of the distribution function in the dissipative integral. The exponential in the integral has a small value as $t \to t_f$, and the weight of the equilibrium distribution function becomes most dominant. A simple coordinate transformation $t' = t + 2t_p$ and $t'_f = t_f + 2t_p$ demonstrates the integrals over each period are equal since $P_{eq}(t') = P_{eq}(t)$. The leading exponential term carries more weight over the first period, but as time evolves the integral washes out contribution from the exponential, leading to the necessity of training cycles to close the loop. The effect is best illustrated when $\tau/t_p = .1$. Training cycles have been seen in the micro-states of artificial spin ice when subjected to a periodic magnetic field and self organization of nanoparticles

undergoing periodic shearing [70, 38].

4.2.2 Atomic Persistent Current in Ring Potential

Non-interacting fermion atoms in a ring trap are threaded with artificial magnetic flux along perimeter of the ring. In cold atom systems, a weak background interaction exists. However, the effect is small, and feedback only changes the effective mass and chemical potential. Memory effects arising in the derived current are not dependent on long range interactions and appear in the non-interacting regime. This contrasts previous work where memory effects appear due to long-range order [45].

The wave function of the non-interacting fermions can be described in the single particle picture due to the periodicity of the trap [21]. Fermions in the ring can be described in the single particle picture and the wave function is coherent in thermal equilibrium, allowing analytical solutions for the energy eigenvalues. Current will also be calculated with the Hamiltonian and single particle wave function.

The Hamiltonian describing the system is

$$H = \frac{1}{2m}(p_x + A)^2 \tag{4.4}$$

Momentum $p_x = -i\hbar\frac{\partial}{\partial x}$ and the quantized magnetic flux ϕ is derived from the vector potential $\Phi = AL = 2\pi\hbar\phi$ where L is the perimeter of the ring and m is atomic mass. The energy spectrum is obtained using the Schrödinger picture with a plane wave basis. An exact periodic wave function can be defined as

$$\psi_n = \sqrt{\frac{1}{L}}e^{ikx} = \sqrt{\frac{1}{L}}e^{i2\pi nx/L}$$

Crystal momentum $k = 2\pi n/L$ because of periodic boundary conditions implicit in the ring shape of the conducting structure. This wave function is exact for any vector potential, meaning the system need not redistribute as flux is added. Using the Hamiltonian and the plane wave function we can determine the energy eigenvalues:

$$-\sqrt{\frac{1}{L}}\frac{\hbar^2}{2m}(\frac{\partial}{\partial x} + \frac{2\pi i}{L}\Phi)^2 e^{i2\pi nx/L} = E\sqrt{\frac{1}{L}}e^{i2\pi nx/L} \tag{4.5}$$

$$-\frac{\hbar^2}{2m}(\frac{\partial}{\partial x}+\frac{2\pi i}{L}\Phi)(\frac{\partial}{\partial x}+\frac{2\pi i}{L}\Phi)e^{i2\pi nx/L} = Ee^{i2\pi nx/L} \tag{4.6}$$

After factoring the expression and operating the derivatives on the wave function, the energy eigenvalues

$$E_n = \frac{\hbar^2}{2m}(\frac{2\pi}{L})^2(n+\phi)^2 \tag{4.7}$$

are found to be periodic in $-0.5 < \phi < 0.5$, and are degenerate when $\phi = 0$. The added flux has no terms which support energy level crossing and if $\phi = 0$ Bohm's theorem states no equilibrium current will be present [147].

We will use the standard quantum mechanical definition of current

$$\frac{\partial \rho}{\partial t} = -\nabla \cdot j \tag{4.8}$$

$$\rho = \psi^*\psi \tag{4.9}$$

$$\frac{\partial \psi^*\psi}{\partial t} = \dot{\psi}^*\psi + \dot{\psi}\psi^* \tag{4.10}$$

Equating this with the time dependent hamiltonian yields the quantum current

$$(\frac{\partial \psi}{\partial t} = \frac{1}{i\hbar}H\psi)\psi^* + (\frac{\partial \psi^*}{\partial t} = \frac{1}{-i\hbar}H^*\psi^*)\psi \tag{4.11}$$

$$H^* = -\frac{\hbar^2}{2m}(\frac{\partial}{\partial x}-\frac{2\pi i}{L}\Phi)^2 \tag{4.12}$$

$$\frac{\partial \psi^*\psi}{\partial t} = \frac{i}{\hbar}H^*\psi^*\psi - \frac{i}{\hbar}H\psi\psi^* \tag{4.13}$$

This stems from the fact that the conjugate momentum operator acts on the conjugate wave function leading to a change in sign for the Hamiltonian. Below the normalization constant is pulled out of the wave function.

1.

$$\begin{aligned} H^*\psi^*\psi &= -\frac{\hbar^2}{2mL}(\frac{\partial}{\partial x}-\frac{2\pi i}{L}\Phi)(\frac{\partial}{\partial x}-\frac{2\pi i}{L}\Phi)\psi^*\psi \\ &= -\frac{\hbar^2}{2mL}(\frac{\partial^2}{\partial x^2}-2(\frac{2\pi i}{L})\phi\frac{\partial}{\partial x}+(\frac{2\pi i}{L})^2\phi^2)\psi^*\psi \end{aligned} \tag{4.14}$$

2.

$$H\psi\psi^* = -\frac{\hbar^2}{2mL}(\frac{\partial}{\partial x} + \frac{2\pi i}{L}\Phi)(\frac{\partial}{\partial x} + \frac{2\pi i}{L}\Phi)\psi\psi^*$$
$$= -\frac{\hbar^2}{2mL}(\frac{\partial^2}{\partial x^2} + 2(\frac{2\pi i}{L})\phi\frac{\partial}{\partial x} + (\frac{2\pi i}{L})^2\phi^2)\psi^*\psi \tag{4.15}$$

Putting these both together, I - II, we will find

$$\frac{\partial\rho}{\partial t} = -\frac{\hbar^2}{2mL}((\frac{\partial^2}{\partial x^2}\psi^*\psi - \frac{\partial^2}{\partial x^2}\psi\psi^*) - 2(\frac{2\pi i}{L}\phi)(\frac{\partial}{\partial x}\psi^*\psi + \frac{\partial}{\partial x}\psi\psi^*))$$
$$= -\frac{i\hbar}{2mL}(\frac{\partial}{\partial x}(\frac{\partial}{\partial x}\psi^*\psi - \frac{\partial}{\partial x}\psi\psi^*) - 2(\frac{2\pi i}{L}\phi)(\frac{\partial}{\partial x}(\psi^*\psi))) \tag{4.16}$$
$$= -\frac{i\hbar}{2mL}\frac{\partial}{\partial x}((\frac{\partial}{\partial x}\psi^*\psi - \frac{\partial}{\partial x}\psi\psi^*) - \frac{4\pi i}{L}\phi\psi^*\psi)$$

$$j_n = \frac{i\hbar}{2mL}(\frac{\partial}{\partial x}\psi^*\psi - \frac{\partial}{\partial x}\psi\psi^*) - \frac{4\pi i}{L}\phi\psi^*\psi \tag{4.17}$$

We can now insert our wave equation and work it through. Again the normalization constant was pulled out before hand.

$$j_n = \frac{i\hbar}{2mL}((\frac{\partial}{\partial x}e^{-i2\pi nx/L})e^{i2\pi nx/L} - (\frac{\partial}{\partial x}e^{i2\pi nx/L})e^{-i2\pi nx/L} - \frac{4\pi i}{L}\phi)$$
$$= \frac{i\hbar}{2mL}(-i\frac{2\pi n}{L} - i\frac{2\pi n}{L} - \frac{4\pi i}{L}\phi)$$
$$= \frac{-i^2\hbar}{2m}\frac{2\pi}{L^2}(2n + 2\phi) \tag{4.18}$$
$$= \frac{2\pi\hbar}{mL^2}(n + \phi)$$

The total current can be found by summing the current multiplied by the distribution function over all the energy states.

$$J_{Tot} = \sum_n j_n f_n \tag{4.19}$$

It is readily apparent the distribution function plays a critical role in determining the current, and a relaxation process is necessary to obtain dissipative current.

Persistent current is a thermal equilibrium phenomena, and if the system is not in equilibrium a current will be observed which is not "persistent." For instance, current
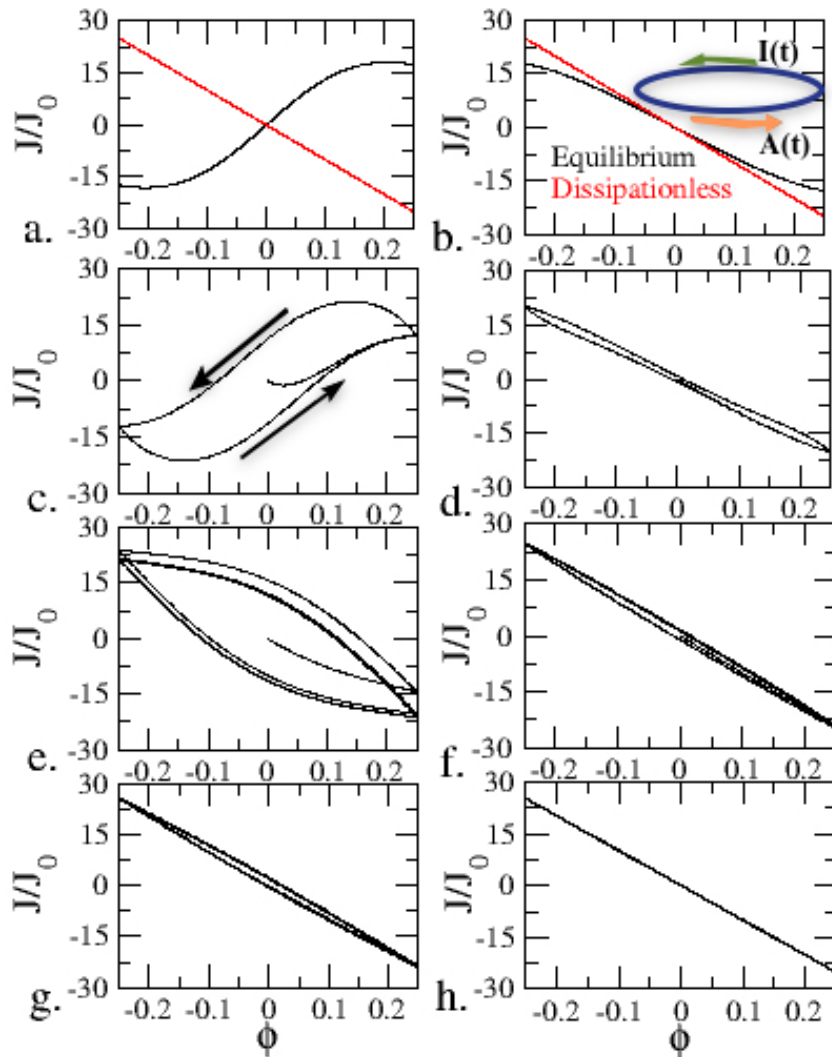
Figure 4.2: Hysteresis loops of total dissipative current J_{tot} over the flux ϕ at $T/T_0 = 10$. (a) The equilibrium (black) and no dissipative (red) currents for an $N_{tot} = 100$, left column (b) and $N_{tot} = 101$, right column, of particles. (b.inset) System setup. Dissipated current as flux is periodically modulated with a dissipation time (c,d) $\tau = 0.1t_0$, (e,f) $\tau = t_0$, (g,h) and $\tau = 10t_0$.

dependence on particle number is diminished as the system deviates from equilibrium which we quantify for an even, $N = 100$, and odd, $N = 101$, number of particles Figure 4.2(a,b). When the quantized flux is absent, $\phi = 0$, there will be no genuine, persistent current in the system and the particles reside in degenerate eigenstates.

Energy levels are smoothly distorted with added flux, and the particles don't redistribute for any value of ϕ. As flux is added the eigenvectors remain the same and only the eigenvalues change allowing the distribution function to provide an analytic description. Lack of particle redistribution can be problematic for direct observation of persistent current in cold atoms. First, the system is not in thermal equilibrium and a non-equilibrium current will be observed. Second, the particle at the Fermi surface highly contributes to the persistent current. As j_n is summed over all levels the current cancels if n and $-n$ are both occupied. Realizing a fermionic persistent current in a cold atom system requires some form of a relaxation process described theoretically by the relaxation approximation.

In metallic systems, at cold temperatures dissipation, is inherent because collisions occur from crystal defects and impurities in the crystal structure. A great characteristic about optical lattices is perfect periodicity, and scattering events must be added externally. The relaxation approximation is highly informative when seeking to understand gross properties of the system. It is a good tool to determine current as a function of time, $J(t)$, when energy is being removed by some scattering process. Useful methods for dissipating energy will be discussed in section IV.

To calculate the total current in thermal equilibrium we utilize the Fermi-Dirac distribution function with equation 10.

$$f_{n,eq} = \frac{1}{e^{\frac{(E_n - \mu)}{kT}} + 1} \tag{4.20}$$

The relaxation approximation for an n-level system governed by Fermi Dirac statistics will be appropriate for calculating dissipative current.

$$\frac{\partial f_n}{\partial t} = \frac{-(f_n - f_{n,eq})}{\tau} \tag{4.21}$$

where $f_{n,eq}$ is the equilibrium distribution function for the nth state and we assume the relaxation time τ is the same for all states [9]. The relaxation time determines the time an electron will experience a collision and in metals is roughly 10^{-14}s [17, 126, 122]. Incredibly fast collision processes for metals is a property of the material allowing for direct measurement of persistent current. The introduction of a collision process in a cold atoms system, though not on the same time scale, will permit measurement of the current as well. The method for collisions in cold atoms is tunable, and the investigation of multiple relaxation times leads to novel effects only observable with cold atoms.

We solve the differential equation to obtain the new relaxed distribution function

$$\frac{\partial f}{\partial t} = \frac{-(f - f_{eq})}{\tau} \tag{4.22}$$

$$\frac{\partial f}{\partial t} + \frac{1}{\tau}f = \frac{1}{\tau}f_{eq} \tag{4.23}$$

Equation 4.23 is a linear first order differential equation $\frac{dy}{dx} + p(x)y = q(x)$ The solution for this equation can be determined by multiplying the full expression by an integrating factor $\rho(x) = exp(\int p(x)dx)$, yielding the solution

$$y(x)e^{\int p(x)dx} = \int (Q(x)e^{\int p(x)dx})dx + C. \tag{4.24}$$

In the relaxation expression $y \to f$, $x \to t$, $p(x) = 1/\tau$, $q(x) = f_{eq}/\tau$, so

$$\rho(t) = e^{\int \frac{1}{\tau}dt} = e^{t/\tau}. \tag{4.25}$$

The solution for the relaxation approximation is as follows:

$$e^{t/\tau}\frac{\partial f}{\partial t} + e^{t/\tau}\frac{f}{t} = e^{t/\tau}\frac{f_{eq}}{\tau} \tag{4.26}$$

$$h\frac{\partial g}{\partial x} + g\frac{\partial h}{\partial x} = \frac{d}{dx}(gh) \tag{4.27}$$

$$\frac{d}{dx}(e^{t/\tau}f) = e^{t/\tau}\frac{f_{eq}}{\tau} \tag{4.28}$$

$$\int_0^{Tf} \frac{d}{dt}e^{t/\tau}fdt = \int_0^{Tf} e^{t/\tau}\frac{f_{eq}(t)}{\tau}dt \tag{4.29}$$

$$e^{Tf/\tau} f(T_f) - f(t=0) = \int_0^{Tf} e^{t/\tau} \frac{f_{eq}(t)}{\tau} dt \tag{4.30}$$

$$f_n(t_f) = e^{-tf/\tau} f_n(t=0) + \int_0^{tf} e^{-(tf-t)/\tau} \frac{f_{n,eq}(t)}{\tau} dt. \tag{4.31}$$

where t_f is the amount of time energy is being dissipated.

Since the energy changes with ϕ a different chemical potential is needed for each ϕ. We model the system as number conserving and by using the following relationship

$$N_{tot} = \sum_n \frac{1}{e^{\beta(E_n - \mu)} + 1}$$

a root finding method Appendix A.2.6 can be used to determine the chemical potential at equilibrium as the flux changes. In our simulation we exploit magnetic flux, ϕ, has a linear relationship with time $\phi = \frac{t}{2t_0}$, and $2t_0$ is the period of oscillation. Here t_0 is the ramping time of the flux over a half period, $0 \leq \phi \leq 0.5$. The number of time steps is given by $N_\phi = \frac{t_0}{dt}$ The root finding method is then embedded within a for loop running from 0 to N_ϕ and the resulting μ is placed in a one dimensional array to be called during computation of the distribution function over each time step. The Fermi distribution function was stored in a two dimensional array with the dimensions: $N_\phi \times N_{level}$.

Ramping time of the flux, t_0, is the fundamental time unit for calculations, and we are able to map how the dissipation function will change with flux as it oscillates between -0.25 and 0.25 with period $2t_0$. Time unit t_0 also sets the timescale for the relaxation time, τ/t_0, allowing analyzation of dissipative dependence on the ramping of the gauge field. Numeric integral calculations determine the new distribution function for each energy state as a function of time. The dissipated current, $J(t)$ can be determined as described in equation 6, and time easily is mapped back to flux as shown above.

Dissipative mechanisms are necessary to observe persistent effects in a cold atom system, or else a non-equilibrium current will be observed Figure 4.2(a,b). The added dissipation won't permit the observation of the true persistent current if the system is consistently, periodically modulated, and the current observed will lie somewhere

between the equilibrium and non-equilibrium current. If $t_0 >> \tau$ the system can settle into equilibrium and the true persistent current for fermions can be mapped out. However, more interesting effects can be explored with a periodic, driving flux.

The relaxed distribution function is evolved over 3 periods in the presence of dissipation, and the resulting current exhibits prominent hysteresis loops Figure 4.2. The dissipation time plays a strong role in the size of the loops and the number of cycles needed to close them. This is readily apparent in Figure 4.2.c and Figure 4.2.e where the dissipation times of $0.1t_0$ and t_0 differ by an order of magnitude, and the dissipated current tends to the non-equilibrium values with longer dissipation time.

4.2.3 Experimental Realization of Atomic Current Using Ultracold Fermions

Measurement of persistent current is achievable with current technology, and has already been facilitated for bosons in the superfluid phase using a rotating barrier as an artificial gauge[45]. The ring trap can be constructed by using LG beams for azimuthal confinement and a horizontal sheet beam for vertical confinement. Atoms are enabled to travel along the perimeter of the ring trap.

There have been a variety of methods to induce artificial gauge fields, which is done by finding methods mimicking the momentum shift due to the Lorentzian force [55]. In cold atoms, atom-light coupling from an external laser field causes an effective vector potential and corresponding magnetic field. Use of gauge fields from the coupling of the atoms and laser field is an advantageous tool, and has lead to measurements of new topological phases not realizable in condensed matter systems [134, 64].

For our purposes, an Abelian gauge field, where all the Cartesian components commute, will induce the effective magnetic flux in the ring trap. The direction of the gauge field is along the direction of lightwave momentum vector, so the light must propagate along the direction of the ring for a circular flux to be present. The LG beam

will serve as an appropriate tool to obtain a circular flux [69]. Modes of the beam can be selected from the angular momentum, l, and the value of l determines the accumulated phase as the atoms traverse the ring. If $l = 0$, no phase is accumulated which is equivalent to having no effective magnetic field. A momentum, $l = 1$, acts as an Abelian gauge field, which is the type needed to drive the current, because the system accumulates a phase of π. A non-Abelian gauge field can be selected when $l = 2$, but such a complicated field is not needed for the system in question.

The above methods address how to trap the atoms and create a synthetic flux, but the key component is the added dissipation. To bring the system to thermal equilibrium the fermions need to interact with the environment. In condensed matter systems, scattering of particles with impurities occurs on a fast timescale, allowing for persistent current to be observed. It is necessary to add a form of scattering to the particles trapped in the ring potential.

Introducing dissipation through Hamiltonian engineering has been highly useful for creating pure entangled states, and a variety of methods to couple the system to it's environment have been explore using electron beams and Bogoliubov excitations [12, 44, 43]. However, a more simple method, a Fermi-Bose mixture, will be most appropriate to realize the theoretical results. By immersing the fermions trapped in a ring potential into a Bose-Einstein Condensate (BEC), collisions between the two species can facilitate the dissipative processes caused by impurities in metals. The relaxation time $\tau(s)$ can be easily controlled by adjusting the number of bosons in the atom cloud and collisions occur on the millisecond timescale [113].

Particle loss is an apparent concern when artificially invoking collisions because the collision process can excite a fermion out of the potential barrier and can affect the direct observation of the number sensitive system. However it has been experimentally observed fermions experience very little loss while depletion of bosons is prominent [58]. The dynamics with a Bose-Fermi mixture are also in favor of experimental realization. It has been shown theoretically and experimentally the dissipative mechanism can induce a
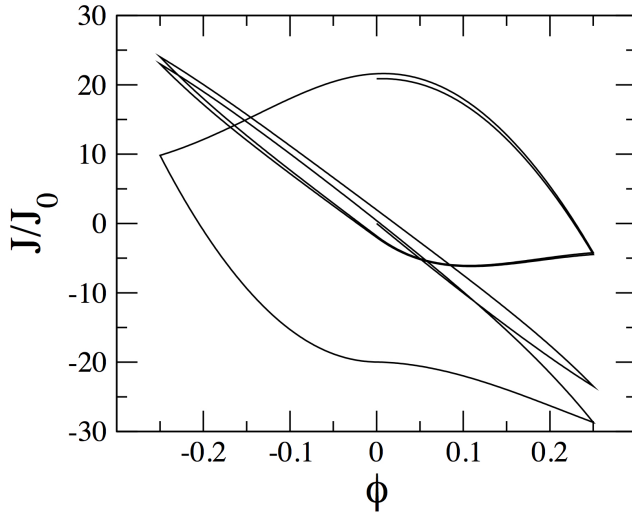
Figure 4.3: Hysteresis curve of the non-equilibrium current assuming one atom loss per driving cycle. Initially, there are N = 103 fermions and $\tau = 0.4t_p$ with a driving period of $2t_0$. We assume atom loss occurs are every 5τ increment. Here $T/T_0 = 10$. When atom loss occures randomly, the curve traverses both the even number and odd number structure after a couple cycles without closing.

current of non-interacting fermions in a periodic potential by acting as a driving force for an initially insulating phase [113, 116]. In direct contrast localization is observed in the boson cloud when interacting with fermionic impurities [112]. Measured current should be a pure, fermion current with the bosons merely interacting with the system as impurities in the perfect, periodic potential. Atom loss in the system results from inelastic collisions. Elastic and inelastic collision ration determines if the system can reach thermal equilibrium before atom loss is observable. Critical temperature range of measurements of trapped bosons is limited by the ratio [133], where a threshold of at least five elastic collisions per one inelastic collision is imposed. This threshold is expected to limit hysteresis of atom current observation in the strongly dissipative regime with small $\tau = t_p$. where t_p is the driving period. The system will experience atom loss in a few cycles if $1/\tau$ is an estimate of the elastic collision rate. Intermediate and weak dissipative regimes are less sensitive
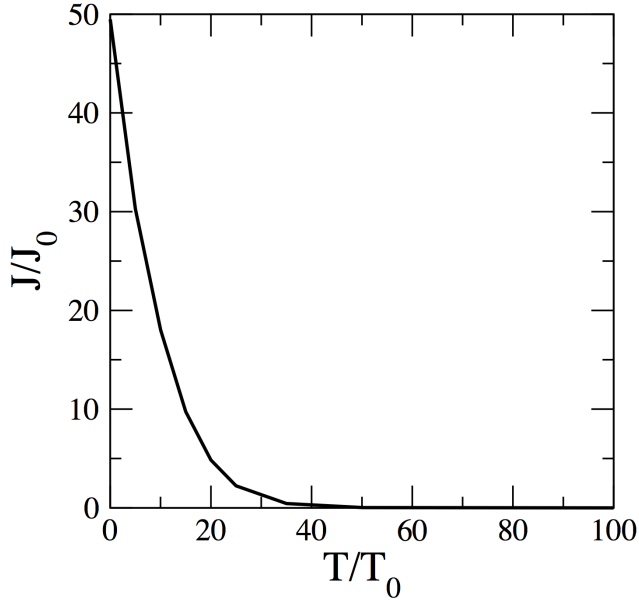
Figure 4.4: Maximal persistent current as a function of the normalized temperature T/T_0 for N = 101 fermions.

to atom loss since the hysteresis loops form before atom loss occurs. If we take the ration of 5 between elastic and inelastic collisions as an estimation of how soon atom loss will occur, curves are likely to be distorted is $\tau \leq 0.2t_p$. One atom lost per driving cycle is illustrated in Figure 4.3 with $\tau = 0.2t_p$. With a small relaxation time, current quickly relaxes to the case with one less particle after a fermion is lost. Atom loss occurs randomly in experiments, the nonequilibrium current is expected to switch between the even number and odd number curves when a fermion is lost, resulting in the current tracing both even and odd number cases after a few cycles. Atom loss will prevent hysteresis curves from forming closed loops. Atom loss will become a hindrance in mapping out the strongly dissipative regime.

Persistent current is highly sensitive to temperature, and the value decreases exponentially as heat is added Figure 4.4. The normalized Fermi temperature for

$N_{tot} = 101$ when $\phi = 0$ is

$$\frac{T_f}{T_0} = 2500$$

In order to observe current the system will need to be cooled to 1% of the Fermi energy to see the effects of persistent current. A previous experiment using mesoscopic, copper rings also reported an exponential decrease, but were able to measure current when the system was cooled to 80 mK since copper has a Fermi temperature of 8610K [89, 9].

4.3 Energy Dissipated by Relaxation and Connection to Classical Oscillator

Energy is released as heat during the relaxation process and this dissipated energy is the area of the hysteresis curve. By calculating the area how much energy is used for the relaxation process can be determined. For the two state system the energy is $E = \oint m \cdot dB$ and for the atomic current is $E = \oint J \cdot d\phi$. A narrow curve means the cycle over the flux requires less energy, and intuitively appears when τ is small because the system relaxes into thermal equilibrium easily. When τ is large the system tends to non-equilibrium values because the relaxation time is too long, leading to less work done in the dissipative process and a smaller hysteresis loop. For atomic current, energy loss has a dependence on the number of particles. More work is required for an even number of atoms because the difference of the non-equilibrium and equilibrium current is large, leading to areas an order of magnitude larger than the areas of odd numbers of particles.

The area of the hysteresis curve has a strong dependence on the rate of relaxation. The work done increases with a linear dependence on dissipation time, $E \propto \tau$, but after reaching a critical value the work done decreases inversely, $E \propto 1/\tau$ Figure 4.5. When fitted the two curves meet at the critical τ value, where the maximum amount of work can be done on the system and the largest loop is observed. Naively, this behavior can be explained through evaluation of the integral in equation 2, but closer evaluation
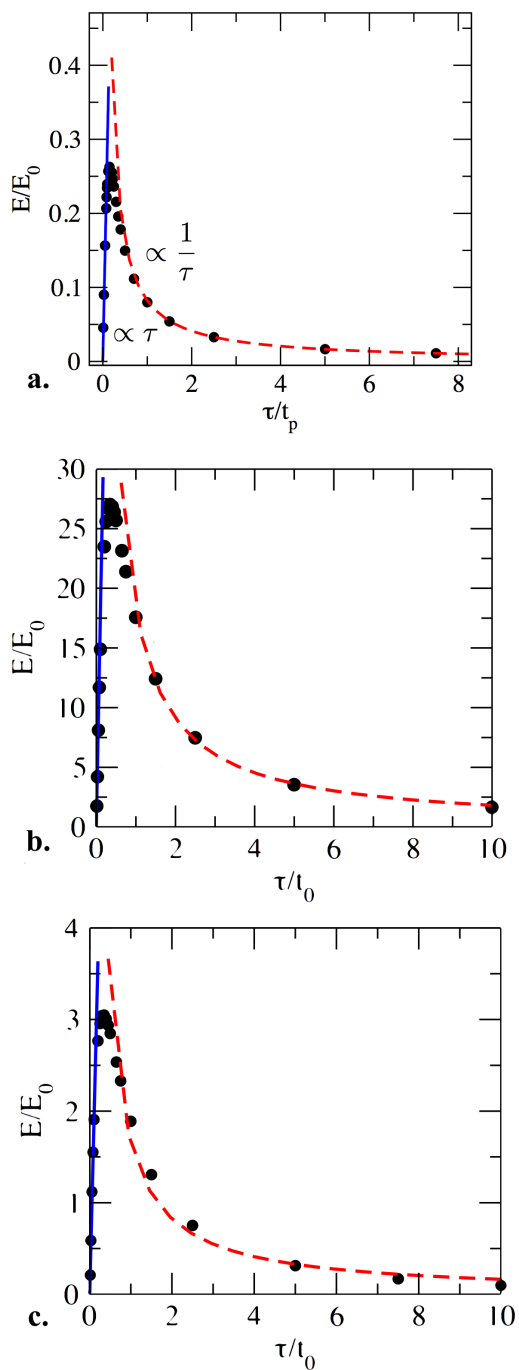
Figure 4.5: Energy loss as a function of the dissipation time τ for (a) magnetization of the two-state system, (b) dissipated current of N = 100 (c) and N = 101 fermions with $T/T_0 = 10$. Linear relationship $E \propto \tau$ (red) is apparent with small τ, and inverse relationship $E \propto 1/\tau$ (blue) with large τ.

demonstrates deep connections with the overdamped harmonic oscillator.

Energy dependence on the rate of relaxation arises from the relaxation approximation differential solution. Since, after several training cycles, the leading term is diminished only the relaxation time from the integral plays a role.

$$g(t) = \frac{1}{\tau} \int_0^t e^{-(t-t')/\tau} g_{eq}(t')dt' \tag{4.32}$$

Evaluation of the above equation in the small and large τ limits elucidates the behavior of dissipated energy. When $\tau >> T_p$ the value of the exponential is big allowing focus on the last cycle,

$$g(t) = \frac{1}{\tau} \int_{t-T_p}^t 1 g_{eq}(t')dt' \propto \frac{1}{\tau}$$

leading the area to decrease inversely with relaxation time. To evaluate $\tau << T_p$ we declare a small change $\epsilon(\tau)$ in time where $lim_{\tau \to 0}\epsilon(\tau) = 0$ since the exponential drops rapidly. The integral is then evaluated over this small change and the equilibrium distribution function can be considered constant over the infinitesimal change in time.

$$g(t) = \frac{g_{eq}(t)}{\tau} \int_{t-\epsilon(\tau)}^t e^{-(t-t')/\tau}dt'$$

By setting $\tilde{t} = t - t'$ the integral becomes

$$\begin{aligned} g(t) &= \frac{g_{eq}(t)}{\tau} \int_0^{\epsilon(\tau)} e^{-\tilde{t}/\tau}d\tilde{t} \\ &= g_{eq}(t)(1 - e^{-\epsilon(\tau)/\tau}) \end{aligned}$$

Expanding the infinitesimal change so $\epsilon(\tau) = a\tau + b\tau^2 + ...$ and the exponential becomes $1 - e^{-(a+b\tau)} = 1 - e^{-a}e^{-b\tau} = 1 - e^{-a}(1 - b\tau)$. Only first-order terms are considered with small τ and $g(t) = g_{eq}(t)(1 - e^{-a} + e^{-a}b\tau)$. The $lim_{\tau \to 0} g(t) = 0$ which means the constant term $a = 0$ leaving the linear dependence on the relaxation time $b\tau$.

Hysteresis due to a driving force in magnetism is dynamic hysteresis, and the dependence on relaxation time τ can be calculated explicitly in the high temperature limit

for the two-state system. The time dependent magnetization

$$\frac{dm}{dt} = \frac{-(m(t) - m_{eq}(t))}{\tau} \tag{4.33}$$

Magnetization of a system of particles, m, in equilibrium can be calculated from the difference of the two probabilities of being either in the up or down spin state depending on the direction of the magnetic field.

$$m_{eq}(t) = m_0 tanh(\beta\mu B(t))$$

$$m(t) = \frac{1}{\tau} \int_{-\infty}^{t} e^{-(t-t')/\tau} m_0 tanh(\beta\mu B(t'))dt'$$

In the high temperature limit the small angle approximation can be used and $m_{eq} = \chi_0 B(t)$ where $\chi_0 = m_0\beta\mu$ is a constant.

$$m(t) = \frac{\chi_0}{\tau} \int_{-\infty}^{t} e^{-(t-t')/\tau} B(t')dt' \tag{4.34}$$

$m(t)$ is magnetization responding to the field $B(t)$. The magnetic field acts as a driving force and by taking the Fourier transform of magnetization a susceptibility and frequency dependent magnetic field can be defined. The susceptibility $\chi(\omega)$ is the response function connecting magnetization with magnetic field, and generic analytical description can be found in reference [16].

$$m(\omega) = \chi(\omega)B(\omega) \tag{4.35}$$

$$= \int_{-\infty}^{\infty} m(t)e^{i\omega t}dt \tag{4.36}$$

Letting $e^{i\omega t} = e^{i\omega t'}e^{i\omega(t-t')}$ and substituting in equation 12 we find the solution for the frequency dependent magnetization

$$m(\omega) = \frac{\chi_0}{\tau} \int_0^{\infty} d(t-t')e^{i\omega(t-t')}e^{-(t-t')/\tau} \int_{-\infty}^{\infty} dt'e^{i\omega t'}B(t') \tag{4.37}$$

Evaluation of the susceptibility enlightens how dissipated energy depends on relaxation time.

$$\chi(\omega) = \frac{\chi_0}{\tau} \frac{1}{1 - i\omega\tau} \tag{4.38}$$

$$\chi''(\omega) = \chi_0 \frac{\omega\tau}{1 + \omega^2\tau^2} \tag{4.39}$$

Taking the high and low τ limits of the imaginary component of the susceptibility, $\chi''(\omega)$, the linear increase and inverse decrease of dissipated energy apparent.

A damped harmonic oscillator has a viscous damping force due to friction $f_\gamma = -m\gamma v$, a driving force f and spring constant k yielding the equation of motion $m\ddot{x} + kx + m\gamma\dot{x} = f$ [27]. Friction coefficient $\gamma = 1/\tau$ irreversibly depletes energy from the system into incoherent degrees of freedom, breaking the time-reversal symmetry of the simple harmonic oscillator. When the oscillator is overdamped, $\tau << 1$, the inertial term in the equation of motion can be ignored. In the case where $\tau >> 1$ the system can be mapped to the massless region of Brownian motion. The response function $\chi(\omega)$ of the overdamped oscillator yields the same solution as the two-state system.

$$\begin{aligned} \Delta E &= t_p P \tag{4.40} \\ &= \pi f_0^2 \chi''(\omega) \\ &= \pi U_0^2 \frac{\omega\tau}{1 + \omega^2\tau^2} \tag{4.41} \end{aligned}$$

where t_p is the period of oscillation, P is the power, and f_0 is the amplitude of the driving force. The rate of energy dissipation depends on $\chi''(\omega)$ implying Figure 4.5 is a universal phenomena for damped oscillators when the inertial term can be ignored.

The results above have been demonstrated in chemistry and thermal physics. The curve is most famously known in Kramer's transition rate theory when observing friction dependence for the transition rate of a particle moving out of a metastable well [61]. When friction is small most of the energy is used by particles transitioning out of the well, and the transition rate increases linearly. After the crossover point, where friction becomes large, more energy is lost to heat and the transition rate decreases hyperbolically. Similar effects are also observable when two heat reservoirs are connected by a 1D lattice [138]. Thermal conductance behaves similarly as friction forces are increased. Effects of friction are readily seen in the dynamics of the latter system because particles propagate ballistically with small friction and non-ballistically after the crossover point.

4.4 Interaction Effects on Hysteresis

Whether interactions effect the presence of hysteresis loops is relevant to the discussion. In order for hysteresis loops to appear with a periodic driving flux the eigenstates of the system can't change as flux is added to the system.

$$H(\phi = 0)\,|\psi\rangle = E(\phi = 0)\,|\psi\rangle \tag{4.42}$$

$$H(\phi > 0)\,|\psi\rangle = E(\phi > 0)\,|\psi\rangle \tag{4.43}$$

Interactions correlate the eigenstates with flux $\langle\psi(\phi = 0)|\psi(\phi > 0)\rangle \neq 1$. The system with dissipation can't be evolved using the relaxation approximation and hysteresis won't be observed. This is evident in a two particle system with an elementary delta interaction. However, this does not encompass all types of interactions. The presence of spin-orbit coupling only effects the eigenvalues as flux is added to the system and hysteresis is still apparent.

4.4.1 Time-Dependent Ground State

For the two-state system and ring current we construct the formalisms with magnetic field $B_z\hat{z}$. What if the magnetic field was not one dimensional and took the form $B_x\hat{x} + B_z\hat{z}$? The corresponding Hamiltonian

$$H = B_x\hat{\sigma}_x + B_z(t)\hat{\sigma}_z \tag{4.44}$$

yields orthogonal eigenstates for the energies

$$E_\pm = \pm\sqrt{B_z(t)^2 + B_x^2}$$

$$|n, t\rangle_+ = \frac{1}{N_-}\begin{pmatrix} -B_x \\ B_z(t) - \sqrt{B_z(t)^2 + B_x^2} \end{pmatrix} \tag{4.45}$$

$$|n, t\rangle_- = \frac{1}{N_+}\begin{pmatrix} -B_z(t) + \sqrt{B_z(t)^2 + B_x^2} \\ -B_x \end{pmatrix} \tag{4.46}$$

with N being a normalization factor. As time evolves the magnetic field $B_z(t)$ changes the eigenstate of the system since $\langle n, t_1 | n, t_2 \rangle \neq 1$. With each incriment of time not only the eigenvalues but the eigenstates must be reevaluated. This implies the system redistributes throughout the energy states with the changing driving field. This not only negates the usage of the distribution function to describe the system, but the current formalism, which depends on the energy states, also evolves with the driving field.

Interactions correlate Eigen energy states, demonstrable with a simple delta interaction between two particles. Use of a Beth Ansatz to match the boundary conditions of the wave function results in the wave vectors of the particles correlating [137]. Adjustment of one particle's momentum state leads to an inverse effect in the other, so the wave functions can't be treated separately. Relaxation processes for a system with wave functions dependent on each other is best not described by the distribution function and relaxation approximation since particle distribution will be effected by change in the momentum state. It is evident strong interactions between particles inhibit the formation of hysteresis loops in a periodically driven system.

4.4.2   Hysteresis with Rashba Spin Orbit Coupling

It is worthwhile to explore whether hysteresis loops of charge current are maintained in the presence of Rashba spin-orbit coupling (RSOC). Coupling of electron spin to momentum in a single atom arises from an effective field produced by the moving electron cloud in the inertial reference frame of a single electron. Spin-orbit interactions in cold atoms are engineered with the same experimental technique as artificial gauge fields [94]. Coupling is induced in dressed atomic states by a pair of Raman lasers and the coupling strength is dependent on the momentum k_L of the laser. Experimentally, spin-orbit coupling is inherent in systems which use artificial gauge techniques. We demonstrate the memory effects occur in the presence of SOC and observation of hysteresis is readily accessible in ultra-cold atoms.
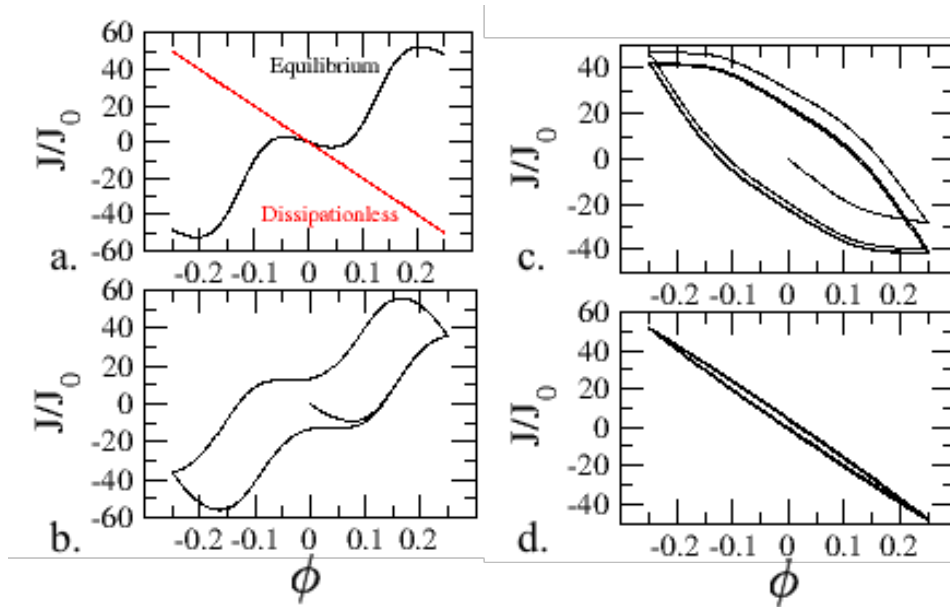
Figure 4.6: The total current, J/J_0, over the flux, ϕ with SOC at $T/T_0 = 3$ and $\alpha/E_0 = 0.75$. (a) The equilibrium (black) and non-equilibrium (red) currents for $N_\uparrow = N_\downarrow = 100$ particles. Dissipated current as flux is periodically modulated with relaxation times (b) $\tau/t_0 = 0.1$, (c) $\tau/t_0 = 1$, (d) and $\tau/t_0 = 10$.

The Hamiltonian of electrons traversing a 1D ring on the xy-plane acquires an extra coupling term dependent on a perpendicular external field $E\hat{z}$. Vector potential is in the azimuthal direction $A\hat{\theta}$. The Zeeman term arising from an external magnetic field is ignored since it's merely constant addition to the energy and demonstrates little effect on the persistent charge current.

$$H = \frac{1}{2m}(p - eA)^2 + \alpha\hat{\sigma} \cdot (E \times (p - eA)) + V(r) \tag{4.47}$$

The spin, given by the Pauli matrix $\hat{\sigma}$, couples to the momentum with coupling strength α. In order for the Hamiltonian to be Hermitian a harmonic confining potential $V(r) \propto x^2$ is added, where $x = (r - a)$ is the width of the confining potential with a being the ring radius [101]. Once the Hamiltonian has been formulated the confining potential can be taken in the 1D limit $r \to a$ and $V(r) \to 0$. Moving into cylindrical coordinates where

$\hat{\sigma}_r = \hat{\sigma}_x cos(\theta) + \hat{\theta}_y sin(\phi)$ and $\hat{\sigma}_\theta = \hat{\sigma}_y cos(\theta) - \hat{\sigma}_x sin(\theta)$ and using the previously defined relationship between A and ϕ the Hamiltonian becomes

$$
\begin{aligned}
H &= -\frac{\hbar^2}{2m}\left[\frac{\partial^2}{\partial r^2} + \frac{1}{r}\frac{\partial}{\partial r} - \frac{1}{r^2}(i\frac{\partial}{\partial \theta} + \frac{\phi}{\phi_0})^2\right] \\
&\quad -\frac{\alpha}{r}\hat{\sigma}_r(i\frac{\partial}{\partial \theta} + \frac{\phi}{\phi_0}) + i\alpha\hat{\sigma}_\theta\frac{\partial}{\partial r} + V(r)
\end{aligned} \tag{4.48}
$$

Separating the radial and azimuthal variables $H = H_r + H_\theta$ allows for the lowest radial mode, $R_0(r) \propto e^{(r-a)^2}$ to be determined from the solution to the simple harmonic oscillator. The hermitian Hamiltonian $H_{1D} = \langle R_0|H_\phi|R_0\rangle$ is found to be

$$
H_{1D} = -\frac{\hbar^2}{2ma^2}(i\frac{\partial}{\partial \theta} + \frac{\phi}{\phi_0})^2 - \frac{\alpha}{a}\hat{\sigma}_r(i\frac{\partial}{\partial \theta} + \frac{\phi}{\phi_0}) - i\frac{\alpha}{2a}\hat{\sigma}_\theta \tag{4.49}
$$

Completing the square the Hamiltonian can be simplified to

$$
H_{1D} = \hbar E_0(i\frac{\partial}{\partial \theta} + \frac{\phi}{\phi_0} + \frac{\alpha}{2E_0}\hat{\sigma}_r)^2
$$

with $E_0 = \hbar/2ma^2$. Using the relationship $\sqrt{H}\psi = \sqrt{E}\psi$ and the following spinor formulation

$$
\psi_n^\pm = e^{in\theta}\begin{pmatrix} a_n^\pm \\ e^{i\theta}b_n^\pm \end{pmatrix} \tag{4.50}
$$

we can obtain the energy eigenvalues

$$
E_{n,-} = \hbar E_0\left((n - \phi) + \frac{1}{2}(1 - \sqrt{(\alpha/E_0)^2 + 1})\right)^2 \tag{4.51}
$$

$$
E_{n,+} = \hbar E_0\left((n - \phi) + \frac{1}{2}(1 + \sqrt{(\alpha/E_0)^2 + 1})\right)^2 \tag{4.52}
$$

Using the following relationship for the eigenfunction coefficients

$$
\frac{E_0}{\alpha}(1 \pm \sqrt{(\alpha/E_0)^2 + 1})a_n^\pm = b_n^\pm \tag{4.53}
$$

the eigenstates can be composed into trigonometric relationship with $1/cos(\theta) = \sqrt{(\alpha/E_0)^2 + 1}$

$$
\psi_n^+ = e^{in\theta}\begin{pmatrix} cos(\frac{\theta}{2}) \\ e^{i\theta}sin(\frac{\theta}{2}) \end{pmatrix} \tag{4.54}
$$

$$\psi_n^- = e^{in\theta} \begin{pmatrix} sin(\frac{\theta}{2}) \\ -e^{i\theta} cos(\frac{\theta}{2}) \end{pmatrix} \tag{4.55}$$

No dependence on changing flux is present in the eigenstates, meaning only the energy eigenvalues change as flux is added. This allows the system to be treated with the relaxation approximation, and current with changing flux can be determined.

The current can be found by taking the full derivative of the energy with respect to flux, $j_n = -dE_n/d\phi$, and for the two spin states becomes

$$j_{n,-} = j_0 \left((n - \phi) + \frac{1}{2}(1 - \sqrt{(\alpha/E_0)^2 + 1}) \right) \tag{4.56}$$

$$j_{n,+} = j_0 \left((n - \phi) + \frac{1}{2}(1 + \sqrt{(\alpha/E_0)^2 + 1}) \right) \tag{4.57}$$

when $j_0 = 2\hbar E_0$. Dissipated current in the presence of RSOC interactions can be evaluated using the relaxation approximation in same fashion as non-interacting fermions. We again implement the Fermi-Dirac statistics for the $E_{n,+}$ and $E_{n,-}$ energy states.

$$f_{n,+} = \frac{1}{e^{\frac{(E_{n,+} - \mu)}{kT}} + 1} \tag{4.58}$$

$$f_{n,-} = \frac{1}{e^{\frac{(E_{n,-} - \mu)}{kT}} + 1} \tag{4.59}$$

Chemical potential can be determined with a root finding method when evaluating $N_{tot} = N_\uparrow + N_\downarrow$ from the distribution functions

$$N_{tot} = \sum_n (f_{n,+} + f_{n,-})$$

The total equilibrium and dissipated current for each state can be found by summing the current multiplied by the distribution function over all levels $J_{Tot,\pm} = \sum_n f_{n,\pm} j_{n,\pm}$. Adding these two currents together we find $J_{Tot} = J_{Tot,-} + J_{Tot,+}$. To determine the dissipated current we relax the distribution function using the relaxation approximation for $f_{n,+}$ and $f_{n,-}$ separately.

$$\frac{\partial f_{n,\pm}}{\partial t} = \frac{-(f_{n,\pm} - f_{n,\pm,eq})}{\tau} \tag{4.60}$$
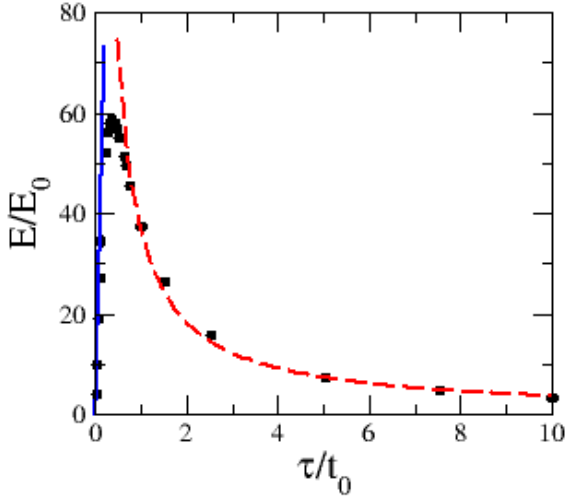
Figure 4.7: Area of hysteresis loop with SOC at $T/T_0 = 3$ and $\alpha/E_0 = 0.75$ as relaxation time τ is increased.

The total current is then plotted against the periodic, driving flux with $\alpha/E_0 = 0.75$. Persistent current in the presence of RSOC is highly sensitive to temperature, so we set $T/T_0 = 3$ for current calculations. As flux is added the eigenstates do not change where in the previous interaction cases the system energy would have to be reevaluated with each additional increment of flux. Hysteresis loops are observable for $N_\uparrow = N_\downarrow = 100$ with spin-orbit interactions Figure 4.6(a-d), and loops for $N_\uparrow = N_\downarrow = 101$ are observable with parameter adjustment .

We focus on an even number of particles when evaluating the dependence of energy lost on dissipation time. Since the memory effects with RSOC can still be described in the framework of rate-dependent hysteresis the linear increase and hyperbolic decrease of energy with dissipation time holds true Figure 4.7. Therefore RSOC interactions induced by the artificial gauge field should not inhibit the ability for experimental measurement and observation of hysteresis due to relaxation towards the persistent current.

4.5   Conclusion

Hysteresis loops of current have been demonstrated to exist for non-interacting fermions confined in a 1D ring potential with added dissipation. The memory of the current is a direct result of the periodicity of the distribution function with time, and after a few training cycles memory effect are apparent. Energy loss strongly depends on the rate of relaxation and exhibits characteristics of an overdamped oscillator. If τ is small compared to the ramping of flux the area of the curve increases linearly with τ. As τ becomes greater than the period of oscillation the area of the curve decreases inversly with τ. The observed phenomena is analogous to effects observed in Kramer's transition rate problem, thermal transport, and is a general property of rate-dependent hysteresis.

Cold atom hysteresis is a milestone in for the development of atomtronics along with rapid loading of atoms [88], portable cold atom systems [124], and entropy reduction [143]. Experimental implementation and observation is feasible in cold atoms with current technology. Hysteresis loops will still be observable with spin-orbit coupling interactions, arising in the system due to the use of gauge field techniques. Cooling is the limiting factor for observation of persistent current since persistent current decays exponentially with temperature. Usage of rate-independent systems will be more robust for atomtronic memory applications, but we prove the system need not be in a superfluid state for observation of closed loop hysteresis. The need for added dissipation in cold atom systems motivates these results, which will not be observable in metal systems, and is and exciting phenomena readily awaiting experimental observation. In future work it would be of interest to explore whether hysteretic behavior can be observed in other non-equilibrium, cold atom systems where a periodic distribution function appears.

Chapter 5

Current Fluctuations and Resulting Lissajous Curves

A mesoscopic lattice with closed boundaries supports an equilibrium current periodic in magnetic flux, and as an equilibrium current the corresponding current fluctuations are purely quantum. These fluctuations form continuous peaks with the addition of contact interactions in the lattice; this is a stark contrast from the non-interacting system where the current and fluctuations possess a discontinuity. Current and current fluctuations are both periodic nature, revealed as Lissajous curves when plotted together. In the non-interacting system the Lissajous curve is single-valued, but the curve becomes multivalued with the addition of contact interactions, revealing a topological distinction between the two systems. Magnetic systems also show Lissajous curves arising from memory effects in the magnetization, and the existence of similar curves spurs curiosity to whether equilibrium current and current fluctuations play a similar role.
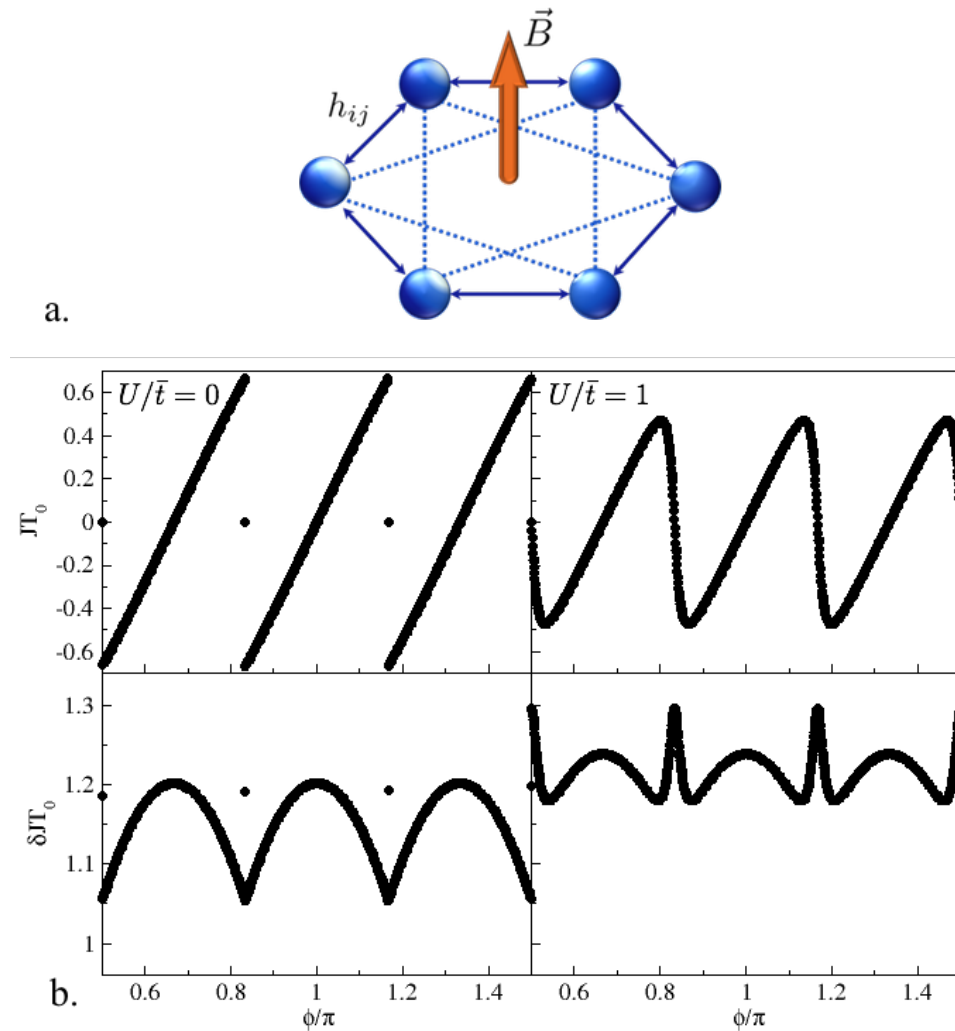
Figure 5.1: (a) Schematic plot of a benzene-like lattice encircling a magnetic field perpendicular to the plane. The hopping coefficient from site i to site j is h_{ij}. The onsite coupling constant is U. (b) Ground-state persistent currents (top row) and current fluctuations (bottom row) as functions of the Peierls phase ϕ. The left (right) column corresponds to the noninteracting (interacting, $U/\bar{t} = 1$) case. Here $N_\uparrow = N_\downarrow = 3$, $\bar{t} =$ is the hopping energy scale, and $T_0 = \hbar/\bar{t}$.
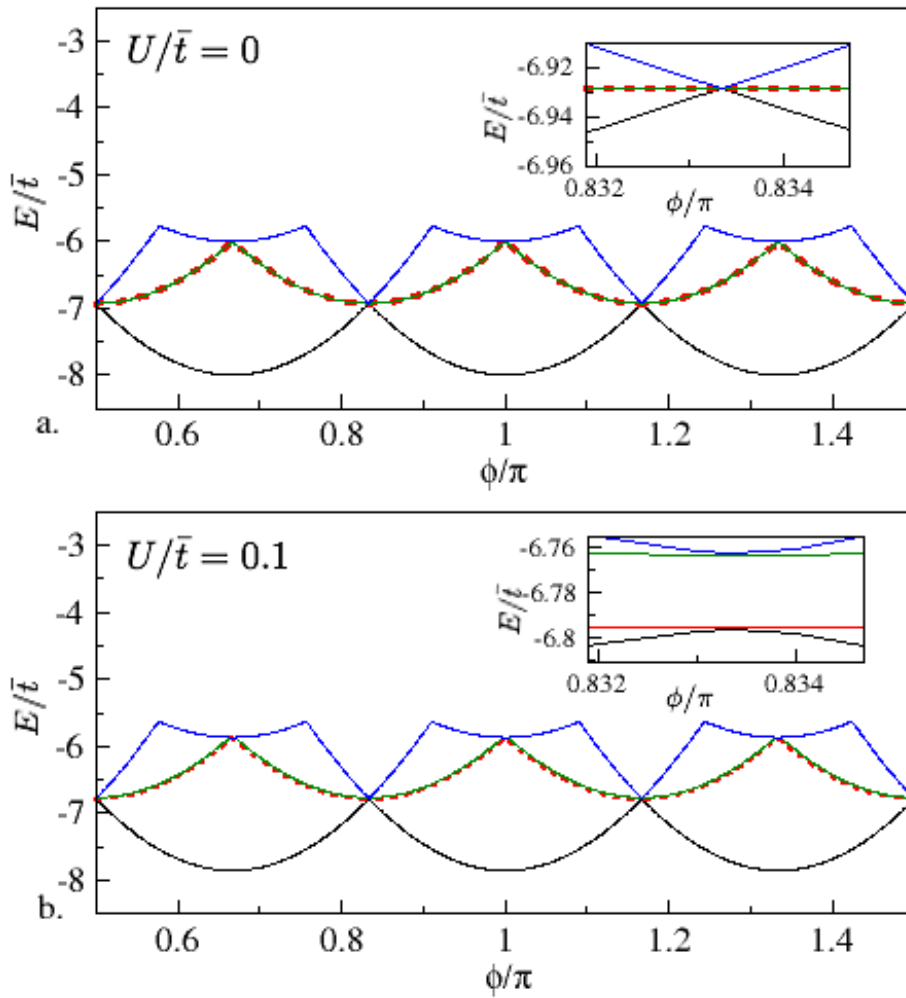
Figure 5.2: Energies of the lowest four states as functions of the Peierls phase ϕ of a half-filled 6-site lattice loaded with (a) non-interacting and (b) weakly interacting ($U/\bar{t} = 0.1$) fermions. The insets show magnified views around the degeneracy point.

5.1 Current and Current Fluctuations in Quantum Lattice Ring Threaded With Magnetic Flux

Consider a one-dimensional discretized ring with a total of six sites and half-filled with $N_\uparrow = N_\downarrow = 3$, like a benzene ring. Here $\sigma =\uparrow, \downarrow$ denote the spin. When the system is in the ground state, particles generate a persistent current in the ring when subjected to a perpendicular magnetic field Fig 5.1(a) [149, 4, 140, 79]. Employing the Hubbard tight-binding model the magnetic field induces a Peierls phase [114, 75] ϕ as they tunnel from an occupied site to an adjacent site

$$H = \sum_{i \neq j, \sigma} h_{ij} c_{i\sigma}^\dagger c_{j\sigma} + U \sum_i n_{i\uparrow} n_{i\downarrow}. \tag{5.1}$$

The creation(annihilation) operator $c_i^\dagger(c_j)$ accounts for a fermion moving from site j to site i. The off-diagonal matrix element $h_{ij} = h_{ij}^*$ represents the hopping coefficient between site i and site j. In the case of nearest-neighbor tunneling $h_{i,i+1} = \bar{t} e^{i\phi}$ where ϕ is proportional to the magnetic field strength and $\bar{t}$ is the hopping strength. The energy unit is $\bar{t}$ and the time unit is $T_0 = \hbar/\bar{t}$. Onsite contact interactions with strength U between particles of opposite spin account for the dominant interaction in the ring lattice. Using the exact diagonalization numerical technique the ground state energy and wave function can be calculated exactly for a half-filled, six sited lattice. No approximations were used in diagonalization of the Hamiltonian. Plotting the ground-state and first-excited state energy as a function of the magnetic flux ϕ, it is apparent the system is periodic in flux with a period $T_\phi = \pi/3$ and a degeneracy point at the end of each period Fig 5.2(a).

A non-interacting ring with next-nearest neighbor hopping has degeneracy points periodic in magnetic flux Fig 5.2. Particles in occupying a degenerate point have the same energy while occupying different states. In the hexagonal ring there is a fourth ordered degenerate point where the current is zero, causing the discontinuity in current and fluctuations. Interactions between particles lifts the degeneracy and can be simply

demonstrated using perturbation theory. The degeneracies from the hopping Hamiltonian between the four states can be described as diagonal elements on a four-by-four Hamiltonian matrix. Off-diagonal terms mixing the states are introduced by interactions acting on all Fock states, and the corresponding eigenvalues are no longer degenerate. Even in a very weakly interacting system the degeneracy is lifted Fig 5.2(b) enabling the current and fluctuations to be continuous in flux.

Starting from the time evolution of the density matrix, the local current operator between sites can be described in second quantization as

$$J_{ij} = i(h_{ij}c_i^\dagger c_j - h_{ij}^* c_j^\dagger c_i) \tag{5.2}$$

where h_{ij} is the Hamiltonian off-diagonal element corresponding to the connection between site i and j. In quantum measurement theory the probabilistic nature of the wave function leads to fluctuations in measurement. Statistically, these fluctuations are quantified as a variance $(\Delta A)^2$ and standard deviation ΔA from the mean. Fluctuations of the local current for a single spin component are

$$\langle \delta J_{ij}^2 \rangle = \langle J_{ij}^2 \rangle - \langle J_{ij} \rangle^2 \tag{5.3}$$

$$\langle J_{ij}^2 \rangle = \left| h_{ij} \right|^2 \big[\langle n_i \rangle + \langle n_j \rangle - 2\langle n_i n_j \rangle \big]. \tag{5.4}$$

However, it is worth considering the contributions of the total current and corresponding fluctuations from both spin components. The total current is a sum of the contributions for both species

$$\langle \mathcal{J} \rangle = \langle J_\uparrow \rangle + \langle J_\downarrow \rangle, \tag{5.5}$$

and the fluctuations have a more complicated structure than single component

$$\langle \delta(\mathcal{J})^2 \rangle = 2\langle J_\uparrow^2 \rangle + 2\langle J_\uparrow J_\downarrow \rangle - 4\langle J_\uparrow \rangle^2. \tag{5.6}$$

With an equal population of both species $J_\uparrow = J_\downarrow$ and working in the non-interacting limit, Wick decomposition can be used to show

$$\langle \delta(\mathcal{J})^2 \rangle = 2(\langle J_\uparrow^2 \rangle - \langle J_\uparrow \rangle^2) \tag{5.7}$$

since all the cross-component terms cancel. With the addition of interactions the full expression for the expectation of cross-component current correlations

$$\langle J_\uparrow J_\downarrow \rangle = -(\langle h_{ij\uparrow} h_{ij\downarrow} c_{i\uparrow}^\dagger c_{j\uparrow} c_{i\downarrow}^\dagger c_{j\downarrow} \rangle - \langle h_{ij\uparrow} h_{ij\downarrow}^* c_{i\uparrow}^\dagger c_{j\uparrow} c_{j\downarrow}^\dagger c_{i\downarrow} \rangle -$$
$$- \langle h_{ij\uparrow}^* h_{ij\downarrow} c_{j\uparrow}^\dagger c_{i\uparrow} c_{i\downarrow}^\dagger c_{j\downarrow} \rangle + \langle h_{ij\uparrow}^* h_{ij\downarrow}^* c_{j\uparrow}^\dagger c_{i\uparrow} c_{j\downarrow}^\dagger c_{i\downarrow} \rangle)$$

needs to be calculated.

The current for a non-interacting ring with an odd number of particles experiences a jump at the degeneracy point. Persistent current is defined as $J = -dE/d\Phi$, and the inability to differentiate the energy at the degeneracy point results in a discontinuity in the current. Since the energy is non-differentiable at that point the exact value of current corresponding to the degeneracy point is fairly uncertain. each degenerate state was given equal statistical weight, the zero-value for current agrees with the zero-temperature limit. However, a zero valued current implies a zero-valued slope on the energy function at the point, and the fluctuations obtained corresponding to $\mathcal{J} = 0$ arises from the $\langle J_\uparrow^2 \rangle$ and $\langle J_\uparrow J_\downarrow \rangle$ term. In the absence of current, current fluctuations remain finite.

The level crossings become avoided crossing with interactions the current becomes continuous as seen in the right column of Fig 5.1. The consequence of the interactions in the quantum current fluctuations is a broadening of the spike into a peak. Cross-componant current fluctuations play a crucial role in the size of the peak. Near the avoided crossings $\langle J_\uparrow J_\downarrow \rangle$ spikes with weak interactions. As interactions increase, the effect of $\langle J_\uparrow J_\downarrow \rangle$ diminishes. The current-current correlations $\langle J_{ij} J_{ij} \rangle$ have a different behavior being lesser in value for the weakest interactions, increasing in value as $U \approx \bar{t}$ and again decreasing in value for strong interactions.
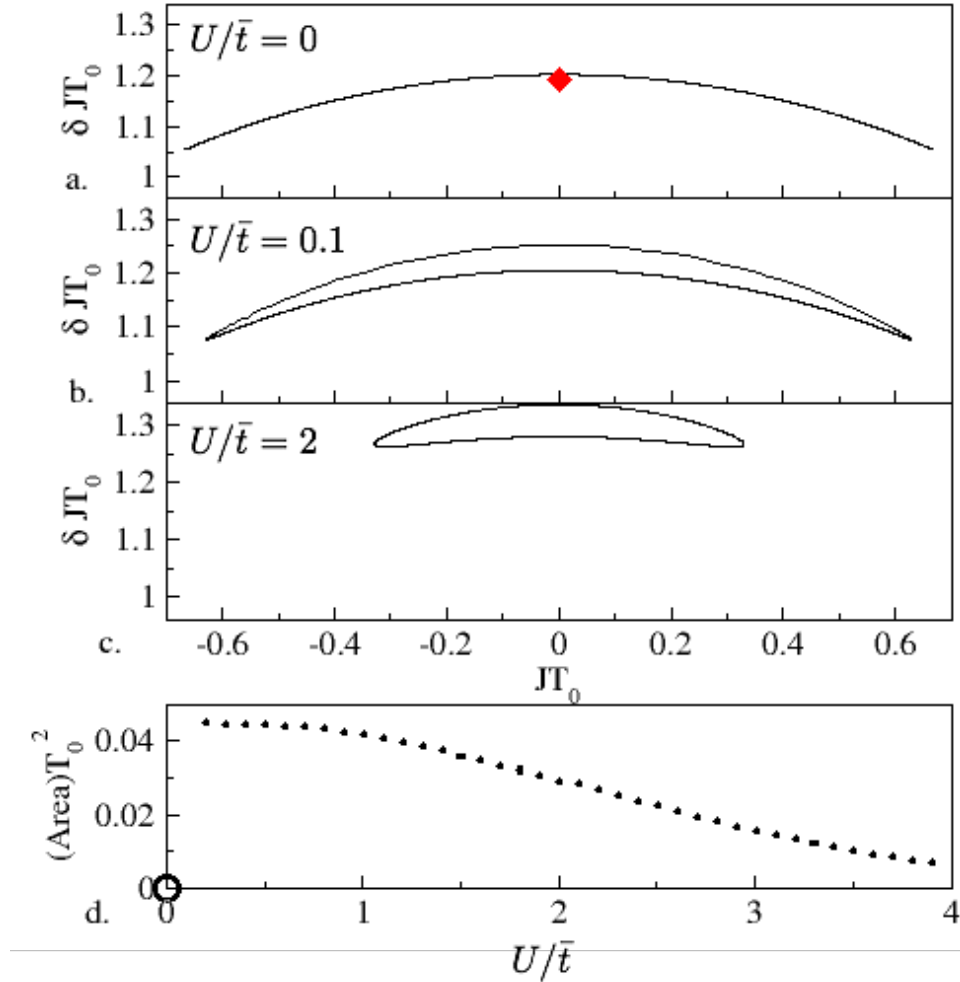
Figure 5.3: Ground-state Lissajous curve of δJ vs. J in the range $\pi/2 \leq \phi \leq 5\pi/6$ for (a) $U/\bar{t} = 0$, (b) $U/\bar{t} = 0.1$, (c) and $U/\bar{t} = 2$. The red rhombus in (a) indicate the value of the degenerate point. (d) Area of the loop over one period. The area is undefined at $U/\bar{t} = 0$ and is denoted by an open circle at zero. The area jumps to a non-zero value abruptly when the interaction becomes finite.

5.2 Lissajous Curves of Current and Current Fluctuation: Interaction Effects

Choosing a single value for current, how will the fluctuations for that value of current be affected by interactions? As the interactions are increased the fluctuations corresponding to the current value also increase. Adding interactions, a single value of current will appear twice in a single period. The left side of the current maximum corresponds to increasing current, and the right side corresponds to decreasing current. These two currents, though possessing the same value, have different fluctuations. The fluctuations of the left current are observably lower than the right. Thus, adding interactions causes multivalued fluctuations for a single value of current.

Since one value of current has two possible fluctuation values, it is worth investigating how the relationship will appear over an entire period. Plotting parametric equations result in Lissajous curves [1, 5, 53]. Fluctuations and current are both periodic functions in flux, parametric equations with equal frequency of oscillation. In a non-interacting system the fluctuations plotted against the current yields a single valued Lissajous curve Fig 5.3(a). Tracing this curve in one-dimensional space you find there is a discontinuity corresponding to the degeneracy. As one reaches the maximum or minimum value of current they would not be able to trace the path back to zero current, and a jump must occur. Perturbing the particles with interactions, Lissajous curves become multivalued and a path can be traced from one point back to itself without any discontinuities Fig 5.3(b-c).

There is a topological distinction between the non-interacting and interacting Lissajous curves. In general topology, the topology depends on the number of open sets and neighborhoods [81, 102]. A set is continuous if all subsets possess a neighborhood within that set, no matter how small the subset becomes. It is more simple to analyze the interacting Lissajous curves primarily. If a single point was removed from the curve, it would become a continuous arc possessing a single open set, and all points within this set, excluding the boundaries, have neighbors. The interacting Lissajous curve is a

continuous set. This system with a single set falls into a distinct topological class and is homeomorphic with all other single set curves. In contrast the non-interacting case has two open sets. The first set is on the interval $\pi/2 < \phi < 5\pi/6$, and all points within this set have neighbors. The second set consists of a single point $\phi = n\pi/6$ with n being an odd integer, and this point has no neighbors, particularly within the first open set. The non-interacting curve can only be connected by the union of the two sets, and is therefore in a disconnected topological space. Adding any interaction changes the topology of the Lissajous curves by connecting the two open sets.

All of the Lissajous curves with interactions are homeomorphic, yet the curve area is affected by the interaction strength. In the limit as $U \to 0$ the area approaches a constant value, signifying the addition of any interaction will make the Lissajous curve continuous. We have tested $U/\bar{t} = 0.01$ observing a curve agreeing with this conclusion. Increasing interactions broadens the loop, but the maximum and minimum value of current begins to decrease with increasing interactions. As repulsive interactions are increased the half-filled ring is Mott insulating, resulting in decreased particle conductivity due to particle localization. The Mott insulating phase causes the area of the loops to decrease with increased interactions Fig 5.3(d).

5.3 Effects from Next-Nearest-Neighbor Tunneling on Lissajous Curves

To further test the robustness of the Lissajous curve as a general phenomenological effect of mesoscopic systems, we consider a more complicated lattice structure by adding a next-nearest-neighbor tunneling term. Total flux from a magnetic field is defined as

$$\Phi = \int_S B \cdot dS = BS \tag{5.8}$$
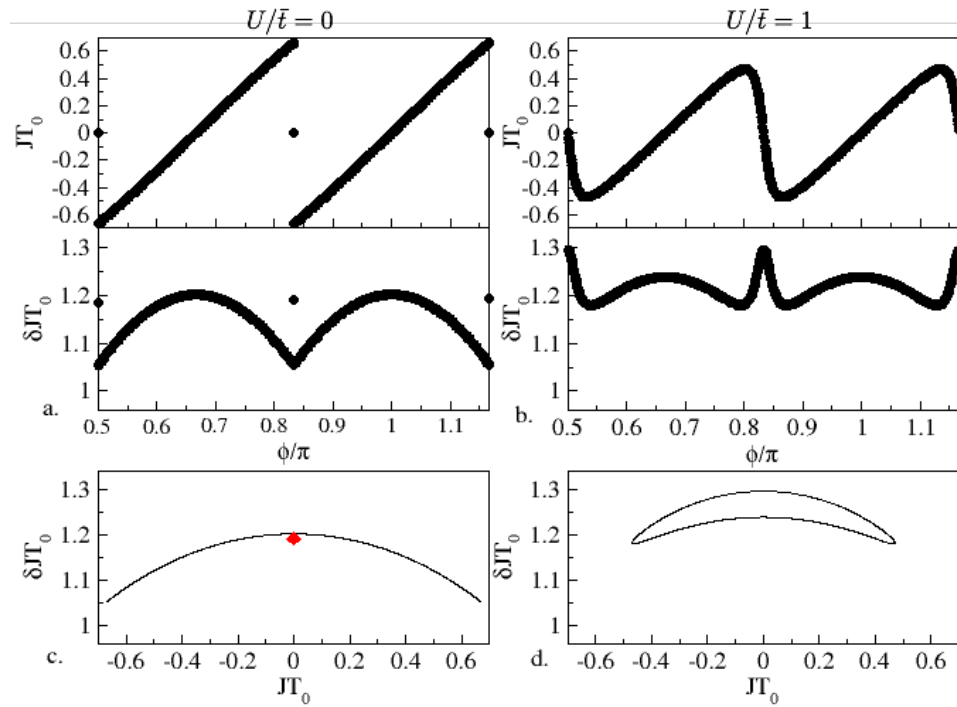
Figure 5.4: Current and corresponding quantum current fluctuations for a) $U/\bar{t} = 0$ and b) $U/\bar{t} = 1$ with next-nearest neighbor hopping $\bar{t}' = \bar{t}/5$. Current fluctuations as a function of current plotted from $\pi/2 \leq \phi \leq 5\pi/6$ for c) $U/\bar{t} = 0$ and d) $U/\bar{t} = 1$.

where B is the magnetic field perpendicular to the ring plane. Applying Stoke's theorem

$$\int_S B \cdot dS = \int_S (\nabla \times A) \cdot dS \oint A \cdot dL \qquad (5.9)$$

the flux can be determined from integrating the magnetic vector potential around a closed loop

$$\Phi = \oint A \cdot dL = AL. \qquad (5.10)$$

Light-induced vector potentials, and in turn flux, are defined along the direction of the wave vector [95]. The Peierls phase ϕ can be calculated from the magnetic flux as $\phi = \Phi/N$ where N is the number of links enclosing the flux. An area $S = 3\sqrt{3}l^2/4$ is enclosed by the next-nearest-neighbor links with a lattice constant $l = 1$. The flux on each link can be found by dividing the total flux by the number of links $\phi = \Phi/3 = \sqrt{3}l^2 B/4$. To find a relation between the flux on the nearest-neighbor links we calculate the relation to the magnetic field in the same way with $S = 3\sqrt{3}l^2/2$ and $\phi = \Phi/6 = \sqrt{3}l^2 B/4$. In cold atoms and materials, the next-nearest neighbor hopping strength is small compare to the nearest-neighbor hopping. The flux generated by the perpendicular magnetic field is equivalent on each of the links, and the off diagonal matrix element $h_{i,i+2} = \bar{t}' e^{i\phi}$ for next-nearest-neighbor links. To model a realistic system we consider the strength of nearest-neighbor hopping to be stronger than next-nearest-neighbor hopping $\bar{t} > \bar{t}'$.

Contributions to the Hamiltonian from next-nearest-neighbor hopping with hopping strength $\bar{t}'$ are considered to test the robustness of the Lissajous curve. In material and ultracold atomic system the effect of the next-nearest-neighbor hopping is minimal, so we tested cases where $\bar{t} > \bar{t}'$. Weak higher order hopping, $\bar{t}' = \bar{t}/5$, does not affect the overall results even with interactions since the level crossing are not present Fig 5.4. The resulting Lissajous curves of δJ vs. J still exhibit the same structures as the case without the NNN hopping.

Adding a stronger higher order hopping term, $\bar{t}' = \bar{t}/2$ changes the energy spectrum and energy periodicity. A level crossing is introduced in the energy with weak interactions arising as a discontinuity in the current and current fluctuations and lifts with
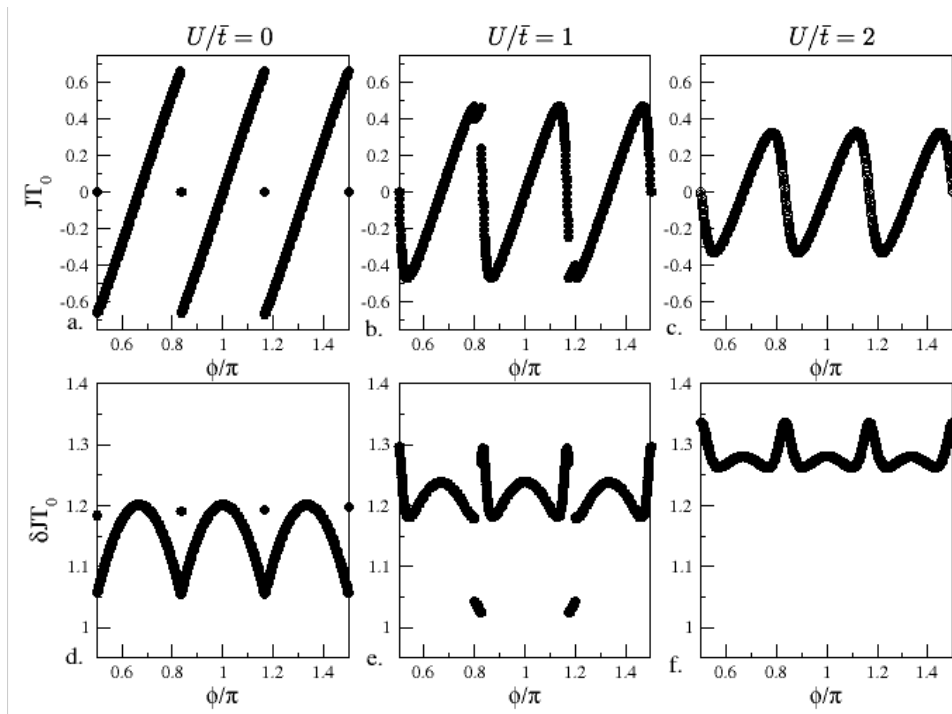
Figure 5.5: (a-c) Current and (d-f) corresponding quantum current fluctuations for $U/\bar{t} = 0$, $U/\bar{t} = 1$, and $U/\bar{t} = 2$ with next-nearest neighbor hopping $\bar{t}' = \bar{t}/2$.
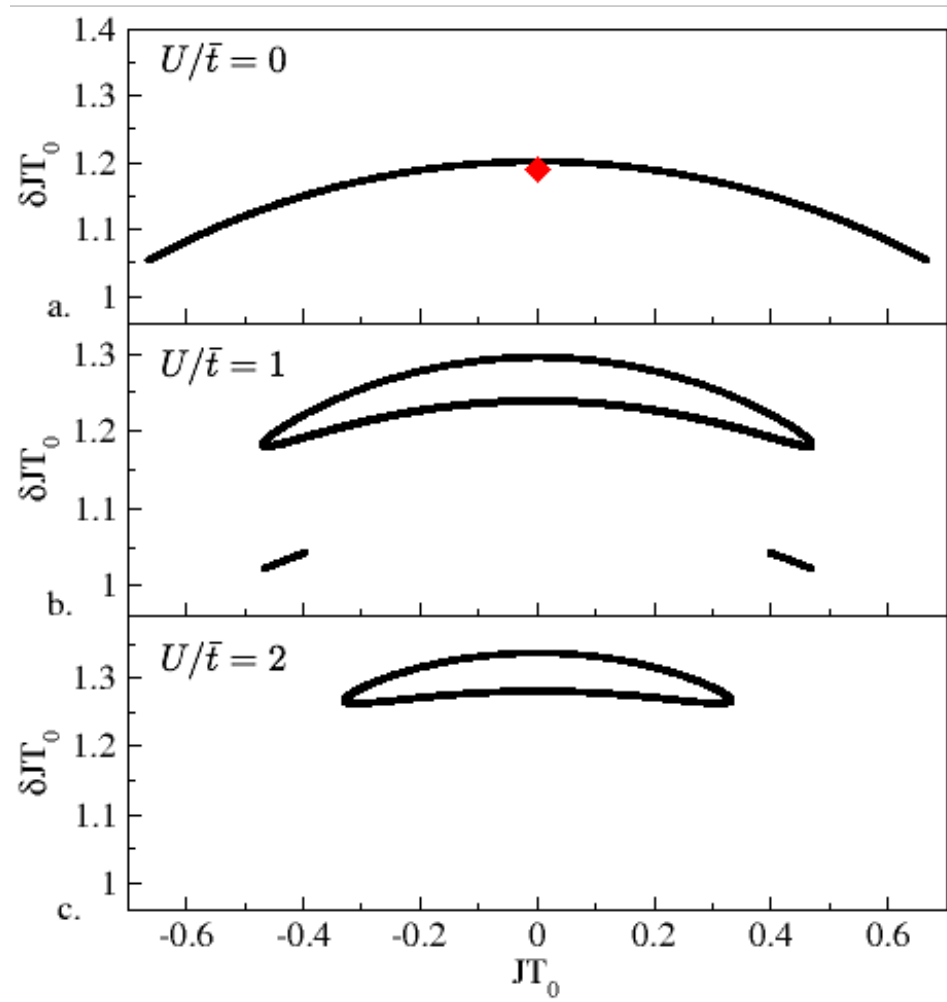
Figure 5.6: Current fluctuations as a function of current in a ring with next-nearest-neighbor hopping $\bar{t}' = \bar{t}/2$ plotted from $\pi/2 \leq \phi \leq 3\pi/2$ for a) $U/\bar{t} = 0$, b) $U/\bar{t} = 1$, c) and $U/\bar{t} = 2$.

strong interactions Fig 5.5. Levels crossing induced by interactions have been calculated using the Bethe Ansatz solution for persistent current in a one dimensional Hubbard model for strong interactions [149, 140], and have also been seen when considering higher-order hopping terms. Appearance of interaction induced levels crossings, in violation of the non-crossing rule, results from non-trivial symmetries and underlying conservation laws. We refer the reader to Refs [66, 6] for a detailed mathematical discussion. The Lissajous curves break at the level crossing with symmetry in the periodicity of flux Fig 5.6. If the period in flux is restricted to $5\pi/6 \le \phi \le 7\pi/6$ there are no degeneracies and the Lissajous curve without breaks can be observed.

5.4 Comment on Multi-Valueness in Open Quantum Systems

Research done on open quantum system was conducted by our collaborator Dr. Chen-Yen Lai. To demonstrate the Lissajous curves are a global property of transport in mesoscopic system, I am including data calculated by our collaborator with brief discussion on the results.

A one-dimensional lattice consisting of three sites is coupled to quantum reservoirs at the boundary sites with coupling strength $\gamma_L = \gamma_R = \gamma$ Fig 5.7(a). The left reservoir provides particles to the system and the right depletes them. Dynamics of a system coupled to the environment can be described using the Lindblad master equation

$$
\begin{aligned}
\frac{d}{dT}\rho &= i\,[\rho, \mathcal{H}_{\mathrm{S}}] + \gamma_L \sum_\sigma \left(c_{1\sigma}^\dagger \rho c_{1\sigma} - \frac{1}{2}\{c_{1\sigma}c_{1\sigma}^\dagger, \rho\} \right) \\
&\quad + \gamma_R \sum_\sigma \left(c_{L\sigma}\rho c_{L\sigma}^\dagger - \frac{1}{2}\{c_{L\sigma}^\dagger c_{L\sigma}, \rho\} \right),
\end{aligned}
\tag{5.11}
$$

and the density matrix is time-evolved. After the time-evolved density matrix is obtained

the current and fluctuations can be calculated as

$$\langle \hat{O} \rangle = \text{Tr}(\rho \hat{O}) = \sum_{mn} \langle m | \hat{O} | n \rangle \rho_{nm}, \tag{5.12}$$

where Tr denotes the trace and $\{|m\rangle\}$ is the set of the Fock-space basis kets from all possible particle-number sectors. The current can be tuned by adjusting the ratio $\gamma/\bar{t}$. Unlike the closed system, where the current is periodic in flux, the open system is not periodic and is driven by the two reservoirs. As the coupling strength is tuned from small value to large value the current exhibits a dome shaped, making it possible to have the same current in both small and large γ limit Fig 5.7(b). Currents in the small and large gamma limits though possessing the same value have different current fluctuation. This is similar to the closed system where multi-valueness of current fluctuation emerges with interactions.

Plotting the current vs. current fluctuations a closed form loop is seen with the addition of interactions Fig 5.7(d). Since the open system is not periodic, these loops are not Lissajous curves. If the system is noninteracting, there is a one-to-one correspondence between the current and fluctuations. Adding interactions fluctuations become multivalued for the same current in a different coupling regime. This means the loops only open up with the addition of interactions, suggesting the loops can serve as an order parameter distinguishing between non-interacting and interacting systems.

There are differences between the closed an open systems. In the closed systems the multi-valueness was demonstrated near a degeneracy point, but there are no degeneracies in the open system. The open system loop possess a more complicated structure than the closed system, and with strong interactions possess multiple nodes on the curves. The dependence of loops area on interaction is also different. As you increases in the closed system the area vanishes, but in the open system the area decreases gradually.

5.5   Experimental Realization Using Ultracold Atoms

The phenomena discussed here may be measured in experiments using ultracold atoms in engineered optical potentials. For example, the benzene-like lattice may be realized by using atom-by-atom assembly with optical tweezers [13, 47, 121] or painting potentials [67]. Open systems with a few lattice sites coupled to two reservoirs have recently been realized by projecting a lattice using holographic beams onto a conductive quantum wire coupled to atom reservoirs [86]. The magnetic field may be simulated by artificial gauge fields from light-atom interactions, and the Peierls phase has been demonstrated [75, 94, 56]. Importantly, the quantum coherence in ultracold atoms is robust because the system is virtually decoupled from the outside environment. Direct measurements of the current may be achieved by utilizing auxiliary light-atom coupling [84], and the current fluctuation may be obtained by evaluating the variance of the current from an ensemble.

Including finite-temperature effects will be a great challenge: Introducing temperature in a closed system requires the micro-canonical ensemble formalism via the concept of entropy [128]. In atom-by atom assembly the ability to laser-cool individual atoms prior to tunneling experiments accounts for entropy increase during geometrical setup [80, 121]. It is known the persistent current in the continuum decreases with temperature [4, 104], so it is expected the phenomena discussed here will also wane as temperature increases.

5.6   Conclusion

Quantum current correlations of persistent current in a mesoscopic ring lattice have interesting features arising from the current-current and cross-current correlations when interactions are present. The stark difference between non-interacting current and fluctuations from the interacting picture is the presence of a degeneracy and non-differentiable point in the energy leading to a discontinuity in the current. The

addition of interactions lifts this degeneracy point and the ground state energy is differentiable for any value of flux. Consequently, correlations contribute to a broadening of a peak in fluctuations in the vicinity of the maximum energy as the degeneracy is lifted in the spectrum.

The periodicity of the energy give parametric equations between the current and the fluctuations. Lissajous curves are generated when these parametric equations are plotted and the frequency of both the current and fluctuations are the same. To parametric equations with the same frequencies gives curves that are spherical/ellipsoidal. There is a distinct topological difference between the non-interacting and interacting Lissajous curves. The non-interacting Lissajous curve has two disconnected sets, and the interacting Lissajous curve has one set. Non-interacting and interacting Lissajous curves are not holomorphic of each other which means there is a topological distinction between both. Adding an external perturbation, like contact interactions, connects the two subsets and all Lissajous curves with interactions are holomorphic of each other.

Particle tunneling between next-nearest neighbors is likely to occur in a realistic lattice with the tunneling being less in magnitude than nearest-neighbor. The addition of long-range tunneling parameters is considered, and it is found with weak next-nearest neighbor tunneling the qualitative behavior of the results is unaffected. With stronger long range tunneling level crossing are induced by interactions. These level crossing cause discontinuities in the current, fluctuations and the Lissajous curves, and they are periodic in flux.
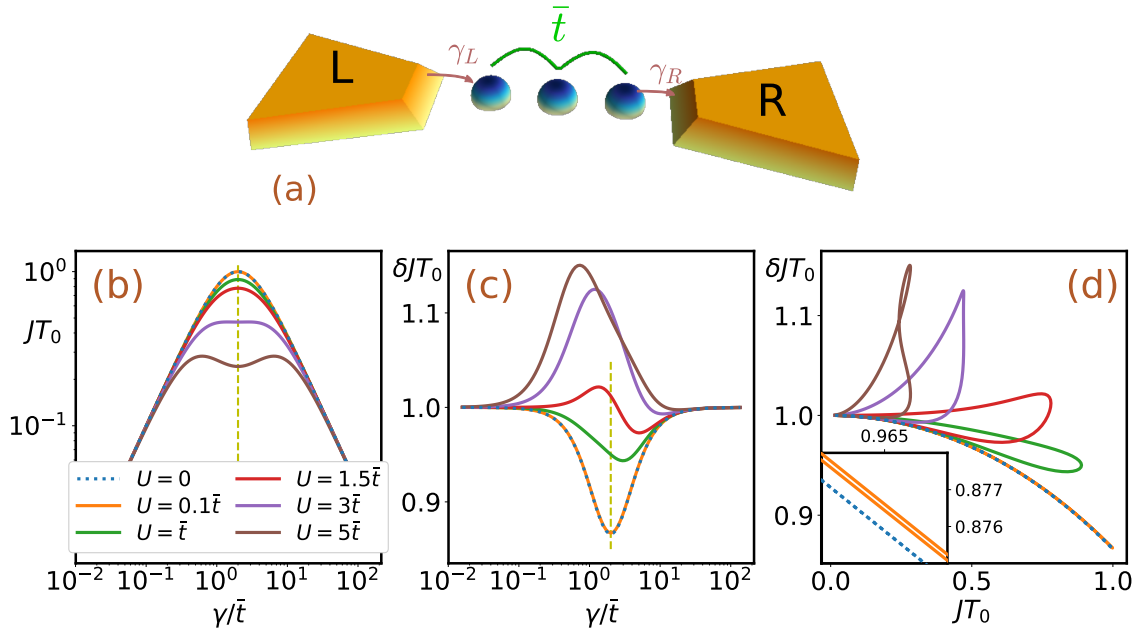
Figure 5.7: (a) Schematic plot of a three-site lattice connected to a source (left) and drain (right). The hopping coefficient between the lattice sites is $\bar{t}$, the system-reservoir couplings are $\gamma_{L,R}$, and the onsite interaction has the coupling constant U. The open system is described by the quantum master equation (5.11). (b) Currents and (c) current fluctuations versus $\gamma = \gamma_L = \gamma_R$ for selected values of $U/\bar{t}$ in the three-site open system. When $U = 0$, the current and current fluctuation are symmetric about the yellow dashed line ($\gamma = 2\bar{t}$). When $U/\bar{t} > 0$, only the currents remain symmetric while the current fluctuations become asymmetric. (d) Current fluctuation versus current. When $U = 0$ (dashed line), there is a one-to-one correspondence between the current and current fluctuation. In contrast, a closed loop and multi-valueness are observable for all $U > 0$. The inset shows a detailed comparison of δj vs. j for $U/\bar{t} = 0$ and $U/\bar{t} = 0.1$.

Chapter 6

Observing Topological Boundary Effects in Cold Atoms

The following protocols for detecting edge states using cold atoms were published by the author in Ref [105] Copyright 2017 IOP Publishing. Below a more detailed description is provided on the research results.

6.1 Motivation

Emergent condensed matter phenomena arising from topological behavior has incited increasing attention. For instance, topological insulators can host edge states within an insulating energy gap and are characterized by topological invariants arising from their band structures [8, 131, 34, 119, 62]. The versatility of ultracold atoms for simulating many-body systems [31, 19] leads to realizations of important topological systems such as the Su-Schrieffer-Heeger (SSH) model [10], Harper-Hofstadter Hamiltonian [107, 2], and the elusive Haldane model [77]. Topological structures also support unique dynamical features realizable with cold atoms such as quantized charge transport [111, 96].

The SSH model has been constructed with an optical superlattice in a confining

potential to probe quantum phases [10]. It supports nontrivial band topology with sublattice symmetry and localized edge states when the system is uniform. Direct detection of edge states, however, has been hindered by the confining potential, which distorts the density profile and prevents a sharp boundary. There have been proposals for observing topological edge modes in 2D cold-atom systems [54]. Here, an alternate setup in 1D with well defined boundaries, where edge states can be generated and detected [65]. Rather than confining atoms in a harmonic trap, they can be confined in an optical ring lattice [108, 39]. The ring can be cut open with an off resonant laser sheet, resulting in a one dimensional lattice with open boundary conditions as illustrated in Figure 6.1(a). Experimental techniques to develop atom circuitry have provided creative means to engineer optical ring potentials with optical masking [39] or painted potentials [24, 67].

Confining atoms in a ring lattice cut by a laser sheet generates localized edge states in real space, but additional methods are needed to distinguish the occupied edge states from the background. As shown in Figure 6.1(b) and 6.1(c), the density profiles of a half-filled, open lattice are featureless for both noninteracting and interacting systems. This is because the edge states are usually buried in a pile of other states, so extra processes for extracting its structures are required. We present dynamical protocols resolving edge state detection with an injection method and a depletion method. A single fermion injected at the edge of an empty open lattice with nontrivial topology does not fully spread out as time evolves because most of its weight is kept by the localized state at the edge. A similar idea was behind recent experiments for bosons injected onto a boundary of a lattice constructed in momentum space [100], and our proposal is the real-space counterpart. Another way to probe the edge states is to dynamically remove atoms [29]. Removing atoms away from the edge over time depletes most of the states except the edge states localized at the boundary. We demonstrate feasible setups for both schemes.

Although the characterization of noninteracting topological systems is pretty complete [34], identifying and characterizing topological properties in interacting
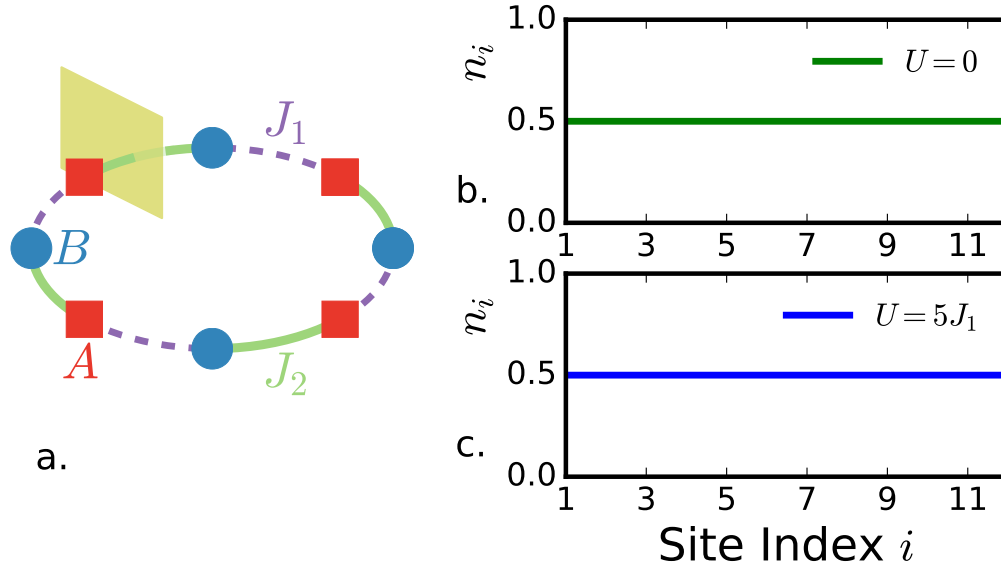
Figure 6.1: (a) Trapping set up with optical ring lattice cut with an off resonant laser sheet (yellow) to open boundaries. The lattice has unit cell with two sites A (red square) and B (blue circle). Density profile for a half-filled lattice with $L = 12$ sites, half filling, $J_1/J_2 = 0.5$, and interaction strength (b) $U/J_1 = 0$ and (c) $U/J_1 = 5$.

systems has remained a great challenge. Topological invariants, calculated from the single-particle wavefunction, are more difficult to evaluate for many-body states. While some invariants can be calculated by Green's functions in the thermodynamic limit [99, 141], cold-atom systems are usually of finite size and require more direct characterization. A half-filled SSH model with an even number of sites has particle-hole symmetry and is shown to remain topological in the presence of interactions [63, 60]. A global topological number may also be determined by adding a phase twist to the boundary and analyzing the phase change when interactions are present [60, 68, 59]. However, the structure of many-body topological edge states remains elusive.

Instead of mapping out the edge state in interacting systems, we propose analyzing selected correlation functions for revealing the dimerized structures in the SSH model

with interactions. Finite correlations will be shown to survive across a broken link after a boundary is created by inserting a laser sheet to cut open a ring lattice. The evolution of spin-spin correlations distinguishes between trivial and nontrivial topological configurations with and without interactions. Previous investigations revealed there are two types of insulators for the dimerized chain depending on whether interactions are present [92, 99, 8, 131]. The time evolved density-density correlations are found to differentiate between the noninteracting band insulating and interacting Mott insulating phases of the one-dimensional SSH Hubbard model.

6.2 Topological Properties of the One-Dimensional Su-Schrieffer-Heeger Model

The SSH model describes a one-dimensional (1D) dimerized lattice with alternating hopping strengths [8, 131]. The 1D chain hosts two sites (A and B) in each unit cell. The Hamiltonian of an N-site noninteracting system is

$$H = -\sum_{i=0}^{N} \left[J_1 c_{B,i}^\dagger c_{A,i} + J_2 c_{A,i+1}^\dagger c_{B,i} + h.c. \right]. \tag{6.1}$$

Here $c_i^\dagger(c_i)$ represents the creation (annihilation) operator on site i. The hopping coefficients alternate with J_1 and J_2 as shown in Figure 6.1(a). Depending on the boundary condition, the hopping between site N and site 1 is present (for periodic boundary condition) or absent (for open boundary condition). The unit of time $t_0 = \hbar/J_1$ is set by the intracell hopping coefficient and $\hbar = 1$. We first consider a periodic system and by taking a Fourier transform of the creation (annhilation) operators, $c_{i,A} = \sum_k a_k e^{ik \cdot x_i}$ and $c_{i,B} = \sum_k b_k e^{ik \cdot (x_i + a/2)}$, the Hamiltonian in momentum space is

$$H(k) \qquad = \qquad \sum_k \begin{pmatrix} a_k^\dagger & b_k^\dagger \end{pmatrix} h(k) \begin{pmatrix} a_k \\ b_k \end{pmatrix} \qquad \text{with}$$

$$h(k) = \begin{pmatrix} 0 & J_1 e^{ika/2} + J_2 e^{-ika/2} \\ J_1 e^{-ika/2} + J_2 e^{ika/2} & 0 \end{pmatrix}.$$ The lattice constant a serves as

the length unit and the momentum summation is over the first Brillouin zone. The matrix

$h(k)$ can be diagonalized as $\begin{pmatrix} 0 & \epsilon(k) e^{i\theta} \\ \epsilon(k) e^{-i\theta} & 0 \end{pmatrix}$. The energy dispersion is given by

$\epsilon(k) = \pm\sqrt{J_1^2 + J_2^2 + 2J_1 J_2 \cos(k)}$. A gap opens between the upper and lower bands in

the bulk when $J_1 \neq J_2$.

Topological insulators can be classified according to their symmetries [34, 131, 119]. The SSH model has chiral (sublattice) symmetry with an associated topological invariant called the winding number ν defined for systems with periodic boundary condition. ν takes values of ± 1 depending on whether $J_1/J_2 > 0$ or $J_1/J_2 < 0$, revealing the parameters of the Hamiltonian wrap around a point counterclockwise (clockwise) in the parameter space. For systems with open boundary condition, zero-energy edge states localized at the boundary can emerge depending on the configuration. The bulk-boundary correspondence [8, 119, 62] states that the number of edge modes is determined by the bulk topological invariant.

Here we propose measuring consequences of band topology by probing the topological edge states. An open boundary introduces an interface between the topological SSH chain and the topologically trivial vacuum, so edge modes can emerge if the configuration is suitable. Location of the edge states on sublattice A (sublattice B) depends on the condition $J_1/J_2 < 1$ ($J_1/J_2 > 1$) and sign of the associated winding number. For instance, in a long chain with one end ending with a J_1 link and $J_1/J_2 < 1$, the probability amplitude of an edge state $|\phi\rangle$ has the form

$$\langle i|\phi\rangle = \mathcal{N}\left(1, 0, -\frac{J_1}{J_2}, 0, \left(-\frac{J_1}{J_2}\right)^2, 0, \left(-\frac{J_1}{J_2}\right)^3, ...\right) \tag{6.2}$$

and it localizes on sublattice A at the boundary. $\mathcal{N} = [1 - (\frac{J_1}{J_2})^2]^{1/2}$ is a normalization factor. Similarly, an end with a J_2 link with $J_1/J_2 > 1$ can support an edge state with similar structures on the B sublattice (but with J_2/J_1 in the power series). Therefore, for a chain with odd number of sites, one edge state is guaranteed and its location depends on the

ratio of J_1/J_2. For a chain with even number of sites, there can be zero or two edge states. For instance, an open chain ending with J_1 links on both sides and $J_1/J_2 < 1$ supports an edge state on both sublattices, and the two modes hybridize to give one symmetric and one anti-symmetric edge mode. On the contrary, the same chain with $J_1/J_2 > 1$ yields no zero-energy edge states. For a ring lattice, an even number of sites is a natural setting before a laser sheet cuts it open, so we will refer to the case with two edge states after it is cut open as the topologically nontrivial and the one with no edge state as the topologically trivial. It is possible, however, to generate a ring with an odd number of lattices [87, 83].

In cold-atom experiments, usually accompanying the alternating hopping in superlattices is the addition of alternating onsite energies, which adds a term $\sum_j (-1)^j \Delta c_i^\dagger c_i$ to the Hamiltonian [10]. The edge-state configuration is still maintained in the presence of alternating onsite energies as one can verify directly, although the edge-state energy is shifted by Δ. For quantized charge pumping of particles [131, 111, 96], this addition of alternating onsite energies is essential because the edge states will fuse into the bulk [15] as the crossing $J_1 = J_2$ happens when they are tuned dynamically. Furthermore, Δ can be tuned to zero [10], so for simplicity we do not include the alternating onsite energy in our discussion.

6.3 Experimental Detection Challenges of Ultracold Atoms and Proposed Solutions

Alternating onsite energies do not destroy the edge states, but a confining harmonic trap can be detrimental to them. A harmonic confining trap, $V(r) \propto r^\gamma$ with $\gamma = 2$, keeps atoms in the optical setup, but it has been shown that if $\gamma < 10$, the energy gap of a dimerized lattice closes due to distortion of the density profile and the edge states fuse into the bulk of the lattice [10]. When γ is large the potential takes the form of a box potential with well defined boundary. Three dimensional box potentials created by intersecting a

hollow tube beam with two sheet beams provide sharp boundaries [50], but adding lattice potential on top of the box potential can be more challenging.

6.4 Dynamical Signatures of Edge States in Topological Noninteracting Systems

We propose a method for confining the atoms in a ring lattice cut with a laser sheet to open the boundary Figure 6.1(a). The appearance of edge states depends on where the link is cut. If $J_1/J_2 < 1$ and the laser sheet cuts a strong link, J_2, two edge states emerge along with further correlation effects. The laser sheet may introduce an energy shift on nearby sites. Assuming a shift of ϵ on the boundary site, the edge mode wavefunction (6.2) starts acquiring values $\epsilon/J_1, \epsilon/J_1(-J_2/J_1), \cdots$ on those sites originally with zero amplitude. The edge mode survives in a chain with length less than $(1/2)[\ln(\epsilon/J_1)/\ln(J_1/J_2)]$. Making the laser sheet sharper to reduce the shift of onsite energy near the boundary will help the edge mode to be more prominent. Interestingly, when $\epsilon = J_1$, the edge mode is completely destroyed, a result consistent with a direct mathematical evaluation [82]. We will assume the collateral energy shift is negligible.

While edge-state contribution can be measured from transport in electronic systems [62, 119], there is a need to develop methods to measure the edge states in cold-atom systems [31]. Bosonic atoms revealed characteristic edge states in momentum space using a single site injection method [100]. Here we found that real-space single site injection also serves as a suitable method to probe edge states. The idea is to have an empty lattice and inject a single atom onto the site at the open boundary, then the particle propagates in time. The time-evolved density profile can be monitored by evolving the correlation matrix $\langle c_i^\dagger c_j \rangle$ according to the equation of motion

$$-i\frac{d\langle c_i^\dagger c_j \rangle}{dt} = \langle [c_i^\dagger c_j, H] \rangle. \tag{6.3}$$
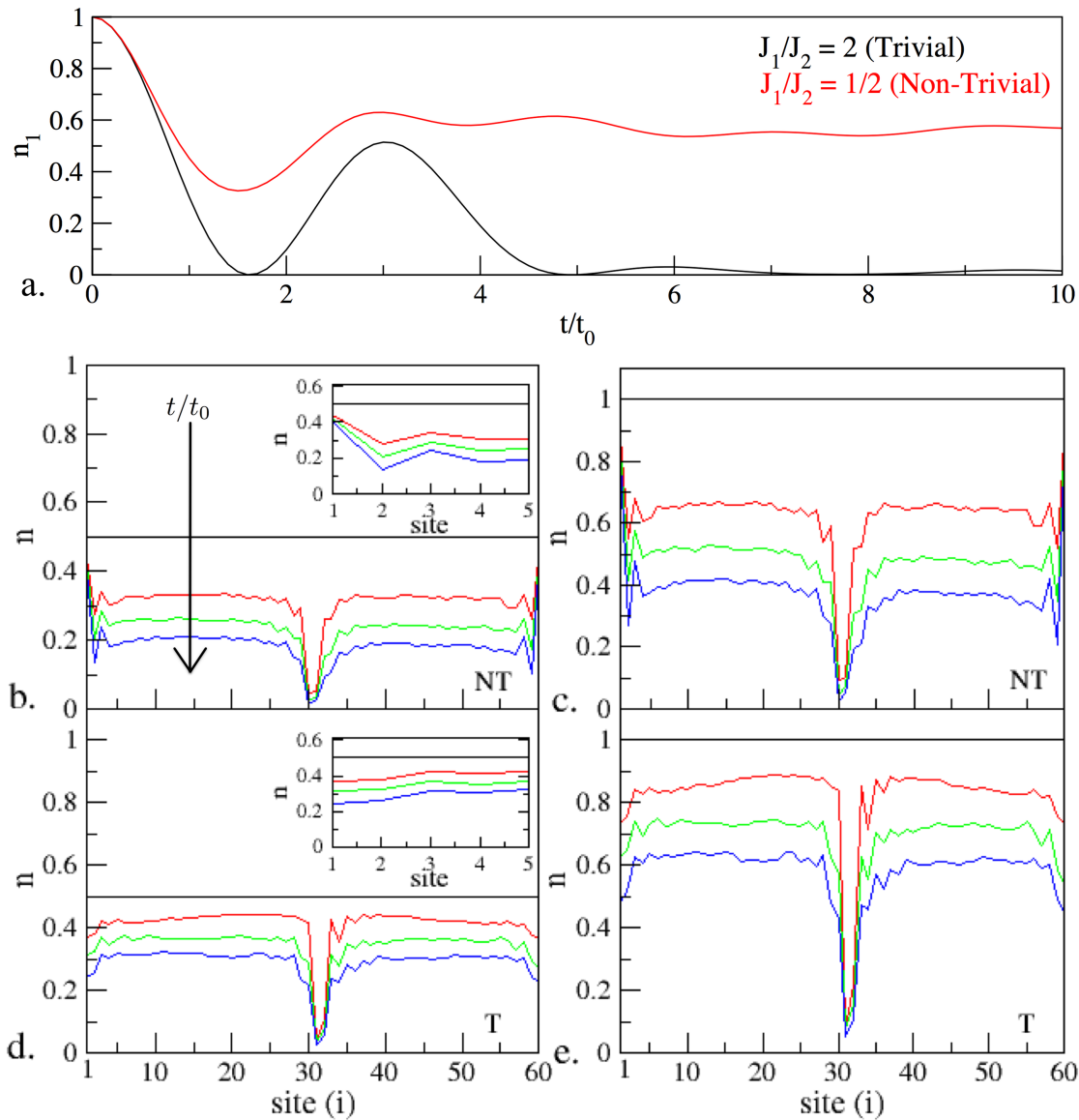
Figure 6.2: (a) Density of the left-most site for a 60-site lattice with one fermion initially place on left boundary. The topologically nontrivial case (red, $J_1/J_2 = 0.5$) has an edge mode on the edge retaining the injected particle while the injected fermion propagates away in the topologically trivial case (black, $J_1/J_2 = 2$). (b) - (e) Evolution of the density profiles of a $L = 60$ lattice sites with a depletion beam removing particles near the center of the system ($i = 31$). The density profiles at selected times (from top to bottom) $t/t_0 = 0, 50, 100, 150$ are shown. The elements $\langle c_{31}^\dagger c_i \rangle$ and $\langle c_i^\dagger c_{31} \rangle$ are wiped out every $t_0/2$. (b) and (c): The topologically nontrivial configuration ($J_1/J_2 = 0.5$, labeled "NT") displays prominent localized edge-state structures with higher density at the two open ends as the overall density is depleted. (d) and (e): No localized structures emerge in the topologically trivial configuration ($J_1/J_2 = 2$, labeled "T"). The insets of (b) and (d) show the density profiles of the first five sites at the boundary.

The initial condition is $\langle c_1^\dagger c_1 \rangle (t\!=\!0)\!=\!1$ and all other elements are zero, where the first site is at the open boundary. The density on site i is $\langle c_i^\dagger c_i \rangle$ and can be extracted from the time-evolved correlation matrix. A fourth-order Runge-Kutta algorithm is used to numerically evaluate the time-evolution.

A single particle injected onto an end site not supporting an edge state propagates away, while a significant fraction of the wavefunction will be retained if there is an edge mode at the boundary. This can be understood by Eq. (6.2) because the edge mode has weight $\mathcal{N}^2 = 1 - (J_1/J_2)^2$ at the boundary site, so the injected fermion will fill the edge mode significantly. Figure 6.2(a) contrasts the remaining density on the injection site with and without an edge mode. For the topologically nontrivial case, the edge mode retains ≈ 0.6 of the weight, which is close to $\mathcal{N}^4 + (1 - \mathcal{N}^2)^2 = 0.63$ estimated from a direct calculation. In contrast, the density practically vanishes as time evolves in the topologically trivial case. The remaining density thus distinguishes the trivial and nontrivial topological configurations, providing measurable evidence of edge states in real space.

The method of depletion provides another measurable evidence of topological edge states, and a similar depletion method has been considered for an optical kagome lattice [29]. By depleting the atoms away from the boundary over time, density of localized particles on the edge become prominent because their weights are small in the bulk. To deplete atoms, a focused laser can eject atoms from the optical trap [23]. Alternatively, an electronic beam has been used to deplete bosons since, excited through collisions, atoms can escape the trap [12]. We consider a uniformly filled lattice with open boundary condition as the initial state and approximate the depletion of atoms on site m by removing all correlations $\langle c_m^\dagger c_i \rangle = \langle c_i^\dagger c_m \rangle = 0$ associated with the atom. Interestingly, depleting with a finite removal rate is necessary, or else the depleting beam will act as a barrier preventing particle transport. Here we use a removal rate of depleting the selected correlations every $t_0/2$, and the qualitative conclusion remains for other reasonable removal rates. Examining the density profile of the topologically nontrivial

configuration, occupancy at the boundary is prominent as the value predicted by $\mathcal{N}^2$ is approached Figure 6.2(b,c). The edge states are observable when the initial filling is above half-filling. The topologically trivial configuration, in contrast, exhibits diminishing edge density as shown in Figure 6.2(d,e). The comparison shows edge states are revealed in noninteracting systems with atom depletion away from the edge.

6.5   Dynamical Signatures of Dimerization in Interacting Systems

Determining topological classification of systems with interactions is difficult. A periodic, dimerized lattice has nontrivial topological features in the presence of onsite interactions when particle-hole symmetry is respected [63]. Therefore, distinguishing topological features of a dimerized lattice with interactions experimentally using cold atoms is desired. Rather than probing global topological number, specific short range correlation functions will indicate nontrivial topology and dimerization structures. Correlation function dynamics is observable as the boundary is changed from periodic to open. Dynamics of some correlations have been evaluated for both trivial and nontrivial topological configurations of the noninteracting SSH model and the Kitaev chain [65]. Importantly, correlations of density or spin can be experimentally measured using phase-contrast imaging which can distinguish between populations of each component [132, 51, 91].

To model the contact interaction of atoms, we use the two-component Hubbard model with onsite repulsion described by $H_U = U \sum_i n_{i\uparrow} n_{i\downarrow}$. Here U is the coupling constant and $n_{i\uparrow}$ ($n_{i\downarrow}$) is the number operator for spin up (down) fermions. The hopping Hamiltonian, Eq. (6.1), is generalized to two components as well. Here the two components $\sigma = \uparrow, \downarrow$ may be two different internal states of the same atomic species. The one-dimensional Fermi Hubbard model can be solved analytically using the

Figure 6.3: Spin-spin correlations of fermions across a suddenly broken link of a dimerized, $L = 12$ site lattice with $J_1/J_2 = 0.5$. The topologically nontrivial configuration (top row) supports two edge modes in the noninteracting case with open boundary condition, and the cut is across a strong link J_2 for $U/J_1 = 0, 1, 5$ (a,c,e). The correlations remain finite after the boundary transformation. The topologically trivial configuration (bottom row) has a cut at a weak link J_1 for increasing interactions $U/J_1 = 0, 1, 5$ (b,d,f). The correlations fluctuates around zero. The triangular (square) symbols show the time-independent correlation of a static configuration with periodic (open) boundary condition for the corresponding case. In all cases the system is half-filled.

Bethe-Ansatz revealing, in the thermodynamic limit, a half filled uniform lattice has a charge gap for any finite interaction [92]. As discussed previously, a dimerized lattice is a band insulator when $U = 0$ at half-filling or full-filling, and it is a topological Mott insulating phase at half-filling when $U > 0$ [99]. By choosing suitable correlation functions, it is possible to distinguish between the topologically nontrivial and trivial configurations in conjunction with band insulating and Mott insulating phases.

We use exact diagonalization (ED) to determine the ground state [93, 130] up to moderate system size and already observe prominent features in relatively small systems. If larger systems are being considered, density matrix renormalization group (DMRG) method may be used [146, 145, 127]. The results presented are from a lattice with $L\!=\!12$ sites, and the same behavior is already observable for systems as small as $L = 8$ sites. Dynamics of the system can be simulated efficiently by applying a Krylov-space approximation to the time evolution operator $U(t)\!=\!e^{-i\hat{H}dt/\hbar}$ to reduce the dimension of matrix operations [98]. The approximation is limited by the Hamiltonian's spectrum width, and we compared the results against the full, exact solution of small size systems to verify the accuracy. The time evolution of correlation functions across a selected link can then be monitored.

To identify which correlation function can clearly reveal the dimerization, we investigate the equal time spin-spin correlation between the sites across the broken link (connecting sites i and $i + 1$):

$$\chi_{ss}(t) = \langle n_{i+1,\sigma}(t)n_{i,\sigma}(t)\rangle - \langle n_{i+1,\sigma}(t)\rangle\langle n_{i,\sigma}(t)\rangle. \tag{6.4}$$

It probes the correlations between the same spin component across the selected link. If measured across a strong (weak) link with J_2 (J_1) and $J_1 < J_2$, the correlation is intracell (intercell). Figure 6.3 shows the correlation in static configurations with open or periodic boundary condition (marked by the symbols). For the intra-dimer correlation, $\chi_{ss}(t)$ remains finite for both the noninteracting ($U/J_1\!=\!0$) and interacting ($U/J_1\!>\!0$) cases. In contrast, the correlation decays to zero for the topologically trivial case. The finite

spin-spin correlation results from the spin singlet on the link $(|\uparrow\downarrow\rangle - |\downarrow\uparrow\rangle)$ preferred inside each dimer, but inter-dimer spin correlations should be weak because long-range spin order is forbidden in 1D [103] and there is no spin gap for a uniform chain in the exact solution [92]. Spin correlation within a dimer is dominated by the singlet behavior and prefers anti-parallel spins, while the spin correlation between adjacent dimers is practically random. Meaning, the spin-spin correlation function can distinguish whether an intercell or intracell link has been broken, working for both noninteracting and interacting cases.

The dynamics of correlation functions can be further explored by setting the lattice configuration initially half-filled and periodic, then changing the boundary condition by suddenly cutting and measuring correlation across a link. In isolated system like cold-atoms trapped in optical potentials, there is no external energy dissipation. As shown in Figure 6.3, the correlations oscillate around their average values, but the contrast between the finite correlation of the intracell case and the vanishing correlation of the intercell case persists in the time-evolution. The correlation can sometimes overshoot the equilibrium values in its time-evolution. Morevoer, the intracell correlation does not decay to zero and exhibits memory effects of its initial state. We mention that previous work has investigated long-range correlations in dimerized lattices by analyzing entanglement entropy [72], and the edges exhibit quantized Renyi entanglement entropy from an effective coupling of sublattices with finite size [142].

The spin-spin correlations, however, do not distinguish between the (noninteracting) band and (interacting) Mott insulating phases of the dimerized lattice, and we need another correlation function to accomplish this. Since Mott insulating phase suppresses onsite density fluctuations but the band insulating phase does not, one can differentiate the two phases by checking the onsite density fluctuation $\langle n_i^2 \rangle - \langle n_i \rangle^2$ [42]. We further consider the equal time density-density correlation function defined by

$$\chi_{dd}(t) = \langle n_{i+1}(t)n_i(t)\rangle - \langle n_{i+1}(t)\rangle\langle n_i(t)\rangle. \tag{6.5}$$
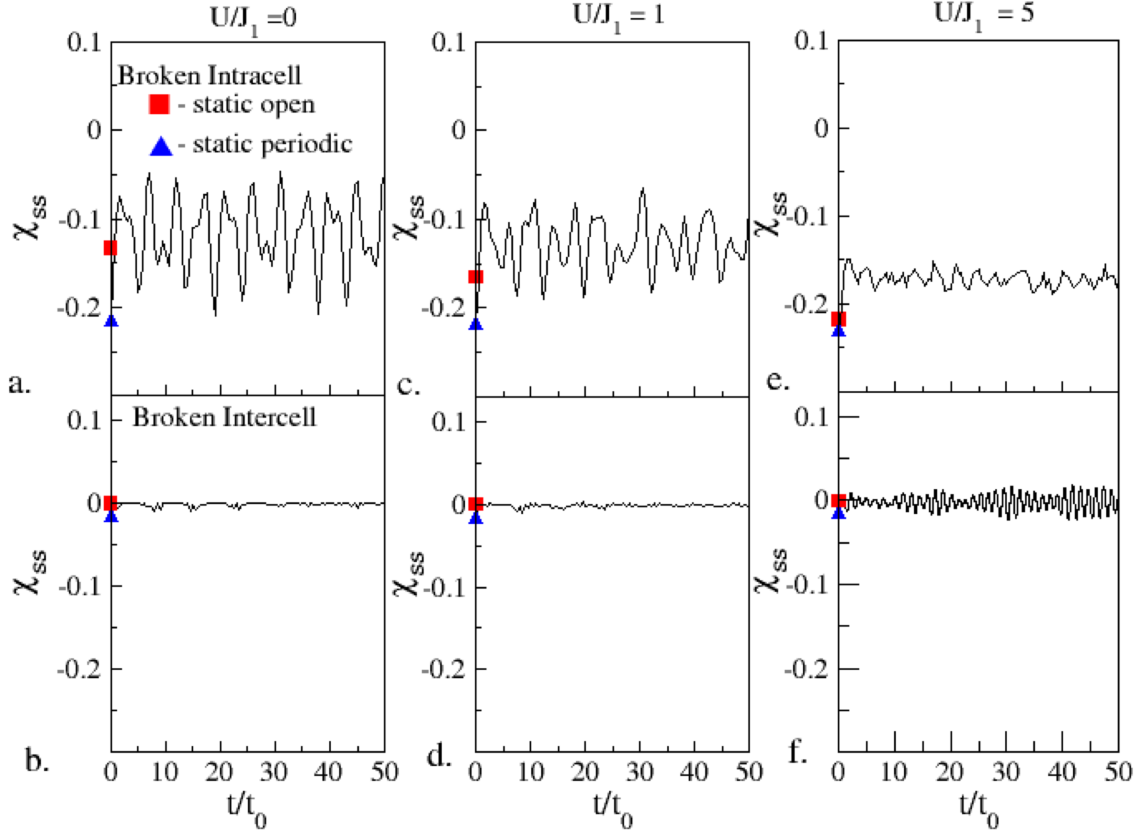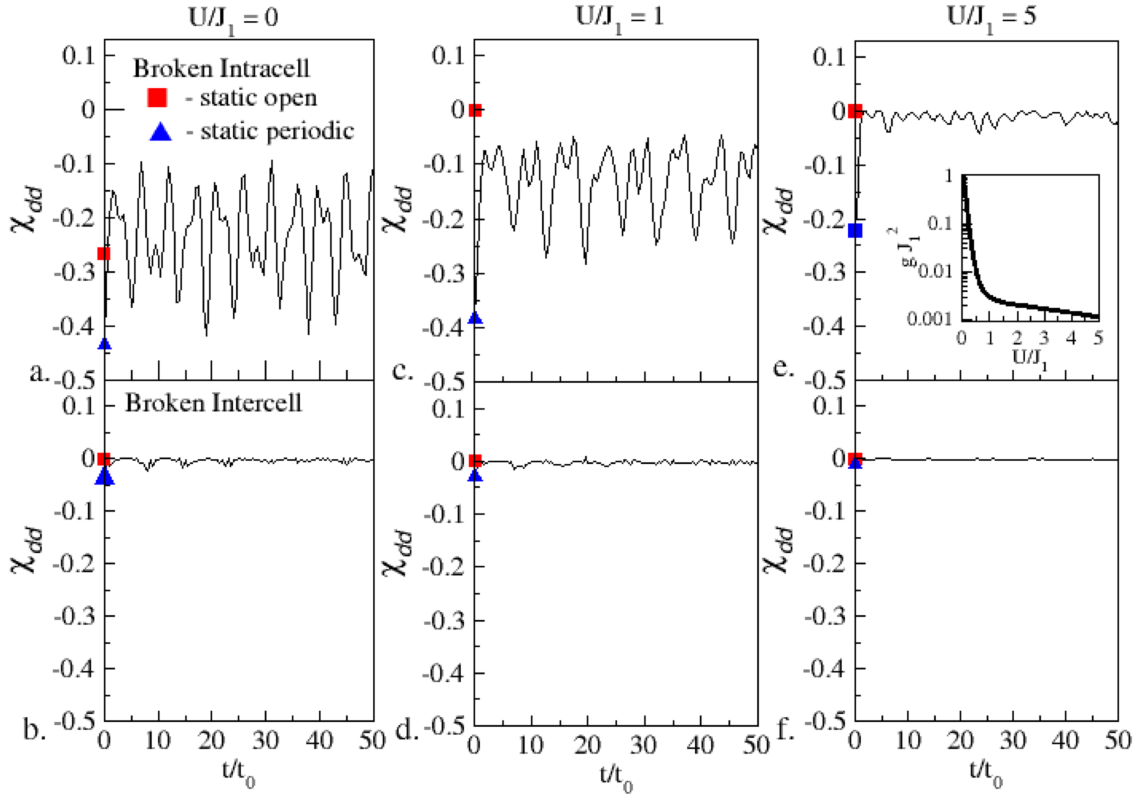
Figure 6.4: Density-density correlations of fermions across a suddenly broken link of a dimerized, $L = 12$ site lattice with $J_1/J_2 = 0.5$. The topologically non-trivial configuration (top row) has a cut across a strong link J_2 for $U/J_1 = 0, 1, 5$ (a, c, e). The noninteracting case exhibits finite density-density correlations after the boundary transformation, while the correlations of the interacting cases diminish due to the suppression of density fluctuations in the Mott insulating phase. The topologically trivial configuration (bottom row) for $U/J_1 = 0, 1, 5$ (b,d,f) is determined by cutting across a weak link J_1. The correlations all average around zero in this configuration. (Inset) Fidelity metric as a function of interaction strength U/J_1 shows a finite-width transition from the noninteracting band-insulating phase to the interacting Mott insulating phase. The correlations fluctuates around zero. The triangular (square) symbols show the time-independent correlation of a static configuration with periodic (open) boundary condition for the corresponding case. In all cases the system is half-filled.

Here $n_i = \sum_\sigma n_{i\sigma}$ is the particle number operator on site i. As shown in Figure 6.4, the static value of the density-density correlation always vanishes across an intercell link regardless of the boundary condition. For the static correlation across an intracell link in the open-boundary case, the correlation is finite in the noninteracting case and vanishes if the interaction is strong. Therefore, the correlation may distinguish the two types of insulating phases if measured across an intracell link.

The dynamics of the density-density correlation function reaches a similar conclusion when the boundary condition is transformed from periodic to open by suddenly cutting an intracell or intercell link. As shown in Figure 6.4(a, b), for noninteracting systems χ_{dd} remains finite across the broken intracell link. In contrast, the similar correlation for the strongly interacting case oscillates around zero. By comparing the eigenstates of the periodic and open systems in the case with a broken intracell link ($J_1 < J_2$ and the cut is on a J_2 link), the major difference is the emergence of the edge modes, which should be responsible for the density-density correlation at the boundary. For the case with a broken intercell link (with a cut on a J_1 link), the eigenstates are only perturbed after the boundary change, and no significant correlation emerges. However, the density-density correlation does not distinguish between the two configurations when U/J is large and the system is in the Mott insulating phase as shown in Figure 6.4 (e, f) since density fluctuations are suppressed as the interaction increases.

By comparing Figure 6.4(a) and (e) one can see the difference between the band-insulating and Mott-insulating phases as the density-density correlation vanishes in the interacting case. The transition between the band and Mott insulating phases of the dimerized lattice, however, is not sharp due to finite-size effect. Figure 6.4(c) shows that the correlation for $U/J_1 = 1$ does not decay to zero compared to the $U/J_1 = 5$ case. To examine where the system departs from the noninteracting limit, we analyze the fidelity metric for increasing interaction and show it in the inset of Figure 6.4. The fidelity metric is obtained from the fidelity $\mathcal{F}(U, \delta U) = \langle \psi(U) | \psi(U + \delta U) \rangle$ measuring the overlap of

ground states as the interaction is changed by $\delta U << J_1$. The fidelity metric

$$g = \frac{2}{L\delta U^2}\Big[1 - \mathcal{F}(U, \delta U)\Big] \qquad (6.6)$$

indicates quantum critical behavior or crossover with the appearance of singularities as a parameter is modified [25, 148, 73]. The fidelity metric shows that the transition regime is relatively broad, and $U/J_1 = 1$ in this case has not fully departed from the noninteracting point. By increasing the system size, the transition regime will get narrower and the contrast between the noninteracting and interacting cases will prevail even in the weakly-interacting regime. Nevertheless, the density-density correlation function and its dynamics provide additional evidence differentiating between the band-insulating and Mott-insulating phases. We remark that the determination of the spin or density correlations may need site-resolved spectroscopies, such as the quantum-gas microscope [11].

6.6 Conclusion

While solid state systems can reveal the influence of topological edge modes on transport, cold atoms can characterize topological properties directly associated with the wavefunction [31]. Since cold-atoms need to be confined in experiments, the confining potential distorts the density profile and hinders direct observation of topological edge modes. We propose a geometry suitable for generating edge modes in 1D by cutting open a ring lattice, and two dynamical probes for revealing the edge modes: One utilizes single-particle injection in real space and the other depletes the particles away from the boundary. Those methods exploit the localized nature of the edge modes and allow their density profiles to be mapped out.

Identifying and classifying topological properties of the interacting SSH model received theoretical progress for determining global behavior, but experimental verification can be challenging. Evaluating the time-evolution of selected correlation

functions provides a local probe of dimerization signatures and distinguishes interacting and noninteracting systems in different configurations. The setup and probes are general and should be useful for experimental verification of bulk-boundary correspondence and explore dynamics in other topological systems.

I would like to acknowledge my co-authors Prof. Chih-Chun Chien, Prof. Kevin Wright and Dr. Chen-Yen Lai in publication of these exciting ideas for edge state detection.

Chapter 7

Conclusion

This thesis provides a comprehensive analysis of fermion transport in quantum systems with theoretical studies done on non-equilibrium quantum dynamics and dynamics of systems in equilibrium. Below, I will summarize what is considered to be the paramount points of this work.

- Fermions in optical lattices can be used to study model Hamiltonians like the Hubbard model, and the systems can be engineered to explore quantum dynamics with controllable parameters in isolated environments.

- Lattice geometry can be used to manipulate the propagation of matter-waves. Speed of the matter waves can be enhanced by adding diagonal links to a square lattice. This is a pure quantum mechanical effect due to the wave nature of particles in the quantum mechanical regime. Mixing of the wave vectors by adding diagonal links contributes additional terms in the group velocity which provide a greater maximal group velocity with increased diagonal links.

- It is not possible to achieve equilibrium persistent current of fermions in an optical ring potential without the addition of an external dissipation since scattering mechanisms are not present in optical trapping systems. When driven periodically

by a synthetic magnetic field, competition between the relaxation time and the driving period leads to rate-dependent hysteresis of current. Area of the hysteresis loop depends on the relaxation time and resembles overdamped harmonic oscillator in the massless limit. Hysteresis of current is robust against interactions which do not change the eigenstate of the system, we demonstrate hysteresis is present with the addition of spin-orbit coupling.

- Detecting topological edge states in cold atom systems is a challenging task since the harmonic confining potential distorts the energy spectrum and fuses the edge states into the bulk. An optical ring potential cut by an off resonant laser beam provides a suitable confining potential to resolve the edge states. In the non-interacting limit, particle filling doesn't have an underlying role in the systems symmetry, and topological effects are observable with any particle filling. Two methods are proposed to resolve the edge states dynamically: single-site injection method and an atomic depletion method. Topology is poorly defined with interactions, however, in the case of the SSH model the system is topology is preserved by particle-hole symmetry at half-filling. Topological non-triviality can be observed by the persistence of finite spin-spin correlations as the boundary conditions are changed from periodic to open.

- Equilibrium current and corresponding quantum current correlations reveal periodic nature as Lissajous curves. Non-interacting curves are single valued with zero area and an isolated point resulting from the degeneracy. The addition of interactions make the current and fluctuations continuous producing multivalued Lissajous curves for any interaction, and the area decreases with increased interaction strength for a system at half filling. These two cases are topologically distinct. All points in the interacting case have a neighborhood, and the isolated point in the non-interacting system lacks any neighbors. Lissajous curves were calculated for an open quantum system connected to external reservoirs, indicating

global transport behavior.

As my thesis work has progressed remarkable progress in ultracold atoms has been made. For instance, the ability to realize synthetic dimensions, methods to detect Chern numbers for topological insulators, phonon modes mediated by optical cavities, and the ability to realize long-range interactions. The ability to realize long-range interactions in a controllable way insights opportunity to understand elusive phase transitions and the dynamics of particles whilst in a new phase.

Continuation of this work would be to further investigate the dynamics of fermions in engineered Hubbard ladders created using synthetic dimensions. A 2D square ladder with next-nearest-neighbor hopping accumulates a phase as a particle hops around a close loop when subjected to a perpendicular magnetic field. This system, better known has the Creutz' ladder (body-centered ladder geometry of Chapter 3), offers an exciting avenue for the investigation of topological insulators in the non-interacting, weakly interacting, and strongly interacting limit because the topological phase survives in the presence of interactions [78]. Investigations of the dynamics in this system could provide avenues to detect the edge-states and chiral currents. This research will open up a new avenue for transport studies in weakly and strongly interacting topological systems.

Theoretically limiting is the ability to simulate dynamics in of two-dimensional lattices, and future theoretical research would be to identify computational methods to get accurate results for these systems. A potential avenue would be to map the Hubbard Hamiltonian to superconducting qubits using quantum computing technology, and that's what I will find out at my next employment opportunity.

Appendix A

Appendices

A.1 Basis of Many-Body Wave-Function

The single particle basis is used when are no interactions between the different spin species of electrons. It works because no inter-particle correlations are necessary for calculation. All that needs to be known is nearest neighbor hopping and onsite energy. The basis extends over the sites, so the dimension of the Hamiltonian is determined by the sites.

In order to determine the many body wave function from single particle eigenstates, a Slater determinant is needed. The formalism is as follows,

$$|\lambda i\rangle = \tilde{a}_i^\dagger |0\rangle$$

$$\tilde{a}_i^\dagger = \sum_i \phi_i(l) a_l^\dagger$$

$$|n_1...n_N\rangle = \prod_i^{N_p} \tilde{a}_i^\dagger |0\rangle$$

$$|\Psi\rangle = \sum_{0 \leq n_1,...n_i \leq 1} c_{n_1,...n_i} |n_1...n_i\rangle$$

$$c_{n_1,...n_i} = \sum_{1<l_1...l_n} \begin{vmatrix} \phi_1(l_1) & ... & \phi_1(l_N) \\ . & . & . \\ \phi_N(l_1) & ... & \phi_N(l_N) \end{vmatrix}$$

where l_i is an eigenvector of the single particle Hamiltonian and N_p is the number of particles. In order to determine the full ground state wave function all the different ways to arrange particles in the system have a coefficient. The ground state wave function is expanded over the Fock basis and the expansion coefficients are determined by Slater determinants from the single-particle basis eigenvectors. $\phi_i(l_i)$ represents the i$^\text{th}$ element of the i$^\text{th}$ eigenvector in the single particle basis.

Example: Find coefficient for $|011\rangle$ state

$$c_{|110\rangle} = \begin{vmatrix} \phi_2(l_2) & \phi_2(l_3) \\ \phi_3(l_2) & \phi_3(l_3) \end{vmatrix} = \phi_2(l_2)\phi_3(l_3) - \phi_2(l_3)\phi_3(l_2) \tag{A.1}$$

A.1.1 Second Quantization for Bosons

Bosons have a symmetric wave function which permits multiple particle occupation on a state. The creation and annihilation operators are different than fermions. The creation operator creates a particle on a state

$$b_\nu^\dagger |n_\nu\rangle = \sqrt{n_\nu + 1}|n_\nu\rangle. \tag{A.2}$$

The annihilation operator removes a particle from a state

$$b_\nu |n_\nu\rangle = \sqrt{n_\nu}|n_\nu - 1\rangle. \tag{A.3}$$

These operators commute due to the symmetry of the wave function $[A, B] = AB - BA$. The commutation relations for the creation and annihilation operators are as follows:

$$[b_{\nu'}, b_\nu^\dagger] = \delta_{\nu'\nu} \tag{A.4a}$$

$$[b_{\nu'}^\dagger, b_\nu^\dagger] = [b_{\nu'}, b_\nu] = 0 \tag{A.4b}$$

The number operator $b_\nu^\dagger b_\nu$ can be all positive integers or zero. It should also be noted that the counting is different for bosons, since the wave function is symmetric and multiple occupancy permitted. For a single spin species the Hilbert space dimension can be calculate as

$$\mathcal{H} = \frac{(N_p + N - 1)!}{N_p!(N-1)!}. \tag{A.5}$$

The Fock space for bosons is greater than the Fock space for fermions, however, if cooled below a critical temperature they all occupy the ground state and can be modeled with a single particle wave function.

A.2 Numerical Algorithms

A.2.1 Exact Diagonalization Computation

The most important aspect of exact diagonalization is determining the diagonal elements for interaction. The full Fock basis is constructed from a tensor product of the single particle sub-spaces, so the mixing between the states is essential. **Example of Fock state**

$$|011\rangle \, |001\rangle$$

In order to determine the mixing the basis needs to be constructed and indexed.

Creating Basis

The individual Fock states can be represented with binary numbers. For instance, $|011\rangle$ corresponds to the number 3. Quick on binary: each bit represents an integer to the power of two, so the N$^{\text{th}}$ bit is 2^N. The binary sequence for three $2^0 + 2^1 = 3$

First, a given number of sites and particles are needed, we will continue the example with M=3 and N=2. All the fock states are:

- $|011\rangle = 3 = 1$

- $|101\rangle = 5 = 2$

- $|110\rangle = 6 = 3$

It is apparent the smallest integer allowed is when N particles are on the right, and the most is when N particles are on the left. This sets the bound for the integer representation of the Fock basis, and is computed by

$$I_{min} = \sum_{i=1}^{N} 2^{i-1}$$

$$I_{max} = \sum_{i=1}^{N} 2^{M-i}$$

Once the min and max ranges have been determined the basis can be created. A loop runs over all the possible integers in between min and max. An algorithm checks whether the ith bit is set corresponding to the site. If the number of bits set is equal to the number of particles it is a Fock state. For example, $4 = |100\rangle$ which only has one bit set, therefore not a Fock state for a two particle system.

The states are indexed from lowest to highest value, see Table 1, and the total index is the size of the Fock basis. It is important to know that the index integer is unique to each Fock state

Total Index

It is important that each Fock state has its own unique integer associated to it so the computer can reference the state. Each up spin has to be matched with all possible down spin combinations. Once way to do this is to put them in front of each other.

Example of Index for Fock state

$$|011\rangle \, |001\rangle$$

$$I = 001 - 011 = 3 + 8 = 11$$

Up	$Basis_\uparrow$	$Index_\uparrow$	Down	$Basis_\downarrow$	$Index_\downarrow$	Total Index
011	3	1	001	1	1	1
101	5	2	001	1	1	2
110	6	3	001	1	1	3
011	3	1	010	2	2	4
101	5	2	010	2	2	5
110	6	3	010	2	2	6
011	3	1	100	4	3	7
101	5	2	100	4	3	8
110	6	3	100	4	3	9

Table A.1: Basis states and Index number for a system with $L = 3$ sites, $N_\uparrow = 2$ and $N_\downarrow = 1$. Each basis state has an individual index and the Fock state referenced by the Total Index. These values are stored into vectors.

This will give a unique integer and can be shown mathematically from Lin's two table method as

$$I = \sum_{i=1}^{M}[n_\uparrow(i)2^{i-1} + n_\downarrow(i)2^{M+i-1}]$$

However this is not what is done is our algorithm. The indexing is ordered so the product of the two Fock states with the smallest integers are 1 and the two Fock states with the largest integers give $I_{tot} = \nu_\sigma \nu_{\bar\sigma} = count_\uparrow count_\downarrow$ This can be done if

$$Index = (Index_\downarrow - 1)count_\uparrow + Index_\uparrow$$

If more spin states are added it can be modified as

$$I = \sum_{i=1}^{N_\sigma}(I_i - 1)(\prod_{j=1}^{N_\sigma-1} count_j)$$

where N_σ is the number of spin states in the system.

A.2.2 Hopping Matrix and Binary Functions

The creation and annihilation operators can be realized computationally by using bitwise functions to operate on the Fock states. First a little bit about bitwise operators:

- shift operator $<<$ moves a digit a certain number of places $1 << 2 = 2$ or $001 \leftarrow 100$

- AND operator, &, evaluates two integers and returns a 1 when both are set to 1

$$1001010$$
$$0101010$$
$$= 0001010$$

- OR operator, $|$, is one when either of the bits is 1. You get a nonzero number if the bit you are interested in is 1

$$1001010$$
$$0101010$$
$$= 1101010$$

- Complement operator, ~, flips all the bits. 1 becomes 0 and 0 becomes 1

The annihilation operator can be realized with a bit clear function, which will clear the nth bit on some integer m It is written as

$$Clrbit = m\& \sim (1 << n)$$

This shifts the number 001 n bits to the left. It is then flipped so the nth bit is 0. When evaluated with & the nth bit is 1-0=0.

The creation operator is realized with the bitset function. Where the nth bit was cleared, the n+1 bit is set to 1. If it is already 1 the or function will set it to 0, and it will be discarded.

$$NewState = m|(1 << (n))$$

Once the new state is found after hopping the integer is matched with it's index. The index is used, as shown above, to determine the correct element of the hopping hamiltonian

Hopping between next-nearest negihbors has to account for the antisymmetry of the wave function. The matrix element $c_i^\dagger c_i + 2$ is calculated in the same way as nearest neighbor elements using the Clrbit and bitset functions. An additional Bittest function, $Bittest = m\&(1 << n)$,is used to check occupancy on the site $i + 1$. If the bit is set to 1, meaning the site is occupied than the matrix element gains a negative sign. If the bit is 0, than no changes are made to the matrix element. Working with periodic boundary condtions antisymmetry needs to be accounted for as the boundary is crossed. This is done using the same Bittest function, but all site occupancies between the first and last are tested. An odd number of particles requires a negative sign on the matrix element, and an even number of particles leaves the element unchanged.

Building Interactions

The first step is to have some map to tell you which state have a particle on which site. This is done by building an interaction index matrix $L \times point$ where point are the number of occupied (unoccupied) sites in a given basis state. What this matrix is depends on the number of particles. If $N_\uparrow + N_\downarrow > L$ then the number of unoccupied sites over each basis is counted. If $N_\uparrow + N_\downarrow \leq L$ the the number of occupied site is counted. This index will let the computer know when a Fock state has double occupation on a site.

Example of Index matrix: counting occupied

- $|011\rangle = 1$ The numbers refer to index

- $|101\rangle = 2$

- $|110\rangle = 3$

$$IndexU = \begin{pmatrix} 1 & 2 \\ 1 & 3 \\ 2 & 3 \end{pmatrix}$$

This matrix says on index 1 there are particles on site 1 and 2, on index 2 there are particle on site 1 and 3 and on index 3 there are particles on site 2 and 3. By referencing the interaction index all of the diagonal elements are generated for the doubly occupied sites in a given Fock state.

A.2.3 Lanczos Diagonalization

The Lanczos diagonalization technique is efficient in obtaining ground state eigenvalues for Hamiltonians with large Hilbert spaces [117]. It takes a very large matrix and converts it into a tridiagonal dense matrix. This is done by a matrix built in Krylov space. The transformation will satisfy the equation

$$H_{N \times N} K_{N \times M} = K_{N \times M} T_{M \times M} \tag{A.6}$$

The space has an orthogonal basis and with Hamiltonians we call them Lanczos vectors $\{\phi_0, \phi_1, ..., \phi_M\}$ and they have the dimension of the total Fock basis. The first Lanczos vector, ϕ_0, is all you need to begin with, and it is a completely random vector. This vector then needs to be normalized, which is easy with built in Eigen functions. The rest of the process will be listed as steps.

1. Create r-vector $|r\rangle = H |\phi_0\rangle$

2. Next this r-vector needs to be orthonormal with the first Lanczos vector and this gives the α coefficient which is on the diagonal part of the T-matrix $\alpha_0 = \langle \phi_0 | r \rangle$

3. Now we determine the $|r'\rangle$ vector which will make sure the $|\phi_1\rangle$ is orthogonal. $|r'\rangle = |r\rangle - \alpha_0 |\phi_0\rangle$

4. The off diagonal elements are obtained by normalizing $|r'\rangle$ we get the off-diagonal elements, $\beta = |\langle r' | r' \rangle|$

5. The new $|\phi_1\rangle$ will be used to find the next $|r\rangle$.

$$|r\rangle = H\,|\phi_j\rangle - \beta_j\,|\phi_{j-1}\rangle$$

6. Repeat process until $\beta = 0$. When $\beta = 0$ the above transformation of the Hamiltonian to the tridiagonal matrix is satisfied. However in our algorithm we diagonalize the T-matrix on every iteration, and when the difference between the eigenvalues is 0 the transformation is satisfied.

Once the eigenvalues of the T-matrix have been obtained, the smallest eigenvalue corresponds to the ground state. Multiplying the corresponding eigenvector by the K-matrix will give the ground state of the Hamiltonian.

$$T_m s_i^m = \nu_i^m s_i^m$$

$$H K_m s_i^m = K_m T_m s_i^m = \nu_i^m K_m s_i^m$$

$$|G\rangle = K_m s_i^m$$

Once the ground state has been found it needs to be converted to the ground state wave function

$$|\Psi\rangle = \sum_{i=1}^{N} c_i\,|F\rangle$$

where the c_i's are the coefficients from $|G\rangle$. The on-site expectation values of number are found the following way

$$\langle n(x)\rangle = \langle G|n(x)|G\rangle$$

$$= \sum_{i=1}^{N} |c_i|^2\,\langle F|n(x)|F\rangle$$

It is important to note that the number operator acts on one spin, so the operations need to be applied on both spin up and spin down. The expectation value can simply be found by using the bittest function to determine the expectation of finding a particle on site x.

A.2.4   Time-Evolution with Lanczos Algorithm

To calculate the ground state over time we continue to work in Krylov-space using the Lanczos algorithm. The main purpose it to evaluate the time evolution operator using the tridiagonal matrix and the associated Lanczos vectors. The ground state from the previous iteration is the first Lanczos vector in the matrix K. The time evolution operator is for time step $t \rightarrow t + dt$ is

$$\hat{U}_{dt} = e^{-iHdt/\hbar} \tag{A.7}$$

Referring back to equation A.6 we can write the Hamiltonian in terms of the tridiagonal matrix and the matrix of Lanczos vectors.

$$H = KTK^{\dagger}$$

$$
\begin{aligned}
\hat{U}_{dt} &= e^{-iKTK^{\dagger}dt/\hbar} \\
&= 1 - \left(\frac{idt}{\hbar}KTK^{\dagger}\right) + \frac{1}{2}\left(-\frac{idt}{\hbar}KTK^{\dagger}\right)^2 + \mathcal{O}(n) \\
&= 1 - \left(\frac{idt}{\hbar}KTK^{\dagger}\right) + \frac{1}{2}\left(-\frac{idt}{\hbar}\right)^2 KTK^{\dagger}KTK^{\dagger} \\
&= 1 - \left(\frac{idt}{\hbar}KTK^{\dagger}\right) + \frac{1}{2}\left(-\frac{idt}{\hbar}\right)^2 KT^2K^{\dagger} \\
&= K\left[1 - \left(\frac{idt}{\hbar}KTK^{\dagger}\right) + \frac{1}{2}\left(-\frac{idt}{\hbar}\right)^2 T^2\right]K^{\dagger} \\
&= Ke^{-iTdt/\hbar}K^{\dagger} \tag{A.8}
\end{aligned}
$$

We can then easily evolve the ground state using the time-evolution operator as above and breaking down T even further with $T = UDU^{\dagger}$ were D is the diagonal matrix containing the eigenvalues we obtain the time-evolved ground state.

$$
\begin{aligned}
|\psi(t + dt)\rangle &= Ke^{-iTdt/\hbar}K^{\dagger}|\psi(t)\rangle \\
&= KUe^{-iDdt/\hbar}U^{\dagger}K^{\dagger}|\psi(t)\rangle \tag{A.9}
\end{aligned}
$$

Error arises from the truncation of the Krylov space, and the number of Lanczos vectors, n, used. Typically n is no larger than 20, and in the time-evolved calculations we use $n = 9$.

A.2.5   Runge Kutta

The equation of motion derived from the time-evolution of the correlation matrix is a first-ordered differential equation.   A fourth-ordered Runge-Kutta algorithm was implemented to determine time-dependent observables in a non-interacting system. Runge-Kutta is a more symmetric version of the Euler method

$$y_{n+1} = y_n + hf(x_n, y_n), \tag{A.10}$$

and the solution progresses from $x_n \to x_{n+1} = x_n + h$. Essentially what the Euler method gives is a crude solution to a first-order differential equation

$$\frac{y_{n+1} - y_n}{h} = \frac{dy}{dx} = f(x_n, y_n). \tag{A.11}$$

In time evolution the discritized step $h = \Delta t$. The Runge-Kutta method breaks the interval between steps h into pieces using a mid-point method. The fourth-order method is broken into four pieces with more weight coming from the mid-points in the total solution

$$k_1 = hf(x_n, y_n) \tag{A.12a}$$

$$k_2 = hf(x_n + \frac{1}{2}h, y_n + \frac{1}{2}k_1) \tag{A.12b}$$

$$k_3 = hf(x_n + \frac{1}{2}h, y_n + \frac{1}{2}k_2) \tag{A.12c}$$

$$k_4 = hf(x_n + h, y_n + k_3) \tag{A.12d}$$

$$y_{n+1} = y_n + \frac{1}{6}k_1 + \frac{1}{3}k_2 + \frac{1}{3}k_3 + \frac{1}{6}k_4 + \mathcal{O}(h^5). \tag{A.12e}$$

Evolving the correlation matrix $y_n \to (c_i^\dagger c_j)_n$, $x_n \to t_n$.The subscript n denotes the time step, so the initial value for the function of a previous step is used to obtain the value of the next step. The error scales as h^{m+1}, where m is the order of the method implemented.

A.2.6   Root Finding with GSL

In order to determine the chemical potential of the Fermi-Dirac distribution a root finding method was implemented with GSL. In the initial conditions the total number of atoms is given, and the equation is:

$$N_{tot} = \sum_n \frac{1}{e^{-\beta(\epsilon_n - \mu)} + 1}$$

Since the energy changes with ϕ a different chemical potential is needed for each value of flux. Flux has a linear relationship with time, which is used to determine the loop used to evaluate all values of ϕ. Here To is the time to reach $\phi = 0.5$.

$$\phi = \frac{t}{2T_0}$$

$$T_\phi = \frac{T_0}{dt}$$

The root finding method is then embedded within a for loop running from 0 to T_ϕ and the resulting μ is placed in a one dimensional array to be called later.

A false positive algorithm is the most accurate root finding method used and is defined:

Two endpoints (a,f(a)) and (b,f(b)) are connected by a line, and the point where this line crosses the x-axis taken as a midpoint. The function value at the midpoint is calculated and its sign, be it positive or negative, is used to determine which side of the interval **does not** *contain a root. By discarding the side without a root a smaller interval containing the root is determined. This procedure is continued until a root is found in a small enough interval.*

Once the roots have been found it is necessary to determine the fermi-function for all values of n as t goes from 0 to T_0.

A.2.7   Numerical Integration

Start with $dy/dx = f(x)$ and $y = \int_{x_0}^{x_1} f(x)dx$ where $x_i = x_0 + ih$. Elementary calculus may lead one to think numerical integration can be done using Riemann sums,

however, this method will lead to large amounts of error. The most simple form of numerical integration is to use the trapezoidal rule:

$$\int_{x_0}^{x_1} f(x)dx = h\left[\frac{1}{2}f_0 + \frac{1}{2}f_1\right] + \mathcal{O}(h^3 f''). \tag{A.13}$$

Essentially with the trapezoidal rule their is a line connecting the points, and the equation becomes similar to calculating the area of a trapezoid. This two-point method is exact for polynomials of degree 1 (i.e. a line). For more higher ordered polynomials, functions with larger curvature, this method can lead to large error as well, and methods have been devised to take a greater number of points. In the calculation of the relaxed Fermi-distribution function, a five-point formula was used called Bode's rule:

$$\int_{x_0}^{x_4} f(x)dx = h\left[\frac{14}{45}f_0 + \frac{64}{45}f_1 + \frac{24}{45}f_2 + \frac{64}{45}f_3 + \frac{14}{45}f_4\right] + \mathcal{O}(h^7 f^{(6)}). \tag{A.14}$$

For more functions with greater curvature higher-order formulas can be used, if necessary.

A.3   Band Calculations

When calculating the dispersion one must have the primitive lattice vectors to translate the primitive cell and the Bravais lattice vector $\mathbf{R} = n_1\vec{a}_1 + n_2\vec{a}_2$ where n is some integer. Determining the dispersion for a 2D with only a single site per unit cell I start with the tight binding Hamiltonian in real space

$$H = \sum_{\langle ij\rangle} -\bar{t}(c_i^\dagger c_j + c_j^\dagger c_i) \tag{A.15}$$

Using the Fourier transform, operators are converted into momentum space $c_i = \sum_k c_k \exp(ik \cdot \mathbf{R})$ and $c_i^\dagger = \sum_p \sum_{\mathbf{R}} c_p \exp(-ip \cdot \mathbf{R})$. The Hamiltonian can be written as

$$H_k = -\bar{t}\sum_{kp}\sum_{\mathbf{R}}(c_k^\dagger c_p e^{i(p-k)\cdot x_i}e^{ip\cdot\mathbf{R}} + c_k^\dagger c_p e^{i(p-k)\cdot x_j}e^{-ik\cdot\mathbf{R}}). \tag{A.16}$$

The series representation for the Dirac Delta function is $\delta(k - k') = \sum_k e^{i(k-k')x}$, and this relationship is implemented on the above Hamiltonian where the Hamiltonian has value only when $p = k$

$$H_k = -\bar{t} \sum_k \sum_{\mathbf{R}} (c_k^{\dagger} c_k e^{ik \cdot \mathbf{R}} + c_k^{\dagger} c_k e^{-ik \cdot \mathbf{R}}). \tag{A.17}$$

Energy dispersion obtained from the Hamiltonian above is $\epsilon_k = -\bar{t} \sum_{\mathbf{R}} (e^{ik \cdot \mathbf{R}} + e^{-ik \cdot \mathbf{R}})$ Below are the analytic derivations of the band structure for the lattices studied in this work.

A.3.1 Square Lattice

The square lattice is connected to neighbors by the primitive vector $\vec{a}_1 = l\hat{x}$ and $\vec{a}_2 = l\hat{y}$ where $l = 1$ is the lattice constant connecting sites. Using the relationship above for the dispersion we find

$$\begin{aligned}
\epsilon(k) &= -\bar{t} \left[e^{ik \cdot a_1} + e^{-ik \cdot a_1} + e^{ik \cdot a_2} + e^{-ik \cdot a_2} \right] \\
&= -\bar{t} \left[e^{ik_x l} + e^{-ik_x l} + e^{ik_y l} + e^{-ik_y l} \right] \\
&= -2\bar{t} \cos(k_x l) - 2\bar{t} \cos(k_y l)
\end{aligned} \tag{A.18}$$

where the Euler's formula was used to obtain the cosine function.

A.3.2 Triangle Lattice

Three vectors connect the triangle lattice's unit cell to its neighbors: $\vec{a}_1 = l\hat{x}$, $\vec{a}_2 = l/2\hat{x} + \sqrt{3}l/2\hat{y}$, $\vec{a}_3 = l/2\hat{x} - \sqrt{3}l/2\hat{y}$. The first two of these is are the primitive vectors while the third is a Bravais lattice vector $\mathbf{R} = 2\vec{a}_1 - \vec{a}_2$. We use these vectors to obtain the dispersion for the triangle lattice

$$\begin{aligned}
\epsilon(k) &= -\bar{t} \left[e^{ik \cdot a_1} + e^{-ik \cdot a_1} + e^{ik \cdot a_2} + e^{-ik \cdot a_2} + e^{ik \cdot a_3} + e^{-ik \cdot a_3} \right] \\
&= -\bar{t} \left[2\cos(k_x l) + 2\cos(\frac{k_x l}{2} + \frac{\sqrt{3}k_y l}{2}) + 2\cos(\frac{k_x l}{2} - \frac{\sqrt{3}k_y l}{2}) \right] \\
&= -2\bar{t} \left[\cos(k_x l) + 2\cos(\frac{k_x l}{2}) \cos(\frac{\sqrt{3}k_y l}{2}) \right]
\end{aligned} \tag{A.19}$$

where the trigonometric identity $\cos(u \pm v) = \cos(u)\cos(v) \mp \sin(u)\sin(v)$ was used.

A.3.3 Cross-Linked Lattice

The cross-linked lattice has two sites (A,B) in the primitive cell with the lattice constant l being the distance between sites A and B. To calculate the dispersion the transitions within the primitive cell and between primitive cell we need a 2×2 matrix with the form

$$\begin{pmatrix} AA & BA \\ AB & BB \end{pmatrix}. \tag{A.20}$$

There are two lattice vectors as the unit cell is translated to create the lattice: $\vec{a}_1 = l\hat{x} + l\hat{y}$, $\vec{a}_2 = l\hat{x} - l\hat{y}$. I will use three matrices to describe the lattice which I will combine to get the energy. The first describes the hopping within the primitive cell

$$H_{intra} = \begin{pmatrix} 0 & -\bar{t} \\ -\bar{t} & 0 \end{pmatrix}. \tag{A.21}$$

The second is the matrix associated with the first vector translated to the upper right

$$H_{a_1} = \begin{pmatrix} -\bar{t} & -\bar{t} \\ 0 & -\bar{t} \end{pmatrix} e^{ik \cdot \vec{a}_1}. \tag{A.22}$$

We then take the vector as the cell is translate to the lower left

$$H_{-a_1} = \begin{pmatrix} -\bar{t} & 0 \\ -\bar{t} & -\bar{t} \end{pmatrix} e^{-ik \cdot \vec{a}_1}. \tag{A.23}$$

Next considered is the translation to the lower right using the second lattice vector

$$H_{a_2} = \begin{pmatrix} -\bar{t} & -\bar{t} \\ 0 & -\bar{t} \end{pmatrix} e^{ik \cdot \vec{a}_2}, \tag{A.24}$$

and also it's conjugate partner the upper left

$$H_{-a_2} = \begin{pmatrix} -\bar{t} & 0 \\ -\bar{t} & -\bar{t} \end{pmatrix} e^{-ik \cdot \vec{a}_2}. \tag{A.25}$$

Summing these together we get the total Hamiltonian in momentum space

$$H(k) = H_{intra} + H_{a_1} + H_{-a_1} + H_{a_2} + H_{-a_2}$$

$$= \begin{pmatrix} -2\bar{t}(\cos(k_x l + k_y l) + \cos(k_x l - k_y l)) & -\bar{t}(1 + 2e^{ik_y l}\cos k_x l) \\ -\bar{t}(1 + 2e^{-ik_y l}\cos k_x l) & -2\bar{t}(\cos(k_x l + k_y l) + \cos(k_x l - k_y l)) \end{pmatrix}$$

$$= \begin{pmatrix} -4\bar{t}\cos(k_x l)\cos(k_y l) & -\bar{t}(1 + 2e^{ik_y l}\cos k_x l) \\ -\bar{t}(1 + 2e^{-ik_y l}\cos k_x l) & -4\bar{t}\cos(k_x l)\cos(k_y l) \end{pmatrix}$$

$$(A.26)$$

We can obtain the dispersion $\epsilon(k)$ from the eigenvalues of this Hamiltonian. A Hermitian Hamiltonian

$$\begin{pmatrix} A & B \\ B^* & A \end{pmatrix} \tag{A.27}$$

possessing the same diagonal elements can be easily diagonalized giving the energy $E = A \pm |B|$. Thus we have

$$\epsilon(k) = -4\bar{t}\cos(k_x l)\cos(k_y l) \pm \bar{t}\sqrt{1 + 4\cos(k_x l)\cos(k_y l) + 4\cos^2(k_x l)}.$$

A.3.4   SSH Lattice

The SSH model is a 1D topological lattice structure with alternating hopping strengths has 2 sites per unit cell and a lattice constant l between unit cells. Constructing the Hamiltonian using Hubbard model with alternating hopping strengths we have

$$H = \sum_{n=0}^{N} J_1 c_{A,n}^\dagger c_{B,n} + J_2 c_{a,n+1}^\dagger c_{b,n} + h.c. \tag{A.28}$$

where N is the number of unit cells and J1 and J2 represent the alternating hopping strengths. To determine the band structure of the system we take a Fourier transform of the creation (annihilation) operator such that

$$c_a = \sum_{k \in BZ} a_k e^{ik \cdot x_i}$$

$$c_{i,B} = \sum_{k \in BZ} b_k e^{ik \cdot (x_i + a/2)}$$

with $x_i = i \cdot a$ and a is the unit vector. In a spinor basis we construct our Hamiltonian in the form

$$\begin{vmatrix} c_A^\dagger c_A & c_A^\dagger c_B \\ c_B^\dagger c_A & c_B^\dagger c_B \end{vmatrix}$$

This is equivalent to

$$\begin{pmatrix} c_{A,i}^\dagger & c_{B,i}^\dagger \end{pmatrix} \begin{vmatrix} 0 & J_1 \\ J_1 & 0 \end{vmatrix} \begin{pmatrix} c_{A,i} \\ c_{B,i} \end{pmatrix} + \begin{pmatrix} c_{A,i+1}^\dagger & c_{B,i+1}^\dagger \end{pmatrix} \begin{vmatrix} 0 & J_2 \\ J_2 & 0 \end{vmatrix} \begin{pmatrix} c_{A,i} \\ c_{B,i} \end{pmatrix}$$

Taking the Fourier transform we can compose the Hamiltonian in energy space to get the dispersion with

$$H(k) \left| \psi \right\rangle = E(k) \left| \psi \right\rangle$$

$$H(k) = \begin{pmatrix} a_k^\dagger & b_k^\dagger \end{pmatrix} h(k) \begin{pmatrix} a_k \\ b_k \end{pmatrix}$$

$$h(k) = \begin{vmatrix} 0 & J1 e^{ika/2} + J_2 e^{-ika/2} \\ J_1 e^{-ika/2} + J_2 e^{ik/2} & 0 \end{vmatrix}$$

Looking at out $H(k)$ we can use Euler's Theorem and let $e^{ik} = \cos(k) + i\sin(k)$ our Hamiltonian can be written as

$$\begin{aligned} h(k) &= \begin{pmatrix} 0 & J_1 \cos(\frac{kl}{2}) + J_1 \sin(\frac{kl}{2}) + J_2 \cos(\frac{kl}{2}) - J_2 \sin(\frac{kl}{2}) \\ J_1 \cos(\frac{kl}{2}) - J_1 \sin(\frac{kl}{2}) + J_2 \cos(\frac{kl}{2}) + J_2 \sin(\frac{kl}{2}) & 0 \end{pmatrix} \\ &= \begin{pmatrix} 0 & re^{i\theta} \\ re^{-i\theta} & 0 \end{pmatrix} \end{aligned} \tag{A.29}$$

On the complex plane we can define the real axis as $a = (J_1 + J_2)\cos(\frac{kl}{2})$ and the imaginary access as $b = (J_1 - J_2)\sin(\frac{kl}{2})$. The radius and angle of the Euler formula is

give as

$$r = \sqrt{a^2 + b^2} \tag{A.30}$$

$$\theta = \arctan\left(\frac{a}{b}\right) \tag{A.31}$$

Diagonalizing this one will find the dispersion $\epsilon(k) = r = \sqrt{a^2 + b^2}$ yielding

$$\epsilon(k) = \pm\sqrt{J_1^2 + J_2^2 + 2J_1 J_2 \cos(k)}. \tag{A.32}$$

Bibliography

[1] M. Acharyya and B.K. Chakrabarti. "Annual Reviews of Computational Physics 1". In: ed. by Dietrich Stauffer. Vol. 1. World Scientific, 1994. Chap. Ising System in an Oscillating Field: Hysteretic Response.

[2] M. Aidelsburger et al. "Realization of the Hofstadter Hamiltonian with Ultracold Atoms in Optical Lattices". In: *Phys. Rev. Lett.* 111 (2013), p. 185301.

[3] Eric Akkermans and Gilles Montambaux. *Mesoscopic Physics of Electrons and Photons*. Cambridge, 2007.

[4] Eric Akkermans and Gilles Montambaux. *Mesoscopic Physics of Electrons and Photons*. Cambridge University Press, 2007.

[5] Hisham A. H. Al-Khazali and Mohamad R. Askari. "Geometrical and Graphical Representations Analysis of Lissajous Figures in Rotor Dynamic System". In: *IOSR Journal of Engineering* 2 (2012), p. 5.

[6] Emil A Yuzbashyan Boris L Altshuler and B Sriram Shastry. "The origin of degeneracies and crossings in the 1d Hubbard model". In: *J. Phys. A* 35 (2002), pp. 7525–7547.

[7] E. Anisimovas et al. "Semisynthetic zigzag optical lattice for ultracold bosons". In: *Phys. Rev. A* 94 (2016), p. 063632.

[8] János K. Asbóth, László Oroszlány, and András Pályi. "A Short Course on Topological Insulators:Band-structure topology and edge states in one and two dimensions". ArXiv 1509.02295. 2015. URL: `http://arxiv.org/abs/1509.02295{\%}5Cnhttp://www.springer.com/us/book/9783319256054`.

[9] N W Ashcroft and N D Mermin. *Solid state physics*. Thomson Learning, 1976.

[10] Marcos Atala et al. "Observation of chiral currents with ultracold atoms in bosonic ladders". In: *Nat. Phys.* 10 (2014), p. 510.

[11] Waseem S Bakr et al. "A quantum gas microscope for detecting single atoms in a Hubbard-regime optical lattice." In: *Nature* 462.7269 (2009), pp. 74–77. ISSN: 0028-0836. DOI: `10.1038/nature08482`.

[12] G. Barontini et al. "Controlling the Dynamics of an Open Many-Body Quantum System with Localized Dissipation". In: *Phys Rev. Letters* 110 (2013), p. 035302.

[13] Daniel Barredo et al. "An atom-by-atom assembler of defect-free arbitrary two-dimensional atomic arrays". In: *Science* 354 (2016), p. 1021.

[14] C. Becker et al. "Ultracold Quantum gases in triangular optical lattices". In: *New J. Phys* 12 (2010), p. 065025.

[15] A. Bermudez, L. Amico, and M. A. Martin-Delgado. "Dynamical delocalization of Majorana edge states by sweeping across a quantum critical point". In: *New J. Phys.* 12.5 (2009), p. 55014. ISSN: 1367-2630. DOI: `10.1088/1367-2630/12/5/055014`. URL: `http://arxiv.org/abs/0907.3134`.

[16] Giorgio Bertotti. *Hysteresis in Magnetism: for physicists, material scientists and engineers*. Academic Press, 1998.

[17] J.-Y. Bigot et al. "Electron Dynamics in Copper Metallic Nanoparticles Probed with Femtosecond Optical Pulses". In: *Phys Rev. Letters* 75.25 (1995), pp. 4702–2705.

[18] F. Bloch. "Nuclear Induction". In: *Phys. Rev.* 70 (1946), p. 460.

[19]   I. Bloch, J. Dalibard, and S. Nascimbéne. "Quantum simulations with ultracold quantum gases". In: *Nat. Phys.* 8 (2012), pp. 267–276.

[20]   Immanuel Bloch. "Ultracold quantum gases in optical lattices". In: *Nat. Phys.* 1 (2005), pp. 23–30.

[21]   M. Buttiker, Y. Imry, and R. Landauer. "Josephson Behavior in Small Normal One-Dimensional Rings". In: *Phys. Lett. A* 96A.7 (1983), p. 327.

[22]   W Cai and V Shalaev. *Optical Metamaterials*. New York: Springer, 2010.

[23]   Seth C Caliga et al. "Transport dynamics of ultracold atoms in a triple-well transistor-like potential". In: *New J. Phys.* 18.2 (2016), p. 25010. ISSN: 1367-2630. DOI: `10.1088/1367-2630/18/2/025010`. URL: `http://dx.doi.org/10.1088/1367-2630/18/2/025010`.

[24]   Adolfo del Campo, Malcolm G Boshier, and Avadh Saxena. "Bent waveguides for matter-waves: supersymmetric potentials and reflectionless geometries." In: *Sci. Rep.* 4 (2014), p. 5274. ISSN: 2045-2322. DOI: `10.1038/srep05274`. arXiv: `1311.2062v1`. URL: `http://www.pubmedcentral.nih.gov/articlerender.fcgi?artid=4053736{\&}tool=pmcentrez{\&}rendertype=abstract`.

[25]   L. Campos Venuti et al. "Fidelity approach to the Hubbard model". In: *Phys. Rev. B* 78.11 (2008), p. 115410. ISSN: 10980121. DOI: `10.1103/PhysRevB.78.115410`.

[26]   A. Celi et al. "Synthetic Gauge Fields in Synthetic Dimensions". In: *Phys. Rev. Lett.* 112 (2014), p. 043001.

[27]   P.M. Chaikin and T.C. Lubensky. *Principles of Condensed Matter Physics*. Cambridge University Press, 1995.

[28]   V. Chandrasekhar et al. "Magnetic Response of a Single, Isolated Gold Loop". In: *Phys. Rev. Lett.* 67.25 (1991), p. 3578.

[29] Gia-Wei Chern, Chih-Chun Chien, and Massimiliano Di Ventra. "Dynamically generated flat-band phases in optical kagome lattices". In: *Phys. Rev. A* 90 (2014), p. 013609. URL: `http://link.aps.org/doi/10.1103/PhysRevA.90.013609`.

[30] C Chien and M Di Ventra. "Dynamical crossover between the infinite-volume and empty-lattice limits of ultra-cold fermions in 1D optical lattices". In: *EPL* 99 (2012), p. 40003.

[31] C C Chien, S Peotta, and M Di Ventra. "Quantum transport in ultracold atoms". In: *Nat. Phys.* 11 (2015), p. 998.

[32] Chih-Chun Chien, Massimiliano Di Ventra, and Michael Zwolak. "Landauer, Kubo, and microcanonical approaches to quantum transport and noise: A comparison and implications for cold-atom dynamics". In: *Phys. Rev. A* 90 (2 2014), p. 023624. DOI: `10.1103/PhysRevA.90.023624`. URL: `http://link.aps.org/doi/10.1103/PhysRevA.90.023624`.

[33] Chih-Chun Chien, Michael Zwolak, and Massimiliano Di Ventra. "Bosonic and fermionic transport phenomena of ultracold atoms in one-dimensional optical lattices". In: *Phys. Rev. A* 85 (4 2012), p. 041601. DOI: `10.1103/PhysRevA.85.041601`. URL: `http://link.aps.org/doi/10.1103/PhysRevA.85.041601`.

[34] Ching-Kai Chiu et al. "Classification of topological quantum matter with symmetries". In: *Rev. Mod. Phys.* 88.September (2016), p. 035005. DOI: `10.1103/RevModPhys.88.035005`.

[35] J. I. Cirac and P. Zoller. "New Frontiers in Quantum Information With Atoms and Ions". In: *Physics Today* 57 (2004), p. 38.

[36] S R Clark and D Jaksch. "Dynamics of the superfluid to Mott-insulator transition in one dimension". In: *Phys. Rev. A* 70 (2004), p. 043612. URL: `http:`

```
//journals.aps.org/pra/abstract/10.1103/PhysRevA.70.
043612.
```

[37] Marco Cominotti et al. "Optimal Persistent Currents for Interacting Bosons on a Ring with a Gauge Field". In: *Phys. Rev. Lett.* 113.025301 (2014).

[38] Laurent Corte et al. "Random organization in periodically driven systems". In: *Nat. Phys.* 4 (2008).

[39] Emmanuel Courtade et al. "Dark optical lattice of ring traps for cold atoms". In: *Phys. Rev. A* 74 (3 2006), p. 031403. DOI: `10.1103/PhysRevA.74.031403`. URL: `http://link.aps.org/doi/10.1103/PhysRevA.74.031403`.

[40] M Creutz. "End states, ladder compounds, and domain wall fermions". In: *Phys. Rev. Lett.* 83 (1999), pp. 2636–2639.

[41] K. B. Davis et al. "Bose-Einstein Condensation in a Gas of Sodium Atoms". In: *Phys Rev. Letters* 75.22 (1995).

[42] X Deng, C Jia, and C C Chien. In: *Phys. Rev. B* 91 (2015), p. 054515.

[43] S. DIEHL et al. "Quantum states and phases in driven open quantum systems with cold atoms". In: *Nat. Phys.* 4 (2008), p. 878.

[44] Sebastian Diehl et al. "Topology by dissipation in atomic quantum wires". In: *Nat. Phys.* 7.2106 (2011), p. 2106.

[45] Stephen Eckel et al. "Hysteresis in a quantized superfluid 'atomtronic' circuit". In: *Nat. Lett.* 506 (2014), p. 200.

[46] A Eckhardt et al. "Frustrated quantum antiferromagnetism with ultracold bosons in a triangular lattice". In: *EPL* 89 (2010), p. 100010.

[47] Manuel Endres et al. "Atom-by-atom assembly of defect-free one-dimensional cold atom arrays". In: *Science* 354.1024 (2016).

[48] A L Fetter and J D Walecka. *Quantum Theory of Many-Particle Systems*. New York: Dover Publications, 2003.

[49] Victor Galitski and Ian B. Spielman. "Spin–orbit coupling in quantum gases". In: *Nature* 494 (2013), p. 49.

[50] Alexander L. Gaunt et al. "Bose-Einstein Condensation of Atoms in a Uniform Potential". In: *Phys. Rev. Lett.* 110 (2013), p. 200406. URL: `http://link.aps.org/doi/10.1103/PhysRevLett.110.200406`.

[51] Jordan M. Gerton et al. "Direct observation of growth and collapse of a Bose-Einstein condensate with attractive interactions". In: *Nature* 408 (2000), pp. 692–695.

[52] N S Ginsberg, S R Garner, and L V Hau. "Coherent control of optical information with matter wave dynamics". In: *Nature* 445 (2007), p. 623.

[53] A.P. Godse and U.A. Bakshi. *Basic Electronics*. Tech. Pub. Pune, 2000.

[54] N Goldman et al. "Direct imaging of topological edge states in cold-atom systems". In: *PNAS* 110 (2013), p. 6736.

[55] N Goldman et al. "Light-induced gauge fields for ultracold atoms". In: *Rep. Prog. Phys.* 77 (2014), p. 126401.

[56] N. Goldman et al. "Light-induced gauge fields for ultracold atoms". In: *Rep. on Prog. Phys.* 77 (2014), p. 12.

[57] S. Greschner, L. Santos, and T. Vekua. "Ultracold bosons in zig-zag optical lattices". In: *Phys. Rev. A* 87 (3 2013), p. 033609. DOI: `10.1103/PhysRevA.87.033609`. URL: `http://link.aps.org/doi/10.1103/PhysRevA.87.033609`.

[58] Kenneth Gunter et al. "Bose-Fermi Mixtures in a Three-Dimensional Optical Lattice". In: *Phys Rev. Letters* 96 (2006), p. 180402.

[59] Huaiming Guo. "π Berry phase and topological excitation in interacting boson-fermion mixtures". In: *Phys. Rev. A* 92 (2015), p. 033625.

[60] Huaiming Guo and Shun-Qing Shen. "Topological phase in a one-dimensional interacting fermion system". In: *Phys. Rev. B* 84 (2011), p. 195107.

[61] Peter Hanggi, Peter Talkner, and Michal Borkovec. "Reaction-rate theory: fifty years after Kramer". In: *Rev. Mod. Phys.* 62 (1990), pp. 251–340.

[62] M. Z. Hasan and C.L. Kane. "Colloquium: Topological insulators". In: *Rev. Mod. Phys.* 82 (2010), p. 3045.

[63] Yasuhiro Hatsugai. "Quantized Berry Phases as a Local Order Parameter of a Quantum Liquid". In: *J. Phys. Soc. Jpn.* 45.12 (2006), p. 123601.

[64] Philipp Hauke et al. "Non-Abelian Gauge Fields and Topological Insulators in Shaken Optical Lattices". In: *Phys Rev. Letters* 109 (2012), p. 145301.

[65] Yan He and Chih-Chun Chien. "Boundary-induced dynamics in one-dimensional topological systems and memory effects of edge modes". In: *Phys. Rev. B* 94 (2016), p. 024308. DOI: 10.1103/PhysRevB.94.024308.

[66] O.J. Heilmann and E.H. Lieb. "Violation of the Non-Crossing Rule: The Hubbard Hamiltonain for Benzene". In: *Ann. N. Acad. Sci.* 172 (1971), p. 583.

[67] K Henderson et al. "Experimental demonstration of painting arbitrary and dynamic potentials for Bose–Einstein condensates". In: *New J. Phys.* 11 (2009), p. 043030.

[68] T. Hirano, H. Katsura, and Y. Hatsugai. "Topological classification of gapped spin chains: Quantized Berry phase as a local order parameter". In: *Phys. Rev. B* 77 (2008), p. 094431.

[69] Ming-Xia Huo et al. "A solenoidal synthetic field and the non-Abelian Aharonov-Bohm effects in neutral atoms". In: *Sci. Rep.* 4 (2014), p. 5992.

[70] Bryce Fore Ian Gilbert Gia-Wei Chern et al. "Direct visualization of memory effects in artificial spin ice". In: *Phys. Rev. B* 92 (2015), p. 104417.

[71] Richard James. "Magnetic Alloys Break the Rules". In: *Nature* 521 (2015), p. 298.

[72] Yi-Hao Jhu, Pochung Chen, and Ming-Chiang Chung. "Observation of the topological soliton state in the Su-Schrieffer-Heeger model". In: *arXiv:1610.00851* (2016). URL: http://arxiv.org/abs/1610.00851.

[73] C. J. Jia et al. "Fidelity study of the superconducting phase diagram in the two-dimensional single-band Hubbard model". In: *Phys. Rev. B* 84.12 (2011), p. 125113. ISSN: 10980121. DOI: 10.1103/PhysRevB.84.125113.

[74] D.C. Jiles and D. L. Atherton. "Ferromagnetic Hysteresis". In: *IEEE Transactions on Magnetics* 19 (1983), p. 5.

[75] K. Jiménez-García et al. "Peierls Substitution in an Engineered Lattice Potential". In: *Phys. Rev. Lett.* 108 (2012), p. 225303.

[76] Gyu-Boong Jo et al. "Ultracold Atoms in a Tunable Optical Kagome Lattice". In: *Phys. Rev. Lett.* 108 (4 2012), p. 045305. DOI: 10.1103/PhysRevLett.108.045305. URL: http://link.aps.org/doi/10.1103/PhysRevLett.108.045305.

[77] Gregor Jotzu et al. "Experimental realization of the topological Haldane model with ultracold fermions". In: *Nature* 515 (2014), pp. 237–240.

[78] J. Jünemann et al. "Exploring Interacting Topological Insulators with Ultracold Atoms: The Synthetic Creutz-Hubbard Model". In: *Phys. Rev. X* 7.031057 (2017), p. 031057.

[79] Sachindra Nath Karmakar and Santanu Kumar Maiti andJayeeta Chowdhury. *Physics of Zeroand One-Dimensional Nanoscopic Systems*. Vol. 156. solid-state sciences. Springer, 2007.

[80] A. M. Kaufman et al. "Two-particle quantum interference in tunnel-coupled optical tweezers". In: *Science* 345 (2014), p. 306.

[81] John L. Kelley. *General Topology*. University Series in Higher Mathematics. Van Nostrand, 1955.

[82] S Kouachi. In: *Electron. J. Linear. Al. (ELA)* 15 (2006).

[83] A. Kumar et al. "Minimally destructive, Doppler measurement of a quantized flow in a ring-shaped Bose–Einstein condensate". In: *New J. Phys.* 18 (2016), p. 025001.

[84] C. Laflamme, D. Yang, and P. Zoller. "Continuous measurement of an atomic current". In: *Phys. Rev. A* 95 (2017), p. 043843.

[85] Renate Landig et al. "Quantum phases from competing short- and long-range interactions in an optical lattice". In: *Nature* 532 (206), p. 476.

[86] Martin Lebrat et al. "Assembling a mesoscopic lattice in a quantum wire for ultracold fermions". In: *ArXive* (pre-print) (2017), p. 1708.01250v2.

[87] Jeffrey G. Lee and W. T. Hill III. "Spatial shaping for generating arbitrary optical dipole traps for ultracold degenerate gases". In: *Rev. Sci. Instrum.* 85 (2014), p. 103106.

[88] Brian J. Lester et al. "Rapid Production of Uniformly Filled Arrays of Neutral Atoms". In: *Phys Rev. Letters* 115 (2015), p. 073003.

[89] L. P. Levy et al. "Magnetization of Mesoscopic Copper Rings: Evidence for Persistent Currents". In: *Phys. Rev. Lett.* 64.17 (1990), p. 2074.

[90] Maceij Lewenstein, Anna Sanpera, and Veronica Ahufinger. *Ultracold Atoms in Optical Lattices: Simulating Quantum Many-Body Systems*. Oxford University Press, 2012.

[91] Yean-An Liao et al. "Spin-imbalance in a one-dimensional Fermi gas". In: *Nature* 467 (2010), p. 09393.

[92]   Elliott H Lieb and F Y Wu. "The one-dimensional Hubbard model : a reminiscence". In: *Physica A* 321 (2003), pp. 1–27. DOI: 10.1016/S0378-4371(02)01785-5.

[93]   H.Q. Lin et al. "Exact Diagonalization Methods for Quantum Systems". In: *Comput. Phys.* 7.4 (1993), p. 400. ISSN: 08941866. DOI: 10.1063/1.4823192. URL: http://scitation.aip.org/content/aip/journal/cip/7/4/10.1063/1.4823192.

[94]   Y.-J. Lin, K. Jiménez-Garcá, and I. B. Spielman. "Spin–orbit-coupled Bose–Einstein condensates". In: *Nat. Lett.* 471 (2011), p. 09887.

[95]   Y.-J. Lin et al. "Synthetic magnetic fields for ultracold neutral atoms". In: *Nature Lett.* 462.628 (2009).

[96]   M. Lohse et al. "A Thouless quantum pump with ultracold bosonic atoms in an optical superlattice". In: *Nat. Phys.* 12 (2016), p. 3584.

[97]   G D Mahan. *Condensed matter in a nutshell*. Princeton University Press, 2011.

[98]   Salvatore R. Manmana, Alejandro Muramatsu, and Reinhard M. Noack. "Time evolution of one-dimensional quantum many body systems". In: *AIP Conf. Proc.* 789 (2005), pp. 269–278. ISSN: 0094243X. DOI: 10.1063/1.2080353.

[99]   Salvatore R Manmana et al. "Topological invariants and interacting one-dimensional fermionic systems". In: *Phys. Rev. B* 86 (2012), p. 205119. DOI: 10.1103/PhysRevB.86.205119.

[100] Eric J. Meier, Fangzhao Alex An, and Bryce Gadway. "Observation of the topological soliton state in the Su-Schrieffer-Heeger model". In: *arXiv* 1609.09467 (2016). URL: http://arxiv.org/abs/1607.02811.

[101] F. E. Meijer, A. F. Morpurgo, and T. M. Klapwijk. "One-dimensional ring in the presence of Rashba spin-orbit interaction: Derivation of the correct Hamiltonian". In: *Phys. Rev. B* 66 (2002), p. 033107.

[102] Bert Mendelson. *Introduction To Topology*. Allyn and Bacon, Inc., 1975.

[103] N D Mermin and H Wagner. In: *Phys. Rev. Lett.* 17 (1966), p. 1133.

[104] M. Metcalf, C.Y. Lai, and C.C. Chien. "Hysteresis of noninteracting and spin-orbit-couples atomic Fermi gases with relaxation". In: *Phys. Rev. A* 93 (2016), p. 053617.

[105] M. Metcalf et al. "Protocols for dynamically probing topological edge states and dimerization with fermionic atoms in optical potentials". In: *EPL* 118 (2017), p. 56004.

[106] Mekena Metcalf et al. "Matter-wave propagation in optical lattices: geometrical and flat-band effects". In: *J. Phys. B* 49 (2016), p. 075301.

[107] Hirokazu Miyake et al. "Realizing the Harper Hamiltonian with Laser-Assisted Tunneling in Optical Lattices". In: *Phys. Rev. Lett.* 111 (2013), p. 185302.

[108] Olivier Morizot et al. "Ring trap for ultracold atoms". In: *Phys. Rev. A* 74 (2 2006), p. 023617. DOI: `10.1103/PhysRevA.74.023617`. URL: `http://link.aps.org/doi/10.1103/PhysRevA.74.023617`.

[109] R. Mottl et al. "Roton-type mode softening in a quantum gas with cavity-mediated long-range interactions". In: *Science* 336 (2012), p. 1570.

[110] Erich J. Mueller. "Superfluidity and mean-field energy loops: Hysteretic behavior in Bose-Einstein condensates". In: *Phys. Rev. A* 66 (2002), p. 063603.

[111] Shuta Nakajima et al. "Topological Thouless pumping of ultracold fermions". In: *Nat. Phys.* 12.April (2016), p. 3622. DOI: `10.1038/NPHYS3622`.

[112] S. Ospelkaus et al. "Localization of Bosonic Atoms by Fermionic Impurities in a Three-Dimensional Optical Lattice". In: *Phys Rev. Letters* 96.180403 (2006).

[113] H. Ott et al. "Collisionally Induced Transport in Periodic Potentials". In: *Phys Rev. Letters* 92 (2004), p. 160601.

[114] R. Peierls. "On the theory of diamagnetism of conduction electrons". In: *Z. Phys.* 80 (1933), pp. 763–791.

[115] R A Pepino et al. "Atomtronic Circuits of Diodes and Transistors". In: *Phys. Rev. Lett.* 103 (2009), p. 140405.

[116] Alexey V. Ponomarev et al. "Atomic Current across an Optical Lattice". In: *Phys Rev. Letters* 96 (2006), p. 050404.

[117] P. Prelovsek and J. Bonca. "Strongly Correlated Systems Numerical Methods". In: Springer, 2013. Chap. Ground State and Finite Temperature Lanczos Methods.

[118] W Press et al. *Numerical Recipes: The art of scientific computing*. Cambrige University Press, 2007.

[119] Xiao-Liang Qi and Shou-Cheng Zhang. "Topological insulators and superconductors". In: *Rev. Mod. Phys.* 83 (2011), p. 1057.

[120] A. Ramanathan et al. "Superflow in a Toroidal Bose-Einstein Condensate: An Atom Circuit with a TunableWeak Link". In: *Phys. Rev. Lett.* 106.130401 (2011), p. 130401.

[121] C. Regal. "Bringing order to neutral atom arrays". In: *Science* 354 (2016), p. 973.

[122] T. W. Roberti, B. A. Smith, and J. Z. Zhang. "Ultrafast electron dynamics at the liquid–metal interface: Femtosecond studies using surface plasmons in aqueous silver colloid". In: *J. Chem. Phys.* 102.3860 (1995), p. 3860.

[123] J. P. Ronzheimer et al. "Expansion Dynamics of Interacting Bosons in Homogeneous Lattices in One and Two Dimensions". In: *Phys. Rev. Lett.* 110 (2013), p. 205301.

[124] J. A. Rushton, M. Aldous, and M. D. Himsworth. "The feasibility of a fully miniaturized magneto-optical trap for portable ultracold quantum technology". In: *Rev. of Scientific Instruments* 85 (2014), p. 121501.

[125] Inouye S. et al. "Observation of Feshbach resonances in a Bose–Einstein condensate". In: *Nature* 392 (1998), p. 151.

[126] R. W. Schoenlein et al. "Femtosecond Studies of Nonequilibrium Electronic Processes in Metals". In: *Phys Rev. Letters* 58.16 (1987), pp. 1680–1683.

[127] U. Schollwök. "The density-matrix renormalization group". In: *Rev. Mod. Phys.* 77 (2005), p. 1.

[128] D V Schroeder. *An introduction to thermal physics*. New York, USA: Addison Wesley Longman, 2000.

[129] B T Seaman et al. In: *Phys. Rev. A* 75 (2007), p. 023615.

[130] Medha Sharma and M. A H Ahsan. "Organization of the Hilbert space for exact diagonalization of Hubbard model". In: *Comput. Phys. Commun.* 193 (2015), pp. 19–29. ISSN: 00104655. DOI: `10.1016/j.cpc.2015.03.014`. arXiv: `arXiv:1307.7542v1`. URL: `http://dx.doi.org/10.1016/j.cpc.2015.03.014`.

[131] Shun-Qing Shen. *Topological Insulators: Dirac Equation in Condensed Matters*. Vol. 174. Springer, 2012.

[132] Y. Shin et al. "Observation of Phase Separation in a Strongly Interacting Imbalanced Fermi Gas". In: *Phys. Rev. Lett.* 97 (2006), p. 030401.

[133] R. P. Smith et al. "Effects of Interactions on the Critical Temperature of a Trapped Bose Gas". In: *Phys. Rev. Lett.* 106.250403 (2011), p. 250403.

[134] J. Struck et al. "Engineering Ising-XY spin-models in a triangular lattice using tunable artificial gauge fields". In: *Nat. Phys.* 9 (2013), p. 2750.

[135] E. Timmermans et al. "Feshbach resonances in atomic Bose–Einstein condensates". In: *Phys. Rep.* 315 (1999), p. 199.

[136] Murad Tovmasyan, Evert P. L. van Nieuwenburg, and Sebastian D. Huber. "Geometry-induced pair condensation". In: *Phys. Rev. B* 88 (22 2013), p. 220510. DOI: 10.1103/PhysRevB.88.220510. URL: http://link.aps.org/doi/10.1103/PhysRevB.88.220510.

[137] F. Nur Ünal, B. Hetenyi, and M. Ö. Oktel. "Impurity coupled to an artificial magnetic field in a Fermi gas in a ring trap". In: *Phys. Rev. A* 91 (2015), p. 053625.

[138] Kirill A. Velizhanin et al. "Intrinsic thermal conductance, extended reservoir simulations, and Kramers transition rate theory". In: *arXiv* (2013), p. 1312.5422.

[139] Massimiliano Di Ventra, Yuriy V. Pershin, and Leon O. Chua. "Circuit Elements With Memory: Memristors, Memcapacitors, and Meminductors". In: *IEEE* 97 (2009), p. 10.

[140] S. Viefersa et al. "Quantum rings for beginners: energy spectra and persistent currents". In: *Physica E* 21.1-35 (2004), pp. 1–35.

[141] Grigory E. Volovik. *The Universe in a Helium Droplet*. Oxford University Press, 2003.

[142] Da Wang et al. "Detecting edge degeneracy in interacting topological insulators through entanglement entropy". In: *Phys. Rev. B* 91 (2015), p. 115118. DOI: 10.1103/PhysRevB.91.115118.

[143] D. S. Weiss et al. "Another way to approach zero entropy for a finite system of atoms". In: *Phys. Rev. A* 70 (2004), 0403029(R).

[144] David S. Weiss and Mark Saffman. "Quantum Computing with Neutral Atoms". In: *Physics Today* 70.7 (2017), p. 44.

[145] Steven R. White. "Density-matrix algorithms for quantum renormalization groups". In: *Phys. Rev. B* 48.14 (1993), p. 14.

[146] Steven R. White. "Density Matrix Formulation for Quantum Renormalization Groups". In: *Phys. Rev. Lett.* 69 (1992), p. 19.

[147]   Naoki Yamamoto. "Generalized Bloch Theorem and Chiral Transport Phenomena". In: *arXiv* (2015), p. 1502.01547.

[148]   Wen Long You, Ying Wai Li, and Shi Jian Gu. "Fidelity, dynamic structure factor, and susceptibility in critical phenomena". In: *Phys. Rev. E* 76.2 (2007), p. 022101. ISSN: 15393755. DOI: 10.1103/PhysRevE.76.022101.

[149]   Naichang Yu and Michael Fowler. "Persistent current of a Hubbard ring threaded with a magnetic flux". In: *Phys. Rev. B* 45 (1992), p. 20.

[150]   T Zhang and G B Jo. *One-dimensional sawtooth and zigzag lattices for ultracold atoms*. arXiv:1510.02015. 2015.